On extending depth of field in fast photographic lenses

by

Niamh M. Fitzgerald

under the supervision of

Dr Alexander V. Goncharov

Submitted in Partial Fulfilment of the Requirements for the Degree of

Doctor of Philosophy (Ph.D.)

Applied Optics Group,

School of Physics,

National University of Ireland, Galway

April 2019

Contents

Declaration

The work in this thesis is based on research carried out at the Applied Optics Group, School of Physics, National University of Ireland, Galway. No part of this thesis has been submitted elsewhere for any other degree or qualification and it is all my own work unless otherwise referenced in the text.

Dearbhaím gurb é an taighde go hiomlán atá san ábhar seo atá mé a thíolacadh le haghaidh measúnachta déanta san Grúpa Optaice Feidhmí, Scoil na Fisice, Ollscoil na hÉireann, Gaillimh. Dearbhaím nár baineadh aon chuid de as saothar aon duine eile ach amháin sa mhéid atá luaite agus aitheanta sa téacs.

Niamh Fitzgerald
OÉ Gaillimh,
Aibreán 2019.

An Grúpa Optaice Feidhmí
applied optics
PHYSICS nuigalway

Abstract

Modern smartphone cameras are equipped with multiple camera modules. These modules are typically five millimetres in length limiting the focal length of the lens. To preserve resolution the entrance pupil of these lenses are relatively large compared to the focal length. Large apertures are subject to large amplitudes of optical aberrations. These perturbations can only be compensated within a short total track length by the use of high order polynomial surfaces. Fast lenses characteristically have a shallow depth of field whereby a small region in object space is adequately in-focus. This can be an undesirable effect for spatially-dependent imaging applications such as biometric sensing and user authentication. A large depth of field can reduce the need for mechanical refocusing and computationally intensive focusing algorithms. Traditionally in photographic optics, reducing pupil diameter directly results in an increased depth of field. However, due to resolution requirements the aperture cannot be stopped down. This thesis proposes novel approaches to extending depth of field for fast miniaturised camera lenses by employing optical design methods in whole or in major part. Utilising the lens parameters to increase the usable depth of field offers low-cost solutions that can possible replace voice coil motors and reduce the power consumption in camera modules.

This research was financially supported by Science Foundation Ireland and FotoNation under the Strategic Partnership Programme grant number $13/SPP/I2868$.

Acknowledgements

Firstly, I want to thank my supervisor Sasha - a great teacher, mentor and friend. Ever willing to share his experience and knowledge, he was always a reliable source of inspiration especially on the days when my own motivation lacked. My sincerest thanks to Prof. Chris Dainty for his encouragement towards unconventional optics, for ever enlightening discussions and invaluable advice.

Thank you to my officemates, Colm and Conor, who were always willing to have their brain picked. Also to Letty, Ken, Kim and Mark, thanks for all the constructive discussions and ridiculous tearoom conversations. Thanks to Dr Fiona Kenny, Dr Nicholas Devaney and the other members of the *Applied Optics Group* (past and present) who attributed to the wonderful working atmosphere. I would like to acknowledge Science Foundation Ireland and FotoNation for financially supporting this research. I want to extend my thanks to the staff and students of the C3I group; especially Shejin Thavalengal for sharing his knowledge on iris recognition. I also wish to thank Conor Boyce for his efficient collaborative work. I want to thank Prof. Herbert Gross for kindly hosting my visit to his group in Jena during the summer of 2016, and to his PhD students for their friendliness and hospitality.

I want to thank all the staff of the *School of Physics* in particular; Conor Mc Breirty, PJ Walsh and Rebecca Nolan for their kindness and endless good humour. A heartfelt thank you to Tess Mahoney for her years of 'saving the day'. An honourable mention to the physics gang; Aedán, Aonghus, Mike, Ali, Laura, James McG, Nina, Eoin, VJ and Kirsten - a marvellously outrageous group of people who were the best (and simultaneously worst) support group I could have asked for, I wouldn't be here without you all! Not forgetting some terrific friends who always had time for tea or wine; Alison, Sarah, Liam and Lisa-Marie.

To my family, who tried not to ask when my thesis will be finished - this is it! A special thanks to Aidan Uncle, Shirley and Rachel for always being here. Thanks to my sister Tríona, brother Gary, and new sister-in-law Aoife who always provided a few encouraging words and a good excuse to leave the computer. Finally, Mam and Dad, thank you from the bottom of my heart for your unconditional love

and support. It's from your example I learned the importance of hard work and perseverance that ultimately got me to this point. Here are the final words you've waited so long to hear ... I'm finished college now.

Go raibh míle mhaith agaibh,
Niamh

For Nana Fitzgerald

"I myself have always stood in awe of the camera. I recognize it for the instrument it is, part Stradivarius, part scalpel"

- Irving Penn

List of Figures

List of Tables

Abbreviations

AP aspheric plate

AS aperture stop

BFD back focal distance

BFL back focal length

CCD charged couple device

CL cylindrical lens

CMOS complementary metal-oxide-semiconductor

CP curved plate

DOE diffractive optical element

DOF depth of field

EDOF extended depth of field

EnP entrance pupil

ExP exit pupil

FOV field of view

GRIN gradient index

IPD interpupilary distance

IPSF identical point spread function

LC liquid crystal

LCA longitudinal chromatic aberration

LED light emitting diode

MR marginal ray

MTF modulation transfer function

NA numerical aperture

NIR near infrared

OPD optical path difference

OPL optical path length

OTF optical transfer function

PP parallel plate

PR principal ray

PSF point spread function

PTF phase transfer function

P-V peak to valley

RI refractive index

rms root mean squared

SLR single-lens reflex

TCA transverse chromatic aberration

TRA transverse ray aberration

TTL total track length

WFE wavefront error

WP wedge plate

VCM voice coil motor

ZP Zernike plate

Dissemination of PhD Research

All contributions carried out by the author in whole or in part over the duration of the PhD study are listed in the following sections.

Patents

- C. Dainty, A. Goncharov, N. Fitzgerald, "Iris Image Acquisition System", Application: 2017/0366761, (Published 21/12/2017).
- N. Fitzgerald, C. Dainty, A. Goncharov, "Iris Image Acquisition System", Application: 15/973359, (Submitted 17/05/2018).

Journal Articles

- N. M. Fitzgerald, J.C. Dainty and A.V. Goncharov,"Extending the depth of field with chromatic aberration for dual-wavelength iris imaging", Opt Exp, 25, 24, 2017.
- N. M. Fitzgerald, J.C. Dainty and A.V. Goncharov,"Widefield conferencing lens for a smartphone", Optical Communications (Submitted).

Conference Presentations and Proceedings

- N. Fitzgerald, A.V. Goncharov and J.C. Dainty,"Extending the Depth of Field in a Fixed Focus Lens Using Axial Colour", IODC , 31, 41, 2017.
- N. M. Fitzgerald, J.C. Dainty and A.V. Goncharov,"Two iris imaging over an extending depth of field with a mobile phone camera", SPIE Optical Systems Design, Frankfurt, 2018.
- N. M. Fitzgerald, J.C. Dainty and A.V. Goncharov, "Widefield lens in a smartphone", EOS Biennial Meeting, European Optical Society, Delft, 2018

Posters

- "Using LCA to Double the Depth of Field in Smartphone Cameras", N. Fitzgerald, A. V. Goncharov and J.C. Dainty, Photonics Ireland, (2017)
- "Optical element for imaging both irises over an extended the depth of field" N. Fitzgerald, J.C. Dainty and A. V. Goncharov, IOP Spring Meeting, (2018)

Chapter 1

Introduction

1.1 Mobile Imaging Camera Modules

Modern smart devices are equipped with multiple camera modules to enhance user security and imaging experiences. Compact camera modules are fast optical systems comprised of four to six plastic moulded lens elements that are shaped by high order aspheric surfaces. Lenses purposely designed for mobile device applications typically have F-numbers that range between of F/1.7 to F/2.7, having large apertures relative to the focal length of the lens module. Low F-numbers are desirable for photon collection to increase resolution and signal-to-noise ratio. Not all effects of fast lenses are positive, reduction in the depth of field and an increase of optical aberrations can be limiting consequences for these lenses. A limited depth of field can be somewhat compensated with modified phase elements, tunable mechanical refocusing elements and digital image processing techniques, which are discussed in Section 1.2. However, the growth in the number of active camera modules per device requiring digital assistance is increasingly computationally demanding. Therefore, new low-cost approaches are needed to lower power consumption and to offer realistic solutions for the modern consumer market.

Optical design for modern commercial imaging systems is not a trivial task. Fast imaging systems such as those found in mobile devices are fundamentally determined by the the thickness of the device. That is, the allowable module design space between the front and back housing of the device in which the total track length (TTL) for the lens is located, shown in Fig. 1.1. Most current mobile devices allow between four to five millimetres for the TTL, although modest increases in design space of one millimetre have been allocated in larger devices of late. A large entrance pupil diameter is required to ensure that sufficient light

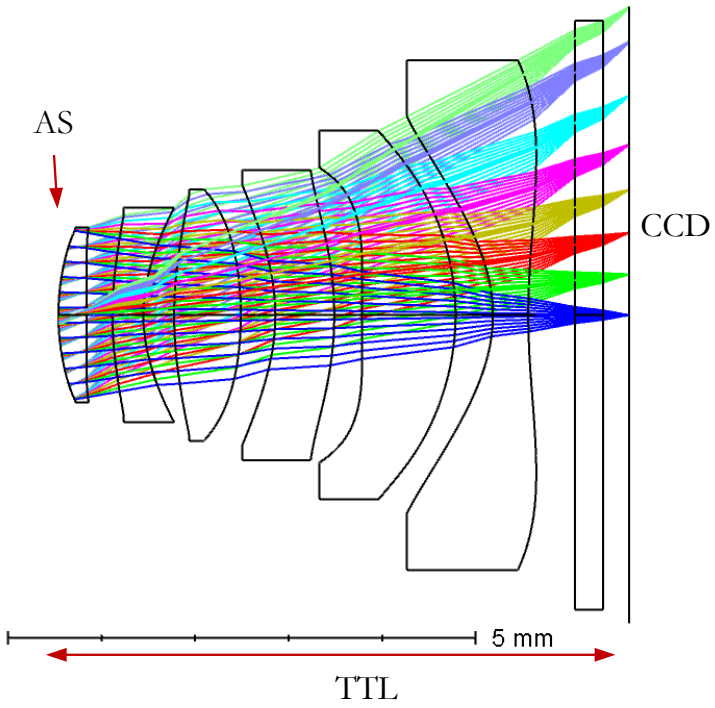

Figure 1.1: Traditional smartphone camera lens with labelled aperture stop (AS), total track length (TTL) and detector. Re-optimised in Zemax from design presented in [1].

is collected to maximise resolution and signal-to-noise ratio. The limit to which the diameter can be increased is related to the diffraction-limited image formed by the lens. The minimum acceptable entrance pupil is based on the angular resolution of the human eye. Therefore, the smallest acceptable pupil diameter is two millimetres. The sampling theorem governs the minimum usable Airy disk diameter from the detector pixel size. It can be deduced that the camera module has two critical parameters for which the optical designer must work from, the thickness of the device housing and detector pixel pitch. All remaining lens parameters are designed in such a way to maximise the performance of the system.

One parameter that is determined by the spatial limitations of the lens module is the aperture stop, which is positioned at the front vertex of the lens. Stop position is a result of space restriction within the lens. The horizontal field of view (FOV) of these camera lenses is on average 70° which yields large principal ray angles with the detector. Detector manufacturers provide guidelines for the

maximum principal ray angle for their product. Current complementary metal-oxide-semiconductor (CMOS) detectors have a maximum acceptance principal ray angle with a value of approximately 35°. Ray angles that do not match the guidelines are subject to cross-talk producing undesirable effects in the image.

The range of refractive indices for imaging optical polymers is ever increasing. At the beginning of this project, the range of available optical plastics was limited which restricted effective balancing of chromatic aberration in plastic-only lenses. Colour correction often required a combination of glass and plastic elements. In many cases, when chromatic aberration would be reduced sufficiently residual effects were cleaned up by computational means. This is more successful with lateral colour than axial colour. The advancement in the polymer industry can now offer higher refractive indices through means of doping optical polymers.

In this chapter a brief introduction to the fundamental concepts in photographic optics is presented. A clear understanding of the background frames the challenges and limitations associated with commercial camera modules and the performance trade-offs required to increase the depth of field by optical means.

Fundamental Concepts of Photographic Optics

Diffraction is the fundamental limit of image forming optical systems. Circular apertures are the most common aperture shape found in photographic optics. The Fraunhofer diffraction pattern of a circular aperture with radius a is known as the Airy pattern, which has a characteristic central intensity peak surrounded by concentric rings of decreasing intensity with increasing radius. The intensity distribution at the Gaussian focus plane of a diffraction-limited lens with a uniformly illuminated circular aperture is described by:

$$I(r) = \left[\frac{2J_1(v)}{v}\right]^2, \tag{1.1}$$

where $v = (2\pi ar)/(\lambda l')$ is a dimensionless optical parameter, $r = \sqrt{x^2 + y^2}$ is the image plane coordinate, l' is the distance to the focus plane, λ is the illumination wavelength and J_1 is a Bessel function of the first order which mathematically describes the spacing of the rings in the Airy pattern. The first zero point of the

diffraction pattern occurs at $v = 3.833$. The radius of the first minimum can be found by $l' \approx f'$ for an infinitely conjugated object:

$$r_{Airy} = 1.22\lambda\frac{f'}{D}, \tag{1.2}$$

where f' is the focal length of the lens, D is the EnP diameter and λ is the mean wavelength, usually taken as $0.55\mu m$. Rayleigh defined a criterion for resolution which states that two closely located image points of equal intensity can be resolved if the central maximum of one Airy disk falls on the first zero of the other [6]. This criterion is a limiting factor that determines the resolution of image forming optical systems. For two incoherent object points the minimum separation distance for resolving the images individually is described by Eq. (1.2). It is clear that the Airy disk size depends upon the lens parameters, focal length and entrance pupil (EnP) diameter. It is assumed that the edge of the EnP coincides with the lens aperture. The ratio of the focal length to the diameter seen in Eq.(1.2) is called the lens F-number and is commonly used in photography to described the light collecting ability of the lens. For an object located at infinity, the F-number of a lens is written as:

$$F\# = \frac{f'}{D}, \tag{1.3}$$

where f' is the focal length of the lens and D is the diameter of the entrance pupil [7]. Equation (1.3) indicates that for a constant focal length, an increase in entrance pupil diameter forms an Airy disk with a reduced diameter on the image plane. For finite conjugate imaging systems, the definition for the traditional F-number in Eq. (1.3) no longer holds. The focal plane cannot be considered as the image plane for an object that is positioned at a finite distance l in front of the lens, therefore the back focal distance (BFD) denoted by l' is substituted in for the new image position. This relationship is known as the *working F-number* given by:

$$F_W\# = \frac{l'}{D}. \tag{1.4}$$

A lens is considered faster with decreasing F-number. Equations (1.3) and (1.4) denote that for a small F-number the distance of the image plane from the lens approaches the diameter of the EnP. Adhering to mobile device housing restrictions, the lenses found in mobile devices have a small F-number with values between

$F\# = 1.7$ to $F\# = 2.7$, having a short focal length and large diameter. In contrast, an astronomical telescope has a much longer focal length which is imperative for aberration control and mounting restrictions. Astronomical imaging instruments are known be slow systems with an F-number of usually at least $F\# = 10$.

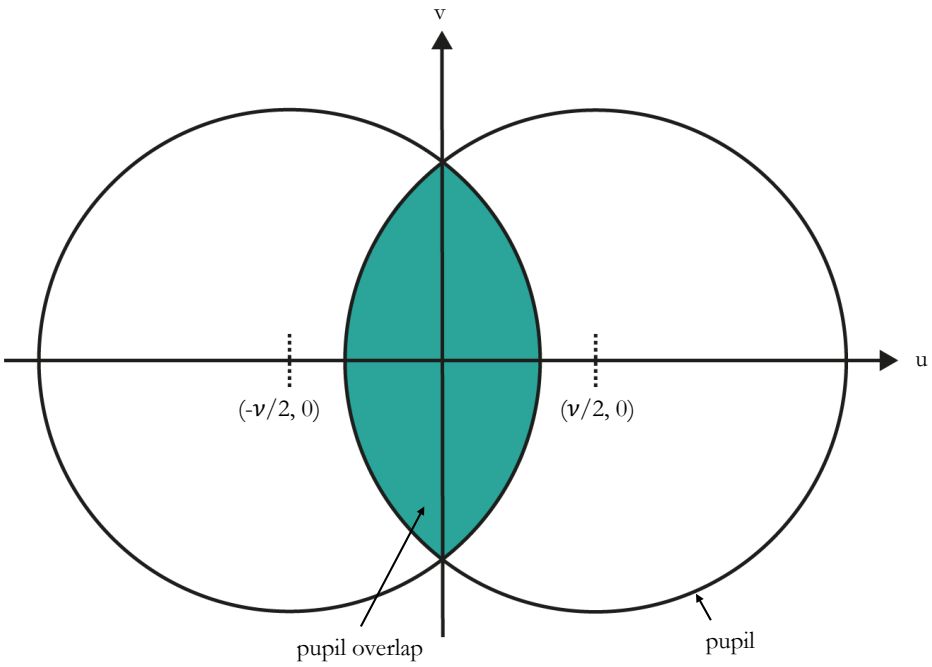

Figure 1.2: Geometrical interpretation of autocorrelating the pupil function.

The performance of a photographic lens is quantified by measuring the spatial frequencies transmitted by the lens. Input and output irradiance functions, $F(\nu_x, \nu_y)$ and $G(\nu_x, \nu_y)$ respectively, of an optical system are related by the system response function $T(\nu_x, \nu_y)$ known as the optical transfer function (OTF):

$$G(\nu_x, \nu_y) = F(\nu_x, \nu_y) \cdot T(\nu_x, \nu_y). \tag{1.5}$$

The OTF is the normalised Fourier transform of the system impulse response function, which is known as the intensity point spread function (PSF) $h(x, y)$ in optics. The OTF is defined as:

$$T(\nu_x, \nu_y) = \int_{-\infty}^{\infty} \int_{-\infty}^{\infty} h(x, y) e^{-2\pi i(x\nu_x + y\nu_y)} dxdy, \tag{1.6}$$

where (ν_x, ν_y) are spatial frequencies, which have the relation $\nu_x = \frac{u}{\lambda f'}$ and $\nu_y = \frac{v}{\lambda f'}$ with u and v being pupil coordinates. A measure of the OTF is obtained by auto-correlating the pupil function of the optical system [8]. This can either be carried out by Fourier transform methods or by direct calculation from a Duffieux integral. A pupil with coordinates (u, v) can be described by the pupil function [9]:

$$\mathcal{P}(u, v) = P(u, v) \exp(-ikW(u, v)), \tag{1.7}$$

where $P(u, v)$ is the amplitude variation over the pupil, $k = 2\pi/\lambda$, $W(u, v)$ is the wavefront variation [10]. The amplitude is assumed to be unity within the pupil of diameter D and zero outside:

$$P(u, v) = \begin{cases} 1, & P \subset D \\ 0, & P \not\subset D. \end{cases} \tag{1.8}$$

The OTF is then an integration over the common area of two sheared pupils described by:

$$T(\nu) = \frac{1}{A} \int\int \mathcal{P}\left(u + \frac{\nu}{2}, v\right) \mathcal{P}^*\left(u - \frac{\nu}{2}, v\right) dudv \tag{1.9}$$

where A is the total pupil area and spatial frequency is denoted as ν. Equation (1.9) can be expanded into the Duffieux integral which can be used for direct calculation of the OTF:

$$T(\nu_x, \nu_y) = \frac{\int_{-\infty}^{\infty}\int_{-\infty}^{\infty} \mathcal{P}\left(u + \frac{\lambda f \nu_x}{2}, v + \frac{\lambda f \nu_y}{2}\right) \mathcal{P}^*\left(u - \frac{\lambda f \nu_x}{2}, v - \frac{\lambda f \nu_y}{2}\right) dudv}{\int_{-\infty}^{\infty}\int_{-\infty}^{\infty} |\mathcal{P}(u, v)|^2 dudv} \tag{1.10}$$

For diffraction limited systems, the aberration function is zero, and $T(u, v)$ is plotted as a continuous blue line in Fig. 1.3. For real optical systems, where the aberration function has a non-zero value, a decrease in contrast is found, which is represented with defocus by the coloured lines in Fig. 1.3. An optical system is tolerable to a finite amplitude of residual aberrations without experiencing detrimental effects. This is discussed in the next section.

The OTF is a complex function composed of two parts, the MTF and phase transfer function (PTF) which are related to the OTF by:

$$T(\nu_x, \nu_y) = M(\nu_x, \nu_y) e^{iP(\nu_x, \nu_y)}. \tag{1.11}$$

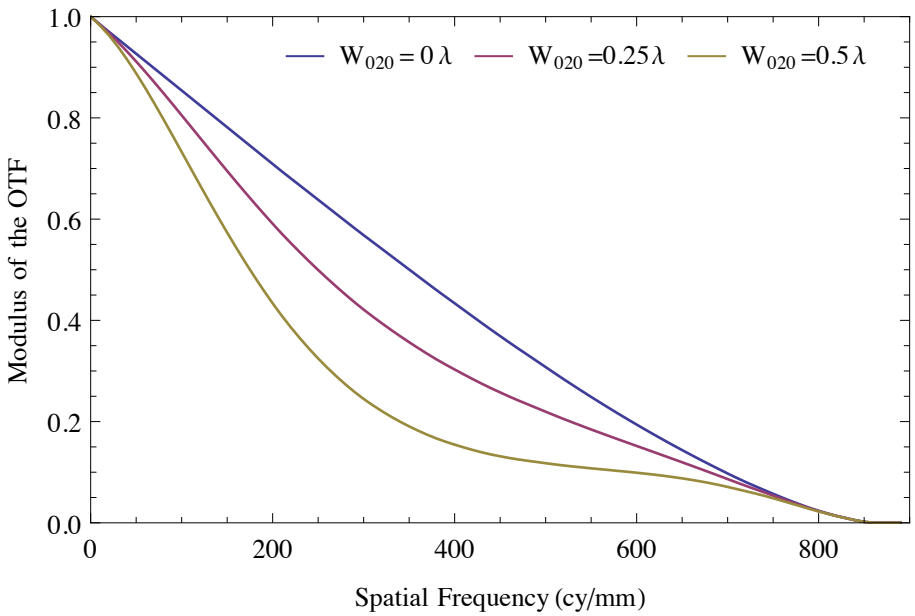

Figure 1.3: MTF for an F/2 paraxial lens with a non-obscured aperture in the presence of defocus at $W_{020} = 0\lambda$ (blue), $W_{020} = 0.25\lambda$ (pink) and $W_{020} = 0.5\lambda$ (yellow).

The MTF is the modulus of the OTF:

$$MTF(\nu) = |T(\nu)|, \tag{1.12}$$

and is always normalised to be unity at zero spatial frequency. This normalisation retains the contrast while eliminating the information about the absolute intensity values. The MTF is the only component of the OTF that is discussed in this thesis as it is a standard measure of the spatial frequency response of photographic lenses. The frequency ν in Eq.(1.9) is normalised to have a value of $\nu = 2$ for the maximum resolvable spatial frequency. For a diffraction limited lens the MTF falls to zero at a critical cut-off frequency $\nu_c = 1/(\lambda F\#)$, with units of lp/mm or cy/mm. MTF fall-off is affected by the presence of optical aberrations. Figure 1.3 shows how the MTF curve is modified in the presence of defocus (W_{020}).

The sensor is typically the most expensive component of a commercial camera module. Therefore, the lens is designed to the specifications of the sensor. According to the sampling theorem, the maximum frequency that can be faithfully

reconstructed is:

$$\nu_N = \frac{1}{2\delta x}, \tag{1.13}$$

where δx is the pixel pitch of the detector [9]. All frequencies below Nyquist (ν_N) can be reconstructed while all frequencies above are aliased. Rearranging Eq. (1.13) and substituting for ν_c, the minimum pixel pitch is:

$$\delta x = \frac{f'\lambda}{2D}. \tag{1.14}$$

In order to sample the PSF correctly, the resolution of the lens is considered from Eq. (1.2). For a given Airy radius r, the minimum number of pixels to satisfy the Nyquist sampling is $r \geq 2$ pixels. Pixel size for these camera modules are commonly $1.1\mu m$, which is determined by the semiconductor industry. Though advancements towards decreasing pixel size is ongoing with the current limit set at 0.8 μm in sensors such as the Sony IMX586 CMOS.

Depth of Focus and Depth of Field

In a paraxial or perfect imaging system a point object forms a perfect point image where the coordinate systems are proportional to one another. However, this relationship does not extend to systems compromised by optical aberrations. Wavefront deformations due to optical aberrations can generate image shifts and cause changes to image spot geometry. Optical aberrations and their subsequent effects are discussed further in Chapter 2.

A perfectly spherical wavefront located in the exit pupil of the optical system focused by an ideal lens forms a rotationally symmetric diffraction-limited image spot at the Gaussian image plane. A defocus-perturbed wavefront that departs from the reference sphere in the exit pupil generates a change in the optical path difference (OPD), which in turn causes a longitudinal shift of the image from the ideal image plane by a distance $\Delta l'$. For small amplitudes of defocus, the longitudinal displacement of the image focus can be examined through considering a change in the OPD between the reference sphere W_R and a spherical wavefront W_{020}. The reference sphere has a radius of curvature R, and the spherical wavefront in the presence of defocus has a radius of curvature of R_{020} at a distance $\Delta l'$ from R. The OPD between the two wavefronts at a height h is OPD = $[W_{020}W_R]$.

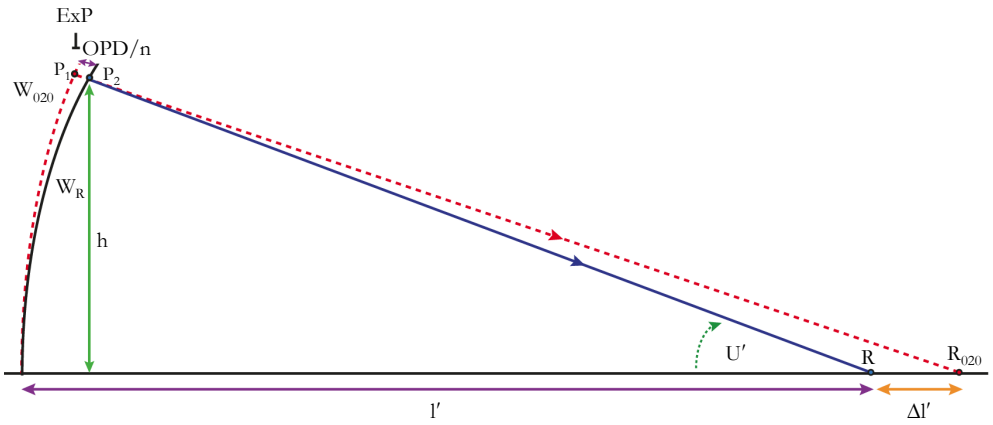

Figure 1.4: Longitudinal focus shift by $\Delta l'$ caused by the departure of W_{020} from the Gaussian reference sphere W_R.

As the optical path is the geometrical path multiplied by the refractive index (RI) n, the optical path length between P_1 and P_2 is:

$$OPD = nP_1P_2. \tag{1.15}$$

The OPD can be described as the difference in sag between the two spherical wavefronts written as $\delta_{sag} = z_{020} - z_R$, which is measured along the ray. The sag of a sphere is described as $h^2/2R$ where h is the marginal ray height. The difference in wavefront sag is expanded from Eq.(1.15):

$$OPD = \frac{nh^2}{2R_{020}} - \frac{nh^2}{2R}. \tag{1.16}$$

Collecting the common variables, and substituting in $R_{020} = R - \Delta l'$, the OPD is:

$$OPD = \frac{nh^2}{2}\left(\frac{1}{R - \Delta l'} - \frac{1}{R}\right). \tag{1.17}$$

Rearranging Eq.(1.17) yields the expression:

$$OPD = \frac{nh^2}{2}\frac{\Delta l'}{2R(R - \Delta l')}. \tag{1.18}$$

For $\Delta l' \ll R$ and $h^2/R^2 = \sin^2 U'$, then the OPD between wavefronts can be expressed as:

$$OPD = -\frac{1}{2}n \sin^2 U' \Delta l', \tag{1.19}$$

illustrated in Fig. 1.4. The calculation is made for a mean wavelength λ within a given refractive index n for λ, and U' is the angle of the marginal ray incident on the image plane. The marginal ray is used for calculations as the maximum amount of aberration is induced at the edge of the pupil.

The Rayleigh criterion describes an optical system as being diffraction limited provided that the peak to valley (P-V) wavefront error (WFE) is smaller than $\lambda/4$ and is referred to as the Rayleigh quarter wavelength rule, $|W_{P-V}| = \lambda/4$. This rule was originally derived to show that an increase in spherical aberration in the P-V WFE in the exit pupil reduces the irradiance of the central peak of the Airy disk by twenty percent, it can also serve as rough guideline for other aberrations, such as defocus.

Equation (1.19) can be equated to a quarter wavelength to derive the maximum tolerable axial displacement of the image with respect to the ideal image position:

$$\frac{\lambda_0}{4n} = -\frac{1}{2} n \sin^2 U' \Delta l'. \tag{1.20}$$

Rearranging Eq.(1.20) and solving for $\Delta l'$, the axial displacement of the image point is:

$$\Delta l' = -\frac{2\lambda_0}{4n^2 \sin^2 U'}. \tag{1.21}$$

The numerical aperture (NA) of an optical system is $NA = n \sin U'$ and the F-number is therefore related by $F\# = n/(2NA)$. The refractive index is taken as $n = 1$ for an image formed in air. Substituting in to Eq.(1.21), a simple expression for depth of focus can be found:

$$\Delta l' = \pm \frac{2\lambda_0}{(2NA)^2} = 2\lambda_0 F\#^2. \tag{1.22}$$

A simple substitution of variables $\Delta z = \Delta l'$ gives the conventional representation for depth of focus and is defined to be maximum axial shift of the detector from the ideal image plane. That is, the maximum acceptable blur in the image without noticeably degrading the sharpness of the image. The depth of focus can also be geometrically estimated by the maximum acceptable blur diameter of the image spot on the detector:

$$\Delta z = c' F\#, \tag{1.23}$$

where c' is the image sided circle of least confusion. The pixel size of the detector will then determine the circle of least confusion. In a typical smartphone the value of c' is approximately one to two pixels in diameter.

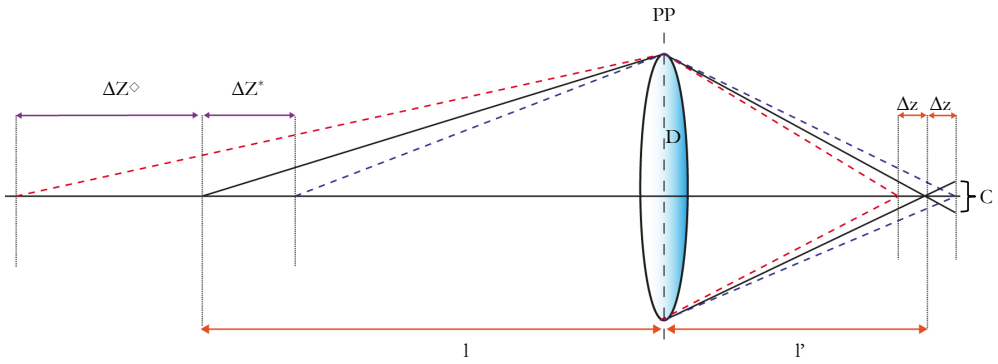

Figure 1.5: Depth of field and depth of focus for a simple thin lens.

In many spatially dependent applications whereby the maximum axial region from the object is required to be known, the DOF becomes an important parameter. Just as the maximum allowable distance in image space is the depth of focus, DOF is used when describing the allowable blur in object space [11]. The depth of field can be defined as:

$$\Delta Z = \frac{\Delta z}{\bar{m}} = \frac{1}{\bar{m}}\left(\frac{\Delta f'}{\Delta D}\right), \tag{1.24}$$

where $\bar{m}$ is the axial magnification, $\Delta f'$ is the variation in focal length and ΔD is the variation in entrance pupil diameter. Here it is clear to see the dependency of DOF on F-number, the importance of aperture diameter to be more exact. For a constant focal length, DOF is inversely proportional to the entrance pupil diameter. For large photographic lenses, such as those found in DSLR cameras, depth of field can be extended or reduced by varying a mechanical iris within the lens. The longitudinal magnification from image space to object space typically has a value of $\bar{m} \ll 1$ in miniature cameras. For a small depth of field, the longitudinal magnification can be approximated by the square of the lateral magnification $\bar{m} = m^2$, where:

$$m = \frac{l'}{l} = \frac{f'}{l}, \tag{1.25}$$

and l is the object position. Combining Eq. (1.24) and Eq. (1.25), under the condition $l' = f'$, the total depth of field is expressed as:

$$\Delta Z = \pm 2\lambda \frac{l^2}{D^2}. \tag{1.26}$$

Equation (1.26) assumes that the depth of field is symmetric about the object point similar to the depth of focus. However, this is not an accurate representation of the ratio between near and far regions of focus about the point in the DOF.

The points in image space which mark the limits for the depth of focus are conjugate to two object points which are the limiting points to the depth of field. The symmetric expression for depth of focus given in Eq. (1.22) yields an asymmetric expression for depth of field due to the difference in longitudinal magnification. The near and far regions of the DOF are defined with respect to the front vertex of the lens, as shown in Fig. 1.5.

When known, the circle of least confusion can also be use to calculate depth of field [12; 13]. The hyperfocal distance H is the distance at which the lens must be focused so that the depth of field extends to infinity. In the case of $H \gg f'$ and $H = l$, the image is acceptably sharp from H/2 to infinity [11; 12]. The diffraction dependent hyperfocal distance is given by:

$$H = \frac{f'^2}{2\lambda F\#^2} = \frac{f'^2}{\Delta z}, \tag{1.27}$$

where f' is the focal length and $F\#$ is the lens F-number. Eq. (1.23) can be substituted in to Eq. (1.27) in order to gain an approximation for the geometrical hyperfocal distance as dependent on the acceptable blur diameter. For $l \gg f'$, the near and far regions can then be written separately:

$$Z^* = \frac{Hl}{H + l - f'} \tag{1.28}$$

and

$$Z^\diamond = \frac{Hl}{H - l + f'}, \tag{1.29}$$

where Z^* denotes the near DOF region and $Z^\diamond$ is the far region. The sum of $(Z^* + Z^\diamond)/2$ is equal to the total DOF value of ΔZ found from Eq. (1.26). It is important to note that for objects positioned in close proximity to the lens the difference in near and far regions of the depth of field is negligible as their ratio

approaches unity. The asymmetry in near and far regions of the depth of field increases as the object approaches the hyperfocal distance.

For finite conjugate thin lenses an exact derivation for the asymmetric regions of the DOF are derived in Chapter 3. This derivation is diffraction dependent and also independent of the hyperfocal distance. Instead, the derivation uses the diffraction depth of focus.

1.2 Methods to Extend Depth of Field

In classical terms, the depth of field and depth of focus can be increased or decreased by varying the diameter of the EnP as interpreted from Eq.(1.22). In large photographic objective lenses, the DOF can be controlled by stopping down the physical aperture therefore changing the F-number of the lens. Annular apertures have proved beneficial for extending focal depth [14]. However, obstructing the aperture significantly reduces the light throughput. A physical change to the stop is not always feasible. A full aperture is needed for lenses with restricted design space or resolution threshold. Physical lens movements and specific phase elements aided by computational image reconstruction can provide alternative methods to achieve an extended DOF. The following sections are divided into EDOF methods including the use of phase masks, the physical movement of elements, and post-processing and computational image reconstruction, as shown in Fig. 1.6.

1.2.1 Phase masks

Phase masks are employed in EDOF systems to introduce a known amount of aberration whereby the scene is blurred evenly over a designated axial separation in object space. A priori knowledge of the optical system aberrations allows for an image of the scene to be reconstructed from intermediate images using the PSF or OTF.

A well established method that utilises a combination of physical elements and computational post-processing is a technique called wavefront coding. Wavefront coding is the name given to modifying the phase of an incoherent wave by a mask

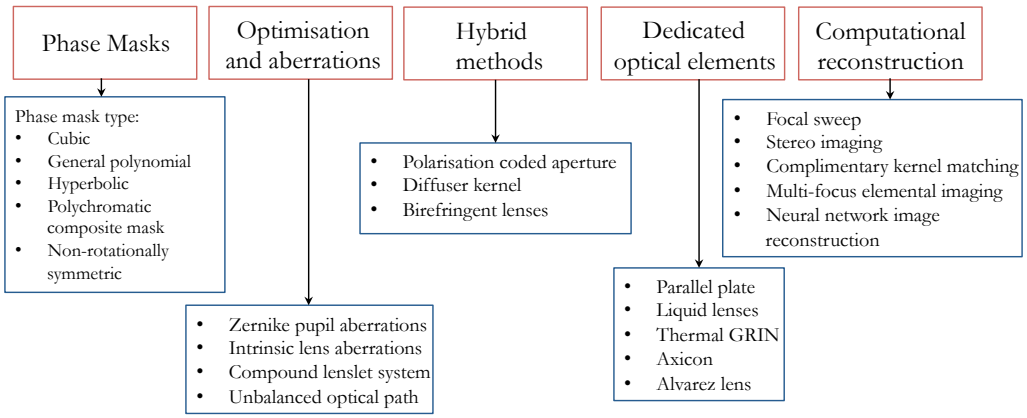

Figure 1.6: Methods to extend depth of field covered in this chapter.

within the pupil of the optical system. The modified system is understood to achieve near-diffraction limited performance over an extended depth of field. The concept of wavefront coding was introduced by Cathey and Dowski [15]. In their method, a phase mask is positioned in the pupil of the optical system producing modified intermediate images. Here, an intermediate image refers to an image requiring post-processing. The phase mask changes the phase through the optical system which in turn modifies the PSF and OTF such that both are insensitive to a change in focus. Post-processing by way of digital filtering is carried out on the intermediate images delivering a near diffraction-limited performance over an extended depth of field.

Extensions and variations to Cathey and Dowski's method have given rise to a wavefront coding research field. Such modifications have been developed to include polychromatic imaging. A binary phase mask of annular rings that generate a π-phase shift for incoherent light was proposed initially for monochromatic light [16]. In this method the phase mask was designed for a designated central wavelength and optimised for a minimum contrast value. As a consequence of prioritising a single wavelength, other wavelengths underwent different phase shifts to the central. The out of focus criterion is described by the term ψ and defined by the lens parameters as the maximum phase error of the spherical wavefront at the boundary of a circular aperture of diameter D:

$$\psi = \frac{\pi R^2}{\lambda}\left(\frac{1}{z'} + \frac{1}{z} - \frac{1}{f'}\right), \tag{1.30}$$

where f' is the focal length of the lens, λ is the central wavelength, R is the pupil radius, z and z' are the object and image distances respectively. Wavelength variations influence both the phase and defocus parameter as shown in Eq. (1.30). Each wavelength produced different values for ψ. Chromatic effects noted by the authors resulted in terming the first iteration as a monochromatic phase mask (MPM). Addressing the variation in phase with wavelength, a modified phase mask consisting of annular rings was designed to introduce a π-phase shift for three selected wavelengths, called polychromatic composite masks (PCM) [17]. The PCM radii are optimised for a minimum cut-off frequency over the depth of field for three sampled wavelengths in the visible region. An improvement in MTF performance can be seen at 450 nm and 650 nm at the expense of the performance at 550 nm. Two PCM elements of inverse profiles, one generating a negative phase shift with positive dispersion and one positive phase shift with low dispersion, placed together in the pupil can achieve almost constant phase shift for the entire illumination bandwidth.

Pre-determined wavelength dependent phase shifts can be induced by a custom designed RGB phase mask [18]. This approach is dependent on producing three different responses for each colour band of RGB, such that all colour channels are in focus for different regions in object space generating an extended depth of field. Combining RGB phase masks with post-processing algorithms similar to the work of Haim *et. al.* shows that the image scene can be restored using a blur modelled as a piecewise-constant kernel, which is defined by a defocus parameter determined from an object in the scene [19].

Milgrom *et al.* introduced an algorithm for designing imaging systems with circular symmetry to extend the depth of field and produce high resolution images using polychromatic incoherent illumination [20]. The authors address previous attempts to extend the depth of field for monochromatic light [21], and introduce a binary phase pupil mask that provides imaging at the highest cut-off spatial frequency while delivering an extended depth of field with the highest attainable contrast. The algorithm to select the best phase mask is designed to incorporate

a cut-off frequency at three discrete wavelengths.

A phase mask shaped by general polynomials can increase the depth of field. This particular type of phase mask is composed of a general polynomial with a high number of odd orders and converges to a stable solution [22]. The mask is optimised using an iteratively defined MTF target. The authors state that the resulting phase profile is similar to a cubic phase mask, but closely resembles an exponential mask. It has been shown to work for a microscope with central wavelength $\lambda = 470$ nm. Employing this approach for a slow optical system such as a microscope offers an extension in the achievable depth of field by a factor of ten.

Non-rotationally symmetric phase masks offer an extension in DOF up to five times across the field of view. Dong-mei Zho *et al.* employed a cubic phase plate to increase the depth of field of an integral imaging system, such as light field cameras [23]. It was proposed that a non-rotationally symmetric cubic phase plate placed in the pupil of each micro-lens in an array can enlarge the depth of field. This approach may increase depth of field but the imaging characteristics of the integral imaging system with the phase plate has not been analysed. With the increase of the defocus, a small variation in the MTF is shown over the extended depth of field and does not appear to have a zero point. The DOF of the microlens unit was shown to increase five times, ranging from 80 mm to 200 mm, when compared to a system of similar optical system parameters.

Tolerancing of optical elements is a central step in the design process and dictates the maximum errors tolerable by the system. Larivière-Bastien et. al. examined the tolerances of a cubic phase mask together with residual primary aberrations [24]. From this study, it was recommend that the residual aberrations of a hybrid system containing a cubic phase mask have a maximum of 1λ of primary spherical aberration, coma and astigmatism while maintaining field curvature below 1λ. The effect of system residual higher order aberrations has yet to be examined.

The use of multiple phase masks produce promising DOF extension. A pair of hyperbolic phase masks have been shown to decrease focus sensitivity and increase the area under the MTF [25]. A single hyperbolic mask acting as a spatial filter, together with a sub-Gaussian apodizer, can reduce the sensitivity

to defocus and reduce artefact noise while attaining a high area under the MTF curve. Ledesma showed that a pair of hyperbolic phase masks with thickness of $\lambda/2$ can be mechanically shifted using the Lohmann-Alvarez method, which can alter the depth of field while retaining a full aperture. The authors note that the light throughput is decreased by half using a pair of masks.

End-to-end design and experimental validation of an extended depth-of-field high definition camera with an f-number of $F/1.2$ over the visible spectrum was developed by Burcklen *et. al* for the visible and near infrared (NIR) bands [26]. The depth of field was increased by combining a six-ring pyramidal phase mask in the aperture of the lens with digital deconvolution. The phase mask and deconvolution algorithm were optimised together to achieve maximum performance over the EDOF range. Real-time deconvolution were carried out on an FPGA that requires a relatively low power consumption of 600mW compared to the 5W power consumption of the camera used in the experiment. A 2.5x extension in DOF was achieved.

Pupil aberrations have inspired custom non-rotationally symmetric phase elements. Positioning such elements in the pupil yields a direct modification of the wave aberration. Phase plates shaped with trefoil have shown to be advantageous in EDOF imaging systems for inducing spherical aberration and trefoil in monochromatic imaging. Chromatic aberration limits the benefit of such elements. Optimisation of trefoil phase plates can improve the performance of the element design for colour wavefront coding [27]. PMMA is chosen for the phase plate material which is responsible for inducing the optimal amount of spherical aberration and and chromatic aberration. In polychromatic imaging the effective depth of focus is limited by the shallow depth of focus for the shortest wavelength. It is necessary for the RGB depths of focus to overlap. Optimisation of a phase mask which extends the depth of focus is carried out by adding a fourth order polynomial to the plate shape. To simulate colour images, the intermediate blurred images are convolved with the PSF's for each channel at the corresponding image plane. The images are then deconvolved with a Wiener filter to show the performance of the corrected mask.

1.2.2 Optimisation methods using optical aberrations

A known amplitude of pupil aberrations can be used to minimise the search for a global minimum in optimisation routines. A combination of superimposed Zernike polynomial terms can generate a custom phase mask to be placed in the pupil of an optical imaging system [28]. A combination of aberrations chosen for the mask include Zernike aberration terms primary coma and trefoil, Z_7, Z_8, Z_9 and Z_{10} according to Mahajan notation [6]. The approach was numerical for a quasi-point source for $\lambda = 550$ nm in a microscope, the mean value of the visible spectrum. The proposed method allowed for an increase in the depth of field over a large bandwidth when simulated, even for off-axis objects.

The use of intrinsic aberrations in the lens can create a spatially invariant PSF without the need of a phase mask [29]. Bergkoetter and Bentley showed that a three element lens can be optimised to produce a similar effect to wavefront coding. A Cooke triplet was optimised in the presence of a comatic phase mask of opposite sign than desired for application. After optimisation the mask was removed and the depth of field was shown to be twice that of the starting design.

Originating in ophthalmic optics [30], spherical aberration can be used for EDOF. Mezouari and Harvey combined spherical aberration and defocus terms in a radially symmetric phase mask [31]. From this, Mouroulis showed that spherical aberration can be induced within a microscope lens and demonstrated to extend the depth of field while retaining resolution within half the maximum diffraction-limited spatial frequency [32]. An extension in depth of field equivalent to $\pm 0.88\lambda$ in terms of wavefront error was proven, showing comparable results without using phase elements. The lens is also achromatic over the visible band.

A compound system of lenslets was designed to simulate the eye as an imaging system. A spherical array of lenslets with deconvolution post-processing was shown to be capable of extending the depth of field and the field of view [33]. The spherical superposition compound-eye optics captures an optically superposed image of an object with different focusing distances and optical axes using a spherical array of erect imaging optics. Due to the three dimensionally space-invariant PSFs, deconvolution can be used to reproduce the image with a single filter from the simple captured image.

Utilising optical aberrations has been proposed for EDOF photographic optics [34]. Tang *et al.* discuss the value of using the PSFs to preserve the frequency content in the presence of defocus. Aberrated PSFs can consist of sharp edges that vary spatially with increasing anisotropicity with departure from the centre of the image. Therefore, defocus also varies spatially, where uneven high spatial frequency losses are observed in some directions. The authors use off-the-shelf photographic lenses to capture wide aperture images from short exposures. The depth of field is then extended by restoring the image blur using single lens calibration PSFs. Exploiting the aberrations from each object position the scene can be recreated.

For large object distances aberrations can be included in the design process while retaining a wide aperture diameter. A new design method was developed for a large depth of field lens with a large aperture diameter [35]. The lens has an F-number of 0.75, of focal length 58 mm and operates in the visible region. The depth of field of their lens ranges from 50 m to 3000 m, effectively extending to infinity. Raytracing through the system mimics the effect of wavefront coding, where the combined element aberrations simulate the effect of a phase mask. In this work the aberrations are optimised for aberration modulation. Experimental results show a larger signal-to-noise ratio on the image plane and the MTF plots are consistent over the EDOF region.

A central obscuration in the aperture is understood to assist in extending the depth of field of imaging systems. Obscuring the aperture is not ideal for low light applications. Chu *et al.* designed a glass plate whose thickness varies with annular zone [36]. This pupil partitioning of a conventional camera lens induces an unbalanced OPD through the optical system. Experimental evidence shows the relative invariance to the PSF to a change in object position. It is noted that a loss of contrast is observed from the partitioned element.

1.2.3 Hybrid methods using polarisation and scattering

Exploiting polarisation allows for non-conventional EDOF techniques. Chi *et al.* uses polarisation to extend the depth of field [37]. Polarisation states can be

modified at the aperture of an optical system to achieve greater image quality. In Chi's method a configuration is described, where the polarisation is rotated by 90° for a portion of the aperture and kept the same for the remaining aperture, where the PSF is a combination of the circular aperture and ring aperture PSFs. There is no interference between polarisations in orthogonal directions, and so this 'coded aperture' is comparable to the addition of two singular apertures. This principle can be applied for unpolarised and linearly polarised light. Using this approach of coded aperture with polarisation the extended depth of field imaging of a diffraction limited lens can be achieved without completely sacrificing detector light intensity. This is especially advantageous for low light level imaging.

The field of microscopy has been known to successfully use this extended depth of field for difficult imaging purposes. Chromatic aberration has been used to dissect images as a function of depth [38]. A system with strong chromatic aberration disperses light into tissue and enables volumetric imaging for non transparent tissues.

The scattering properties of an optical element in the pupil can offer an alternative to amplitude and phase variations. Cossairt *et al.* employ a diffuser element to the lens pupil [39]. Diffusers, like phase plates are relatively non-absorbtive and preserve intensity. The authors formulate diffusion as a kernel which is applied to a light field. This kernel guides the design of the diffuser which produces a depth-invariant PSF. The theory was tested using a Canon 450 D sensor and 50 mm f/1.8 Canon lens with deblurring algorithms.

Birefringent lenses produce effects that can alter DOF [40] [41]. A birefringent lens positioned between two linear polarisers has the ability to preserve Strehl ratio across a depth of focus [42]. In the case that the crystal optic axis of the birefringent material is perpendicular to the principle axis of the lens, the optical system behaves as a bifocus lens with proper orientation of the polarisers. Varying the birefringent lens parameters can alter the separation between the foci [40], where both foci are shifted equally on both sides from the Gaussian image plane. The Sparrow criterion of resolution is employed for finding the optimum separation of the two foci, the first and second derivatives of the combined intensity pattern disappear such that there exists no curvature between the two point intensity distributions [43]. Fulfilling this condition, the Strehl ratio versus defocus remains

constant over a wider region than a conventional lens with an identical PSF (IPSF) with a constant Strehl ratio.

1.2.4 Dedicated optical elements

Physical movement of optical elements within an optical system can facilitate an increase in the usable depth of field. Such mechanical modifications can refocus the optical system for direct imaging or assist in capturing multiple images with varying depths in a scene to be computationally fused post-capture.

The simplest physical modification that one can employ to extend the depth of field, or refocus an imaging system is to introduce a solid plate element with a refractive index $n_1 \neq n_0$, where n_0 is the medium surrounding the optical system. For most imaging systems n_0 is air and has a value of 1. Wang *et al.* presented a simple solution to extend the depth of field of an imaging microscope with a series of glass plate elements of various thicknesses [44]. A shift in focus is directly proportional to the thickness of the plate introduced, shown in Fig. 1.7. Eleven plates with thickness increasing in increments of 1 mm are mounted on a rotary disk. Twelve images are captured of a test target, one with each plate and one image without any plate. The EDOF image is generated by computationally combining the captured images.

Electronically controlled tunable lenses are commonly incorporated into optical systems to reposition the image plane. Electrically tunable focusing liquid crystal (LC) lens shows promise in increasing the DOF of an endoscope [45]. The LC lens can be tuned to be a positive or negative lens by altering the spatial distribution of the effective refractive indices and thereby effectively imaging different objects from various distances onto the detector. This increase in depth of field can also positively affect the spatial depth perception of the scene. Chen and Lin designed an endoscopic system which is optimised for effective aberration correction consisting of a polariser, an LC lens and an imaging lens module. For three separate discrete lens powers of the LC lens, the total depth of field of the endoscopic system ranges from 76.4 mm to 12.4 mm maintaining an acceptable contrast. The experiments show that depth of field is doubled compared to a standard optical setup.

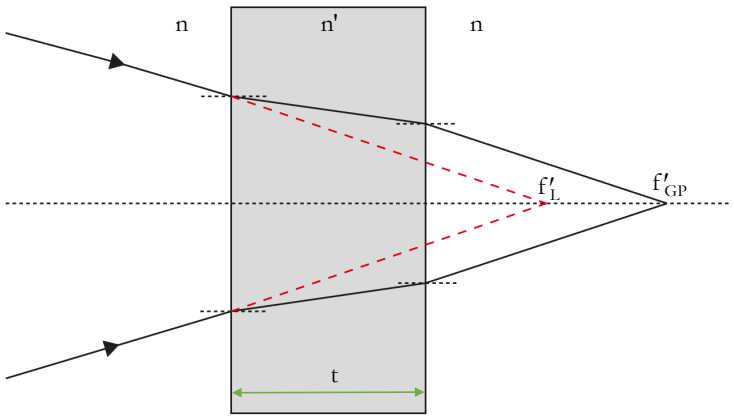

Figure 1.7: Shift of focus by parallel glass plate where the longitudinal shift is determined by the thickness of the glass plate $\Delta f = t(\frac{n'-1}{n'})$.

The advantage of LC lenses over liquid lenses is that the aperture diameter is not limited by the surface tension at a liquid-liquid interface found in liquid lenses. This characteristic is ideal for low-light applications and fast optical systems such as mobile phone cameras. Galstian *et al.* exploit the potential of tunable LC lenses for motion-free autofocus for mobile phone applications [46]. The tunable LC lens is positioned at the aperture stop with diameter up to 2 mm. The compound lens module shows an improvement in spherical aberration by a factor of two and maintaining an acceptable image quality for near object distances at 10 cm. The authors highlight the low-cost manufacturing of maximum 0.05 US dollars, which is desirable for integrating an autofocus solution into cameras dedicated to the consumer market.

Liquid crystal multi-lens arrays (LCMLA)s have been shown to aid EDOF by making wavefront measurements [47]. Two LCMLAs are each divided into 2x2 sub-regions and stacked. The layered LCMLAs allow for two objects to be imaged at different depths within the same scene by applying different voltage signals to each area. The EDOF scene is therefore reconstructed by stitching the clearest sub-images with the sub-region composite wavefront.

An alternative to mechanical movement is to apply heat across the optical elements to increase the depth of field [48]. Sheil utilises plastics characteristic of

low thermal conductivity to show that defocus can be introduced by heating an optical element. A plastic F/2 gradient index (GRIN) plate with a fixed focus is chosen as the high thermal resistance of plastics are desirable. Heating the plate to $50°C$ for 0.4 s yields visible improvement of the consistency of the MTF for the object distances nearest to the plate. The author addresses that this approach is not intended for rapid refocusing but rather as a low-cost solution for high accuracy tuning.

In cases where mechanical movement is not desirable or feasible, the optical system can be designed to include designated elements intended for a particular application. Such elements may trade spatial parameters such as field of view to achieve a more acceptable DOF. One approach to extend the focal segment of an optical system is to introduce a refracting axicon into the optical system [49]. This utilises the traditional sense of the refractive axicon, where the EDOF effect is required along the optical axis. The authors place an axicon before the CCD, with the planar side faced toward the object and apex positioned on the optical axis pointed to the CCD plane. It can be shown that for an object moving longitudinally along the optical axis, all rays that emerge from the lens are optimally refracted toward the CCD by a finite incident ray height on the axicon which is determined by the object position. This is only true for a selected range of object distances, where the image contrast is preferable at larger object distances. A variation in object position generates a change in the structure of the PSF across the image, which in turn causes an undesirable loss of contrast in these regions. Weiner filtering is employed to increase spatial resolution of the image in these regions.

A split pixel method uses a single microlens array positioned in front of a single detector [50] . The microlens array is designed in two halves, one having a longer focal length than the other. The first half acts as a traditional plenoptic camera where 50% is transmitted through the first beamsplitter angled at 45° and the remaining 50% reflected to the second 45° beamsplitter on the other half of the sensor. The second beamsplitter is purely reflective. The aperture of the system matches only half the sensor size. Objects located at a near object position will fall in focus on the second microlens array with a blurred image produced by the first microlens array. Objects positioned further away are in focus on the first

microlens array and blurred on the second microlens array. The image is taken from the sharp pixels and one array compensates for the loss of resolution in the other.

Digital image restoration can be an undesirable requirement in real-time imaging systems or high-speed imaging systems. Therefore, an optical solution that is free from post-processing would be beneficial in such imaging applications. Ben-Eliezer *et al.* propose an all-optical imaging system consisting of a combination of sixteen Fresnel lenses, that are spatially multiplexed and mutually exclusive [21]. The optical system is designed such that each Fresnel lens works with the the primary imaging lens to produce a sharp image for a given object distance. Summing the effect of all the Fresnel lenses the DOF can be extended. The authors state that the resulting image has a reduced resolution whereby no post-processing was applied to the captured images. However, the image remains sharper than an image from a clear aperture imaging system of comparable pupil size. The design is limited in imaging by the use of a single wavelength but is sufficient for the application of a barcode reader.

Alvarez lenses are a well established system consisting of a pair of optical elements used for adjustable focus in ophthalmic optics. The combination of lenses provide a variation in optical power with lateral shift with one lens with respect to the other [51]. Ojeda-Castañeda *et al.* induced defocus into a photographic optical system with an Alvarez-Lohmann element pair [52]. The Lohmann lenses come from the invention of an alternative lens pair with a cubic profile that was aimed at zoom lens systems rather than defocus [53]. The variable focus lens is used to compensate for the focus error of imaging objects beyond the standard depth of field of the optical system. The proposed technique preserves the full aperture maintaining a constant intensity and does not affect the lateral magnification of the optical system. Multiple images capture the scene with varying levels of defocus and are superimposed to generate the EDOF image. An Alvarez-based diffractive optical element (DOE) was developed to accommodate high speed refocusing with the use of a galvo-mirror [54]. The diffractive Alvarez element is divided into sub-elements, whereby a given combination of the sub-elements generates a change in optical power. The galvo-mirror images one subsection onto another in a $4-f$ configuration, where the combination is then imaged by a CCD.

This approach avoids the traditional lateral displacement of the elements while offering an optical power variation of $\pm 50D$.

Zhou *et al.* demonstrate the advantage of laterally translating a phase mask in the pupil of the optical system to introduce defocus [55]. The authors relate the lateral shift in cubic phase mask to the induced system defocus such that a defocus map can be generated. The theoretical proposition is realised with an F/4 cubic phase mask coded lens where the acceptable defocus range lies between $\pm 4\lambda$, whereby the images are reconstructed after capture. This approach claims to avoid errors that typically arise in directly shifting the ideal image plane. Although lateral translations of the masks gives rise to distortion and edge effects.

1.2.5 Computational methods

Computational enhancement of consumer imaging is increasingly attractive as it can provide a low-cost solution which can be improved incrementally with few or no modifications to the optical system. Post-processing algorithms are discussed in this section where the digital reconstruction approaches are featured as the main theme. Most approaches to computational EDOF are facilitated by some form of spatial adjustment, and only mentioned where necessary.

The DOF is often limited by the optical system. Even in systems with large F-numbers, where the ratio of the diameter to the focal length has a large value (e.g. F# $\geq$ 10), optical aberrations can limit the usable DOF. Computational algorithms can assist in minimising some of these limitations.

Focal sweep is a technique in which the focal plane is translated during through the image exposure. Employing such a method of image capture produces a space-invariant PSF that also is quasi depth-invariant [56]. This PSF is then used to deconvolve the image to achieve an increased depth of field without sacrificing the signal to noise ratio. Catadioptric imaging systems are known to have residual astigmatism and field curvature which causes a spatially varying blur in the image. For a single spherical mirror and an single-lens reflex (SLR) F/2.8, 50 mm lens combination, it is observed that the shape of the IPSFs are almost depth independent although spatially varying as the focal plane is shifted along the optical axis [57]. The range in which focal sweep is applied is limited to the preservation

of high frequencies and limiting image artefacts that arise from deconvolution. Yokoya *et al.* determine the optimal sweep range from the amount of astigmatism tolerated by the optical system. A feasibility study of the proposed theory showed that if the image sensor is translated over a distance of 0.69 mm, the spherical mirror-lens combination has a usable DOF retaining a sharp image from 0.3 m to 10 m when deconvolved with the IPSF. This approach has also been demonstrated on a parabolic mirror and for an off-axis parabolic mirror.

Cossairt *et al.* employed a chromatic inspired focal sweep and is termed by the authors as Spectral Focal Sweep (SFS) [58]. A doublet lens was used for SFS where the parameters were optimised to generate a large amplitude of axial chromatic aberration and minimise other residual aberrations. Optimisation generates a range of discrete focus positions for consecutive wavelengths where the PSF of the SFS camera is the continuous sum of concentric disks scaled as a function of wavelengths. For fifty sampled wavelengths, the authors simulate a PSF for twelve depth locations, where the range is chosen so that the magnitude of spot defocus of the center wavelength is the same as the maximum chromatic defocus. The image is then deconvolved using a Weiner filter. While the study shows promise for both greyscale images and colour imaging, it is documented that artefacts are introduced to the reconstructed image when applied to narrowband spectra.

Axial chromatic aberration assisted EDOF has been applied to fields such as microscopy and commercial imaging. DxO (DxO, France) proposed a technique of colour transportation to extend the DOF across colour channels [59]. This approach appears to increase the longitudinal chromatic aberration such that for a given object distance, at least one colour plane of the RGB image lies in-focus. The lens is designed in such a way that the red image is in focus for objects at infinity, green image for intermediate distances, and blue is sharp for close objects. A sharpness comparison across colours can give a relative estimation of the object distance and can allow for correct choice of digital filters with the information received from the object distance. The processing steps include estimating the depth map. The depth map guides the image filtering, where the regions of blur in one image is compensated by copying the high frequencies from the sharpest image to the others. Following the sharpness-transportation step, all the images have a comparable MTF, which in turn resembles the MTF of the lens at the optimal

focus. Restoration algorithms can be applied to improve the MTF further and filters to remove noise, but is not necessary.

A combination of image exposures and focus distances provides more information to faithfully recreate a scene with a large DOF and high dynamic range. Qian and Gunturk combine focus stacking and high dynamic range (HDR) imaging to produce an extended depth of field and dynamic range from a set of images with a range of various exposures over a variation of focus positions [60]. The focus stacking procedure is independent of exposure value. The process follows a pixel by pixel weight calculation for photometric and spatial registration. Focus stacking is then applied to images of different exposure levels. A standard HDR creation algorithm is used to generate a focused image with an accurate exposure with respect to the reference image.

Stereo imaging has become increasingly popular in mobile devices. The low cost sensors found in these devices can be used to generate EDOF effects in a smartphone [61]. Image pairs are captured by two adjacent cameras conjugated to different object positions. The images can then be combined to obtain low-resolution disparity maps, that is the pixel difference between the two stereo images. The map is then upsampled and combined with the raw image to create light fields.

Developments in the area of image reconstruction constantly improve the suppression of artefacts that arise as a consequence of subtle variations in PSF caused by defocus. Complimentary kernel matching is a technique proposed by Zammit et al. based on capturing two images with different phase masks that respond differently to defocus thus producing complimentary PSFs [62]. Complimentary kernel matching restores the images by deconvolution using the PSFs corresponding to a uniform defocus and spatially varying defocus which creates a disparity map between the images. Both simulation and experimental results are in agreement for producing artefact free imaging even in the case of large amounts of defocus.

The depth of field can be extended using both amplitude and phase modulation of the pupil function [63]. Bagheri *et al.* found that amplitude modulation is best suited to extending the total or traditional depth of field, while phase modulation is more suited to partially extending the DOF. The methodology

uses a combination of an annular aperture for amplitude modulation and the cubic, fourth and fifth order for phase modulation. A combination of the two modulations did not increase the MTF, however phase modulation alone made it possible. Amplitude modulation performs well when a small increase in DOF is required, generally 1 wave of defocus, and preserves spatial frequency in all directions. Alternatively, phase modulation performs well when a large increase in DOF is needed (few waves of defocus) and preserves spatial frequency on some line segments, referred to as extending the partial DOF.

Focus stacking is heavily dependent on capturing a stabilised sequence of images. Zhang developed a novel method which uses focus stacking in a hand held device despite changes in position and focus [64]. Hand held cameras are difficult to stabilise and therefore traditional focus stacking cannot be used. For a stack of images captured over a variation of focus positions, the inertial measurement unit of the phone can be used to select suitable images for combination. Images aligned in such a way that pixels in focus at a certain object position can be fused. An improvement in global sharpness is seen when comparing to other image fusing methods.

Neural networks are becoming increasingly popular in image registration and computational imaging. Elmalem *et al.* proposed applying deep learning to train the imaging system to restore phase mask coded images to achieve an extended DOF [65]. The phase element is encoded to induce axial chromatic aberration, which creates defocus in each image yielding a variation in depth. Traditionally, the phase element is designed first, and then the image is restored. Here, the design of the phase mask is incorporated in the training of the convoluted neural network. This is realised by using the parameters, radii and phase, of the mask as weights for the neural network. In doing so, a comprehensive system design is achieved. The authors discuss the ease of introducing such an approach to existing lens systems, while showing an improvement in reconstructed image sharpness and a tenfold reduction in runtime compared to previous phase modulated approaches.

Combining a stack of images for EDOF is well-established in the field of post-processing. However, a single image captured at maximum aperture has been shown to yield EDOF with high resolution. A complex amplitude mask can be applied during pre-processing, which eliminates the requirement to capture

a stack of images [66]. The mask consists of a cubic-phase mask and Gaussian amplitude filter, which helps to reduce the system sensitivity to focus errors, as the Gaussian amplitude filter decreases the MTF oscillations induced by the cubic phase mask. The combination of filters shows a reduction in the modulation of the system, amount of light collected, therefore post-processing is recommended. A field programmable gate array (FPGA) was used to demonstrate the feasibility of this EDOF approach. The experimental study illustrated the susceptibility of the system to noise-contamination, which in turn can affect the post-processing stage. Although contamination may be reduced by the promise of this approach to be adjusted for other implementation platforms.

Edge blur is a concern when reconstructing images in computationally assisted EDOF imaging techniques. A technique posed by Piao *et al.* use multi-focus elemental imaging to capture images from different perspectives over a range of focal lengths to create an all-in focus image [67]. The spatially varying images are geometrically aligned so that the objects are exactly overlapping in the scene. The EDOF image is then formed by fusing the aligned images.

1.3 Thesis Motivation

Section 1.2 gives an overview of the field of EDOF imaging to the best of the author's knowledge. Currently, processes such as zoom and refocusing are carried out computationally in mobile devices. These implementations are usually cost-beneficial and easy to implement. When considering a single camera, digital alternatives to zoom and refocus are not computationally intensive. However, with the increased number of cameras and sensors embedded in mobile devices the computational power to facilitate all processes can overload the device thus slowing its operation. From an optical perspective, these digital substitutions for zoom and refocus are undesirable as the image quality is reduced along with a decreased signal-to-noise ratio. As fore-mentioned, these miniature camera modules are fitted with a voice coil motor (VCM), which adds cost to the manufacturing and production. This cost is not desirable for multiple imaging modules.

Design restrictions in producing these modern commercial imaging systems

suggests that new approaches are needed to optically address the limitations relieving computational power and lowering the module cost.

The aim of this thesis is to develop methods of extending the depth of field using optical design in whole or in major part. By doing so, optical design can lead to a cost-effective solution for multiple camera module devices while also lowering the power consumption of the device.

1.4 Thesis Outline

The content of this thesis is presented in the following layout:

- **Chapter 2** provides an introduction to optical aberrations and aberration balancing. The foundations of aberration theory are discussed whereby the reader can gain an understanding of the underlying principles of the methodologies used in the following chapters.
- **Chapter 3** is based on the concept that dual-flash illumination can be utilised to extend the depth of field in a simple plano-convex singlet lens. An analytical method is introduced for designing a dual-wavelength imaging system where the criteria and limitations are clearly evaluated.
- **Chapter 4** addresses the challenge of imaging two irises over an extended depth of field. The design is based upon the principle that the irises are always positioned off-axis, only varying in field angle with object distance from the lens. Sacrificing the central field offers an increase in usable field of view, that is where the MTF for the fine details of the iris remains about the pre-fixed spatial frequency criterion. The key element in this design is an optical plate whose thickness profile displaces all image points to a region within the CCD depth of focus.
- **Chapter 5** introduces a novel smartphone lens element. The element is a standard rotationally-symmetric widefield lens. The novelty lies in the location of the lens within the device housing. The proposed design uses the corner of the device to anchor the front element. This lens orientation

does not limit the TTL of the lens by device thickness. EDOF can then be achieved by vignetting the field and including a small refocusing mechanism.

- **Chapter 6** discusses the conclusions of the project and summarises the contribution of the author to the field of optical design and suggests possible future work.

Chapter 2

Optical Aberrations

2.1 Introduction to Aberrations

An optical system is considered to be ideal if all rays originating from any object point P on the $\xi - \eta$ plane converge to one point P' in the $\xi' - \eta'$ plane satisfying Fermat's principle. This condition states that light travelling from point P to P' takes a stationary path. A minimum optical path is an example of a stationary path and is described as the time taken for light to travel from P to P':

$$t(PP') = \frac{1}{c} \int_{P}^{P'} n dl, \tag{2.1}$$

where n is the RI of a homogeneous medium and dl is the geometrical path length along all line elements of the ray [68; 69]. The integral in Eq. (2.1) is known as the optical path. The coordinates of point P and P' are proportional to one another under ideal imaging conditions.

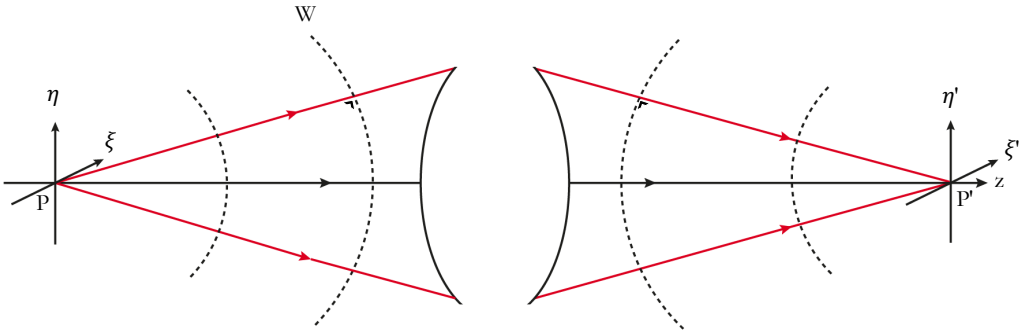

Figure 2.1: Principle of ideal imaging using both rays and wavefronts.

Wavefronts are surfaces of equal time from the point object, denoted by W in

Fig. 2.1. Rays are constructs that are perpendicular to wavefronts and are used in geometrical optics to trace light through the optical system.

Paraxial optics refers to an approximation valid in a narrow region with small ray heights relative to the optical axis, where the ray angle is assumed to be $i \cong 0$, shown in Fig. 2.2. In the paraxial region the optical system performs under ideal imaging conditions. Due to the small angle approximation, Snell's Law can be simplified to $ni = n'i'$ for rays propagating close to the optical axis. Outside this region the non-linearity of sine arises with the increase of angle i described by a Taylor expansion series [11; 70]:

$$\sin i = i - \frac{i^3}{6} + \frac{i^5}{120} \ldots, \tag{2.2}$$

where i is plotted in radians shown in Fig. 2.2. Paraxial approximations do not faithfully represent the ray path through an optical system. To do so, finite ray heights must be considered, where optimal performance is governed by aberration theory.

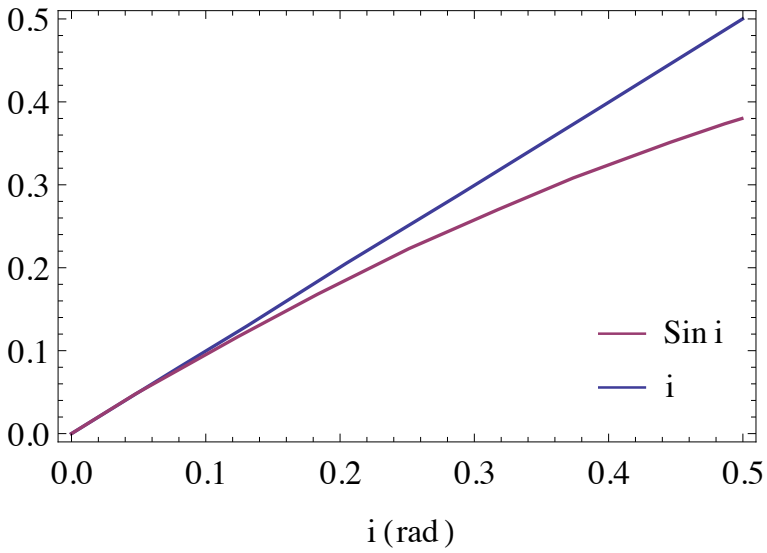

Figure 2.2: Non-linearity of sine with small positive values for i as described by Eq. (2.2).

The term aberration refers to optical effects in optical systems, that prevents attaining perfect imaging. There are many approaches of describing optical aberrations, which include wavefront perturbations, angular ray aberrations, trans-

verse ray aberrations and longitudinal ray aberrations. Sections 2.2 and 2.3 introduce the monochromatic aberrations through wave and geometrical approaches. Traditionally monochromatic optical aberrations are classed in families; namely spherical aberration, coma, astigmatism, distortion and field curvature where the emphasis of discussion is on the primary aberrations with a brief mention of higher orders. Chromatic aberrations are discussed separately in Section 2.5. This is simply because of their wavelength dependency. Chromatic aberrations are second order wave aberrations, but are often grouped with fourth order monochromatic aberrations as they have similar magnitude. It is important to note that all aberrations experience chromatic effects although the magnitude is often negligible compared to their monochromatic effects.

The art of optical design is effective aberration balancing to achieve the desirable imaging quality. Balancing aberrations refers to minimising the variance or rms wavefront error (WFE) and transverse ray aberration (TRA). However, in some cases the aberrations are utilised as another design parameter in the optical system. In general, the number of degrees of freedom available in the optical system will determine the effective aberration balancing. The reason for this becomes evident by further examining aberration constructs discussed in Sections 2.4 and 2.5.

2.2 Wave Aberrations and the Aberration Function

An aberrated wavefront is characterised by its deviation from the reference sphere in the exit pupil of the optical system. The optical path length (OPL) along a real ray is:

$$W(x, y) = [Q_0 Q], \tag{2.3}$$

where the points Q_0 and Q are points at which the real ray intersects the reference sphere and aberrated wavefront respectively, shown in Fig. 2.3. This statement is valid as the wave propagates by Helmholtz equation [68].

The measure of image quality of an optical system can be characterised by three main metrics. The choice of metric depends on the amount of aberration

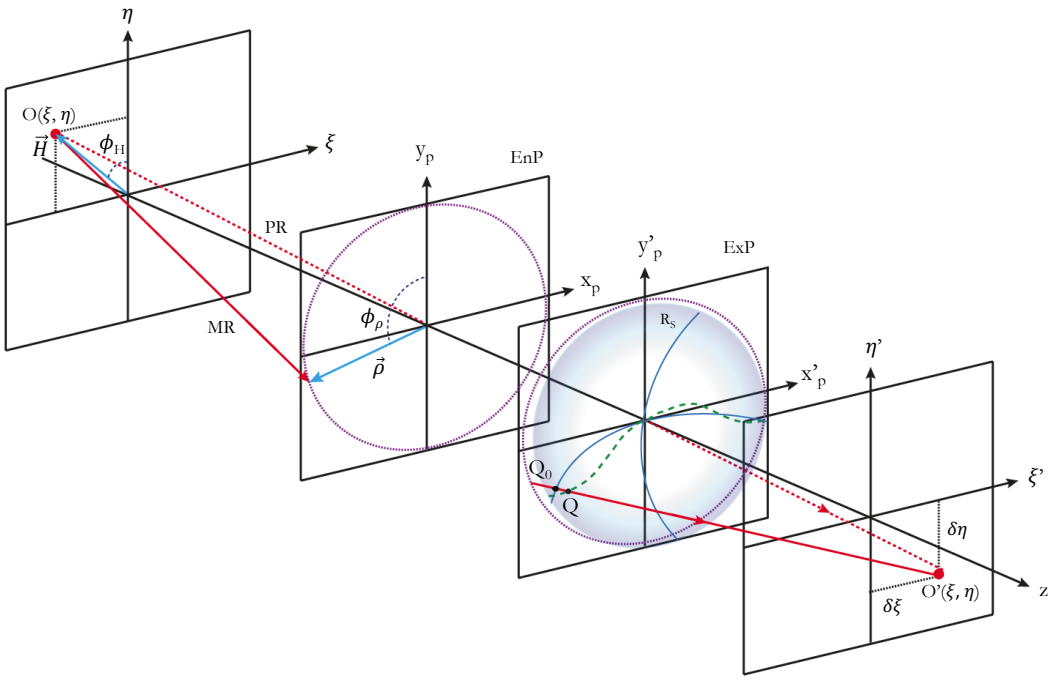

Figure 2.3: Propagation of the marginal ray (MR) and principal ray (PR) from object space to image space where there exists a rotationally symmetric optical system between the EnP and ExP.

present. Spot diagrams are geometrical metrics for image quality. That is, the intersection of ray position with the image plane is shown for all rays. Diffraction is not considered in this case and so are used to depict large amplitudes of aberrations. However, the Airy disk is calculated and overlaid on the plot to show the relative ray position with respect to the ideal diffraction limited image. The OTF is chosen to assess image quality when residual aberrations appear in the $1 - 2\lambda$ range. Section 1.1 provides further information on the OTF and the advantage of its use in photographic optics. For high performing optical systems, such as those approaching the diffraction limit, the Strehl ratio can be employed. The Strehl ratio is the ratio of the measured PSF intensity to the ideal PSF intensity. Photographic lenses do possess diffraction limited quality, and therefore shall not be discussed further.

A standard way of quantifying the performance of an imaging system is to consult the ability of the system to produce an image spot on the image plane,

known as a spot diagram. The coordinate of the centroid ray is described as:

$$\Delta x_c = \frac{1}{N}\sum_i \Delta x_i \quad \text{and} \quad \Delta y_c = \frac{1}{N}\sum_i \Delta y_i, \tag{2.4}$$

where N is the total number of rays traced and i is the index of the rays. Often the rms spot diagram is considered in the presence of field aberrations that produce non-rotational spot diagrams or in the presence of large aberrations. The rms spot is the root mean square deviation from the centroid ray position (x_c, y_c) on the image plane:

$$\Delta r_{rms} = \sqrt{\frac{1}{N}[(\Delta x_i - \Delta x_c)^2 + (\Delta y_i - \Delta y_c)^2]}, \tag{2.5}$$

and the first approximation in the geometrical model of the spot diagram is $D_{spot} = 2\Delta r_{rms}$ [71].

The WFE of an optical system is commonly expressed in two forms, by the P-V and rms WFE. The P-V WFE is the distance between the maximum and minimum points on the wavefront and is written as:

$$W_{PV} = W_{max}(x_p, y_p) - W_{min}(x_p, y_p). \tag{2.6}$$

For clarity (x_p, y_p) are used to denote pupil coordinates in this chapter as the variable u is reserved for paraxial ray angles in keeping with raytracing notation. The variance of the wavefront can be expressed as:

$$\sigma^2 = \langle W^2 \rangle - \langle W \rangle^2, \tag{2.7}$$

where $\sigma = W_{rms}$, which can be expanded to describe the rms WFE of the optical system in terms of the ExP with an area A_{ExP}:

$$W_{rms}(x_p, y_p) = \sqrt{\frac{1}{A_{ExP}} \int\int \left[W(x_p, y_p) - \bar{W}(x_p, y_p)\right]^2 dx_p dy_p}, \tag{2.8}$$

and the mean wavefront is $\bar{W}(x_p, y_p) = \frac{1}{A_{ExP}} \int\int W(x_p, y_p) dx_p dy_p$. Peak-to-valley and root mean square WFE do not possess information about spatial frequency content, which have a large effect on the PSF structure in the presence of optical aberrations.

An optical system can be described surface by surface with an aberration function similar to Eq.(2.3). The concept of studying the optical path length

between two points along a trajectory was introduced by W.R. Hamilton [72; 73]. The aberration function $W(\overrightarrow{H}, \overrightarrow{\rho})$ gives the geometrical wavefront deformation in the exit pupil as a function of the normalised field and aperture vectors denoted by $\overrightarrow{H}$ and $\overrightarrow{\rho}$ respectively. The field vector is located in the object plane and defines the starting position of the ray, whereas the aperture vector is typically located in the exit pupil. The aberration function is scalar and involves the dot products of the field and aperture vectors in combinations that describe a rotationally invariant system; $\overrightarrow{H} \cdot \overrightarrow{H}$, $\overrightarrow{H} \cdot \overrightarrow{\rho}$ and $\overrightarrow{\rho} \cdot \overrightarrow{\rho}$ [2; 71; 74]. The dot product depends on the magnitude of the vectors and on the cosine of the angle between them. The wavefront can be expanded as a power series with the variables introduced such that a complete description of the wavefront is written as:

$$W(\overrightarrow{H}, \overrightarrow{\rho}) = \sum_{j,p,m,n} (W_{k,l,m})_j (\overrightarrow{H} \cdot \overrightarrow{H})^p (\overrightarrow{H} \cdot \overrightarrow{\rho})^m (\overrightarrow{\rho} \cdot \overrightarrow{\rho})^n, \tag{2.9}$$

over all surfaces j, where the sub-indices p,m,n represent integers $k = 2p + m$, $l = 2n + m$ and the coefficients are denoted by $W_{k,l,m}$ and the indices k, l, m in each coefficient describe the algebraic power of the field, pupil and azimuthal angle between the vectors. The sum of all aberration terms over all surfaces j is inclusive of all orders and gives the total wavefront aberration. The variable l has a positive integer value, not including zero, where $l - m = 2n \geq 0$.

The order of a wave aberration term is denoted by $i = 2(p + m + n)$, which is always an even order in wave aberration notation, and is equal to the degree in the object and pupil coordinates [75]. Each order contains N terms, where $N = (i + 2)(i + 4)/8$ [2], for $i = 4$ then $N = 6$. The piston terms for each order are included in this calculation but are usually omitted from aberration tables. Ray aberrations have odd ordering as they are taken from the derivative of the wave aberration.

Each combination of vectors can be reduced to their cartesian coordinates, the field vector is written as $(\overrightarrow{H} \cdot \overrightarrow{H}) = H^2 = \xi^2 + \eta^2$, here ξ and η are normalised field heights along the x and y planes respectively. The aperture vector is $(\overrightarrow{\rho} \cdot \overrightarrow{\rho}) = \rho^2$, where ρ is a dimensionless parameter that describes the normalised radial coordinate in the pupil $0 \leq \rho \leq 1$, given as $\rho = (r_p / r_{p,max})$ where $r = \sqrt{x_p^2 + y_p^2}$ and $r_{p,max}$ is the maximum pupil radius. The cross terms can be simplified $(\overrightarrow{H} \cdot \overrightarrow{\rho}) = H \cdot \rho \cdot \cos(\phi_H - \phi_\rho)$, whose cartesian coordinates are

Ord	Aberration	Vectorial	Scalar	p	m	n
0	Piston	W_{000}	W_{000}	0	0	0
2	Mag	$W_{111}(\vec{H}\cdot\vec{\rho})$	$W_{111}\eta\rho\cos\phi$	0	1	0
2	Focus	$W_{020}(\vec{\rho}\cdot\vec{\rho})$	$W_{020}\rho^2$	0	0	1
4	Spherical	$W_{040}(\vec{\rho}\cdot\vec{\rho})^2$	$W_{040}\rho^4$	0	0	2
4	Coma	$W_{131}(\vec{H}\cdot\vec{\rho})(\vec{\rho}\cdot\vec{\rho})$	$W_{131}\eta\rho^3\cos\phi$	0	1	1
4	Astigmatism	$W_{222}(\vec{H}\cdot\vec{\rho})^2$	$W_{222}\eta^2\rho^2\cos^2\phi$	0	2	0
4	Field Curv	$W_{220}(\vec{H}\cdot\vec{H})(\vec{\rho}\cdot\vec{\rho})$	$W_{220}\eta^2\rho^2$	1	0	1
4	Distortion	$W_{311}(\vec{H}\cdot\vec{H})(\vec{H}\cdot\vec{\rho})$	$W_{331}\eta^3\rho\cos\phi$	1	1	0
6	Spherical	$W_{060}(\vec{\rho}\cdot\vec{\rho})^3$	$W_{060}\rho^6$	0	0	3
6	Lin. Coma	$W_{151}(\vec{H}\cdot\vec{\rho})(\vec{\rho}\cdot\vec{\rho})^2$	$W_{151}\eta\rho^5\cos\phi$	0	1	2
6	Astigmatism	$W_{422}(\vec{H}\cdot\vec{H})(\vec{H}\cdot\vec{\rho})^2$	$W_{422}\eta^4\rho^2\cos^2\phi$	1	2	0
6	Field Curv	$W_{420}(\vec{H}\cdot\vec{H})^2(\vec{\rho}\cdot\vec{\rho})$	$W_{420}\eta^4\rho^2$	2	0	1
6	Distortion	$W_{511}(\vec{H}\cdot\vec{H})^2(\vec{H}\cdot\vec{\rho})$	$W_{531}\eta^5\rho\cos\phi$	2	1	0
6	Obl. SA	$W_{242}(\vec{H}\cdot\vec{\rho})^2(\vec{\rho}\cdot\vec{\rho})$	$W_{242}\eta^2\rho^4\cos^2\phi$	0	2	1
6	Obl. SA	$W_{240}(\vec{H}\cdot\vec{H})(\vec{\rho}\cdot\vec{\rho})^2$	$W_{240}\eta^2\rho^4$	1	0	2
6	Ell. Coma	$W_{331}(\vec{H}\cdot\vec{H})(\vec{H}\cdot\vec{\rho})(\vec{\rho}\cdot\vec{\rho})$	$W_{331}\eta^3\rho^3\cos\phi$	1	1	1
6	Ell. Coma	$W_{333}(\vec{H}\cdot\vec{\rho})^3$	$W_{333}\eta^3\rho^3\cos^3\phi$	0	3	0

Table 2.1: Zero, second, fourth order and sixth order aberrations listed in vector and scalar notation including indices.

simply $\eta x_p + \xi y_p$, where $y_p = r\cos\phi$ and $x_p = r\sin\phi$. The coefficients ($W_{k,l,m}$) represent the maximum amplitude of each aberration expressed in wavelengths. A list of conversions from wavefront scalar notation to vector notation is provided in Table 2.1. Vector notation is useful for describing non-meridional tilts and decenters and thus is normalised according to Nodal aberration theory [75]. However, vector notation is not always necessary in optical design as is the case with rotationally symmetric optical systems. That is, aberrations calculated on the meridional plane are sufficient to describe the wavefront aberration. Therefore, for simplicity the scalar notation will be used to further describe the aberrations in this chapter, where the field coordinate will be described in terms of normalised y coordinate η. In this way, ξ is set to zero, where the aberration function can be described by a combination of rotational invariant variables in polar coordinates $W(\rho^2, \rho\eta\cos\phi, \eta^2)$. The aberration function can be expanded as a power series

to be:

$$W(H,\rho,\phi) = \sum_{j,k,m,n} (W_{k,l,m})_j H^k \rho^l \cos^m \phi, \tag{2.10}$$

over all surfaces denoted by j. Equation (2.10) takes a scalar form of Eq. (2.9).

Fourth order wave aberration terms are described by the ordering $i = 4$ and are commonly known as the primary or Seidel aberrations and are listed in Table 2.1. Sixth order wave aberrations consist of nine terms (N=9) and are known as the Schwarzschild aberrations. There are two notable additions to the sixth order aberration terms, oblique spherical aberration and elliptical coma. Oblique spherical aberration is the sum of $W_{242} + W_{240}$ terms and does not possess axial symmetry due to the field dependence. In cases when aberration correction is not satisfactory using primary aberrations, one can use the fourth order and sixth order wave aberrations to balance each other. Higher orders than sixth begin to deviate from expected pupil and aperture aberrations [71].

First and Second Order Aberrations

The piston terms only appear in the wave aberration notation as they are examined, when considering the phase of the wavefront. Piston is uniform across the pupil due to the reference sphere and wavefront passing through the center of the pupil therefore the OPD must be zero at the origin of the pupil [76]. Magnification is simply a term to account for a change in magnification. The wavefront coefficient is often set to zero as first order optics can accurately describe its effect. Tilt of the wavefront is addressed in Section 2.4 along with distortion.

The defocus wave aberration is a longitudinal shift in image position that can be compensated by refocusing. Consider that for an optical system with a circular exit pupil, the radius of curvature for the reference sphere f is approximately equal to the radius of curvature l' for the spherical wave W, where both wavefronts are located in the exit pupil and centered on two finite separate image positions that lie on the optical axis. For $f \approx l'$ then defocus can be described as:

$$\delta W \approx -\frac{n_i}{2}\left(\frac{1}{f} - \frac{1}{l'}\right)\rho^2, \tag{2.11}$$

It is important to note that defocus wave aberration has the opposite sign to the longitudinal defocus of a optical system, illustrated in Fig. 2.4.

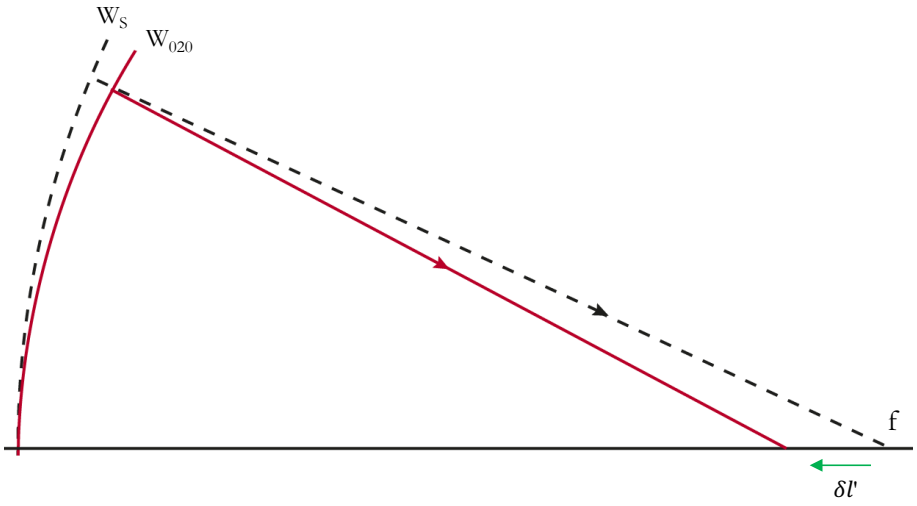

Figure 2.4: Positive defocus wave aberration yields a negative longitudinal defocus.

2.3 Geometrical Aberrations

Geometrical aberrations are calculated by tracing ray paths through the optical system. The minimum number of rays that can be traced through an optical system to locate the image position is two, the PR and the marginal ray (MR). Aberration-free systems traced with geometrical approaches can generate image spots that are not limited by diffraction effects of the lens, producing an ideal image.

Derived from the eikonal equation, the theorem of Malus and Dupin states that a pencil of rays remain at a normal to the wavefront after reflection or refraction for any number of surfaces [68]. From this theorem it can be deduced that the wavefront perturbation can be translated to ray paths for generating transverse ray aberrations. The ray aberration in the image plane is the spatial derivative of the wavefront multiplied by the radius of curvature. Therefore, integrating under the TRA curve gives the corresponding wavefront aberration. If the angle between the ray and the normal to the reference sphere is $\delta U'$, then the y-component of the TRA can be written as:

$$\delta\eta' = \delta U' R. \tag{2.12}$$

Since rays are perpendicular to the wavefront, it can be deduced that $\delta U'$ is

the angle between the normal to the wavefront and the normal to the reference sphere [76]:

$$\delta\eta' = -\frac{R}{n'}\frac{\partial W}{\partial y}. \tag{2.13}$$

Aldi derived equations expressing the TRA components on a finite ray with respect to the paraxial principal ray. The most applicable use of Aldi's theorem is that the formulae can be broken down into the individual surface contributions which makes locating the source of an aberration extremely useful as the formulae include all orders of the aberration polynomial [71]. The theorem becomes a powerful design tool when implemented with Seidel theory.

Seidel aberrations are generally the first introduction to aberration theory. Although imaging is considered ideal for rays traced in close proximity to the optical axis, Seidel aberration theory describes the primary aberrations in terms of ray heights and angles within the paraxial region. The Seidel sums also indicate the dependency of each aberration on the MR, PR, RI and Lagrange invariant. The refraction invariants for a surface are described as $A = n(hc + u)$ and $\bar{A} = n(\bar{h}c + \bar{u})$, where the bar indicates the dependency of the PR, u is the paraxial angle with respect to the optical axis, c is the surface curvature commonly known as the inverse of the radius of curvature $c = 1/R$ and h is the paraxial ray height. The Lagrange invariant is denoted as $H = A\bar{h} - \bar{A}h$ and holds for all optical systems [76], this is not to be confused with the field variable in wave notation. The Seidel aberrations are listed in Table 2.2.

Aberration	Seidel Sum
Spherical aberration	$S_I = \sum A^2 h\Delta(\frac{u}{n})$
Coma	$S_{II} = -\sum \bar{A}Ah\Delta(\frac{u}{n})$
Astigmatism	$S_{III} = -\sum \bar{A}^2 h\Delta(\frac{u}{n})$
Petzval curvature	$S_{IV} = -\sum H^2 c\Delta(\frac{1}{n})$
Distortion	$S_V = -\sum \frac{\bar{A}^3}{A} h\Delta(\frac{u}{n}) + \frac{\bar{A}}{A} H^2 c\Delta(\frac{1}{n})$
Axial chromatic aberration	$C_I = \sum Ah\Delta(\frac{\delta n}{n})$
Lateral chromatic aberration	$C_{II} = \sum \bar{A}h\Delta(\frac{\delta n}{n})$

Table 2.2: Seidel aberrations where the sum is taken for all surfaces in the optical system.

The total aberration in this representation is the summation for each surface.

Seidel sums can be used to estimate the wave aberration with the help of the conversion Table 2.3. It is important to note that Petzval curvature is only listed in the Seidel aberrations. A more complete discussion of Petzval curvature and field curvature can be found with the introduction of astigmatism.

Aberration	Wave Coefficient	Seidel Coefficient
Spherical Aberration	W_{040}	$\frac{1}{8}S_I$
Coma	W_{131}	$\frac{1}{2}S_{II}$
Astigmatism	W_{222}	$\frac{1}{2}S_{III}$
Field Curvature	W_{220}	$\frac{1}{4}(S_{III}+S_{IV})$
Distortion	W_{331}	$\frac{1}{2}S_V$

Table 2.3: Wave aberration coefficient to Seidel notation for the primary monochromatic aberrations.

The wavefront aberration can therefore be written for the monochromatic third order aberrations in terms of the Seidel coefficients as [77]:

$$W = \frac{1}{8}S_I\rho^4+\frac{1}{2}S_{II}\eta\rho^3\cos\phi+\frac{1}{2}S_{III}\eta^2\rho^2\cos^2\phi+\frac{1}{4}(S_{III}+S_{IV})\eta^2\rho^2+\frac{1}{2}S_V\eta^3\rho\cos\phi \tag{2.14}$$

In general, this description of the wavefront is very advantageous for generating good starting designs before optimisation.

2.4 Monochromatic Aberrations

In this section each aberration family is described individually assuming all other aberrations in the system are zero. That is, unless specifically outlined otherwise.

Spherical Aberration

Primary spherical aberration, denoted by the wave aberration as $W_{040}\rho^4$, is considered a longitudinal aberration, where the absence of a field variable implies that the aberration is invariant over the field of view.

Presenting as a variation in focus position as a function of marginal ray height, a caustic is generated in the focal region, as illustrated in Fig. 2.5. The effect on

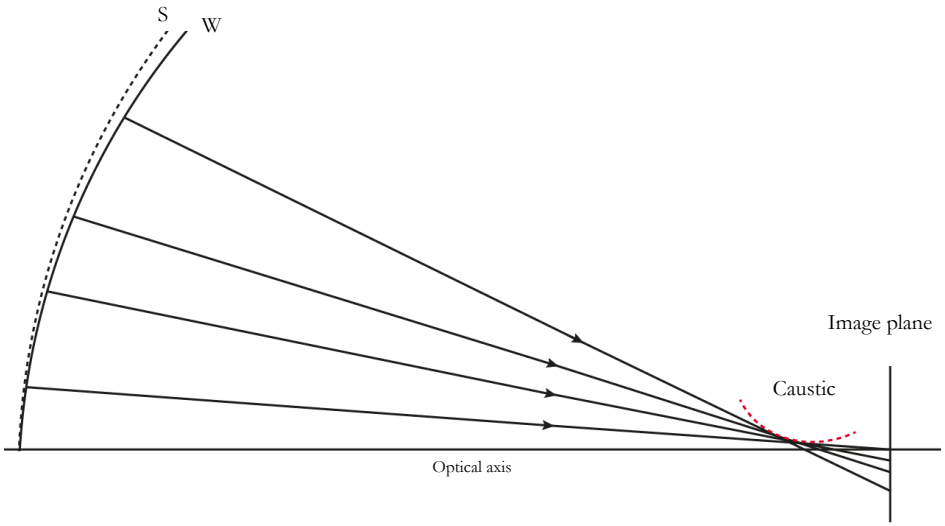

Figure 2.5: Spherical aberration with caustic along the optical axis ($+z$) shown close to the focal plane.

the spot is axially symmetric about the principal ray as the sagittal and tangential rays have an identical profile in the pupil due to the lack of an azimuth dependence ϕ. The TRA for spherical aberration is:

$$\delta\eta'_{SA} = \frac{-4W_{040}R}{n}\rho^3. \tag{2.15}$$

It is important to understand the origin of spherical aberration in order to balance or avoid its effects. The paraxial Delano equation for longitudinal spherical aberration contributions $\Delta l'_{SA}$ at a surface can be expanded for finite ray heights as derived by Kingslake [78]:

$$\Delta l'_{SA} = -\sum_{j=1}^{i} \frac{ni\Delta Q'}{n'_i u'_i \sin U'_i} = -\sum_{j=1}^{i} \frac{2\overline{PA}[\sin\frac{1}{2}(I'+U)\sin\frac{1}{2}(I'-I)]A}{n'_i u'_i \sin U'_i}, \tag{2.16}$$

where $\Delta Q = Q' - Q$, $ni = A$ the refraction invariant for the marginal ray and the relation of the angles being $I' - I = U' - U$ and $I' + U = I + U'$ shown in Fig. 2.6. The variables Q and Q' are described by the ray angle $Q' = R(\sin I' - \sin U')$ and $Q = R(\sin I - \sin U)$ [71].

Interpreting the surface contributions in Eq.(2.16) frames four conditions, for which a surface is free from spherical aberration. The first condition relates to the chord $\overline{PA} = 0$ in Fig 2.6, where the ray passes through the vertex of the surface.

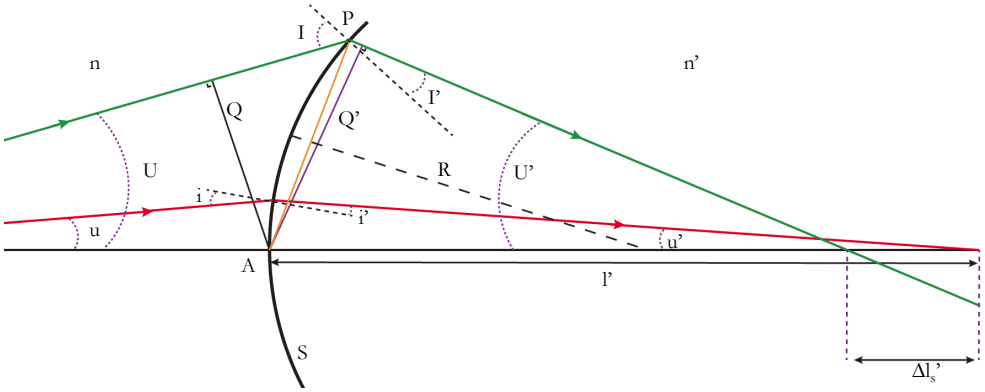

Figure 2.6: Spherical aberration contribution at a surface S, where the red ray is the paraxial ray, green ray corresponds to a marginal ray at a finite height, the orange line is the chord $\overline{PA} = 0$ and the purple and red lines correspond to Q and Q' respectively. Recreated with reference to Eq.(2.16).

For the induced spherical aberration to be zero the incident ray has the ray angles $U = -I$ and $U' = -I'$.

The second condition states that the spherical aberration contribution is zero at a surface for angles $I' = I$, meaning that the marginal ray does not undergo refraction at the surface, this is not true for all rays in the bundle. The third condition is the paraxial case of the second condition, where $ni = 0$ and the paraxial marginal ray does not undergo refraction. A surface with this characteristic is called a concentric surface. The fourth and final condition is an important rule in optical design where $I' + U = 0$. This relation is called the aplanatic condition and arises when the optical system is free from all orders of spherical aberration and coma. The Abbe sine condition for a finite conjugate optical system is:

$$\frac{n \sin U}{n' \sin U'} = \frac{u}{u'} = const, \tag{2.17}$$

where U is the finite aperture angle, u is the paraxial aperture angle. The sine condition assumes that Fermat's principle is satisfied and does not hold unless there exists no spherical aberration in the optical system. For an infinite conjugate lens the condition can be written as:

$$f' = -\frac{y}{\sin U'}, \tag{2.18}$$

where f' is the focal length of the lens and y is the ray height in the aperture.

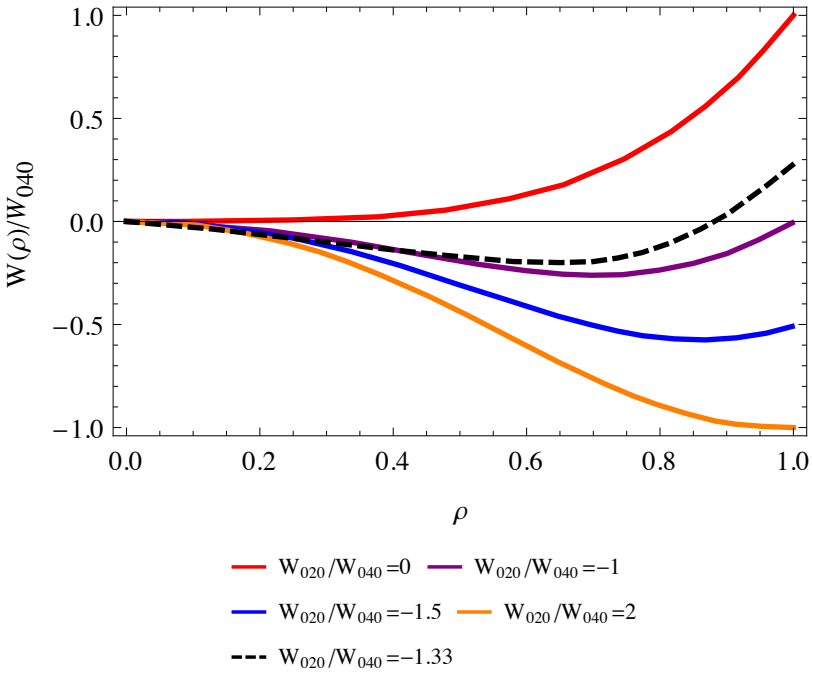

Figure 2.7: Spherical aberration and defocus balance. The value of $W_{020}/W_{040} = -1.33$ represents the smallest rms spot radius for spherical aberration in the pupil [2].

Spherical aberration and defocus can be combined to balance the presence of spherical aberration in the system. The paraxial image point is often not the position of best image quality. By inducing defocus the location of smallest spot size can be found, this is known as the disk of least confusion [76]. This effect is not only important for finding the best image position, but also for strategically blurring the image for computational EDOF methods, discussed in Chapter 1. The aberrated wavefront with spherical aberration and defocus present is written as the sum $W(\rho) = W_{040}\rho^4 + W_{020}\rho^2$, where the ratio of defocus to spherical aberration is plotted as a function of normalised pupil radius demonstrating the balancing effect of the two aberrations in Fig. 2.7. The y-axis is scaled as $W(\rho)/W_{040} = \rho^4 + (\frac{W_{020}}{W_{040}})\rho^2$ [2]. In most cases $W_{040} \approx -W_{020}$ would give a good balance so that $W(\rho) = 0$.

A priori knowledge and understanding of surface contributions give rise to conditions in which spherical aberration can be minimised within the lens. These approaches include varying ray geometry and minimising the discrepancy between

the incident ray and surface normal. Fermat's principle, introduced in Eq. (2.1) can be applied to correct all orders of spherical aberration. This can be carried out in a finite conjugate system by ensuring the optical path of all rays from the object point to the image point are equal. Increasing the number of spherical surfaces, where refraction is split between the successive lens surfaces, creates a more gradual refraction of the marginal ray. Gradual refraction can also be carried out by employing a GRIN lens, where the index variation of the lens causes refraction within the material reducing the overall spherical aberration. Increasing RI of lens material reduces spherical aberration in a thin lens, this dependency is seen by the presence of n in Eq. (2.16) and also in the Seidel sum formula. In some cases the lens can be split, where a small air-gap is introduced between two lenses if the surfaces have different radii of curvature, the OPL undergoes a change with increasing ray height and is ideal to correct spherical aberration. For a full clear aperture of fixed diameter spherical aberration can be minimised by modifying a spherical surface to a non-spherical shape such as a conicoid of revolution generally followed by a set of polynomial terms. The most common type is a polynomial aspheric surface, which has a sag (z) described by:

$$z(x,y) = \frac{c(x^2+y^2)}{1+\sqrt{1-(1+\kappa)c^2(x^2+y^2)}} + \sum_{k=1} a_k (x^2+y^2)^{k+1}, \tag{2.19}$$

where c is the surface curvature, κ is the conic constant, a_k is a constant. The second term is a power series sum over the normalised radial coordinate. Aspherical terms a_k have units of mm^{1-k}. Fermat's condition can also be used to derive the optimal sag profile for an aspheric surface. Position of the asphere in the lens will target different aberrations. An asphere located close to the stop can correct spherical aberration as all field angles are affected nearly equally. When necessary stopping down the aperture truncating the most peripheral ray zones, where spherical aberration is most prominent, is an extreme case of correction.

Coma

The second perturbation of the wavefront is coma. It is described by $W_{131}\rho^3\eta\cos\phi$. Primary coma is a field dependent aberration, where the linearity with field angle quickly limits the usable field of view unless corrected. This odd order field

aberration arises when the intersection of the rays is not symmetrical with respect to the principal ray. From the azimuth angle dependency, $\cos\phi$, the sagittal component of the wave aberration is often zero, and the tangential component has a dependency on the pupil radius as ρ^3. Coma's characteristic comet shaped image spot arises from the sagittal pupil section where the ξ'-component is zero and the η'-component is found to be similar in amplitude to the η'-component of the tangential pupil section. The ratio of the two sections are $1:3$, as seen in Fig 2.8.

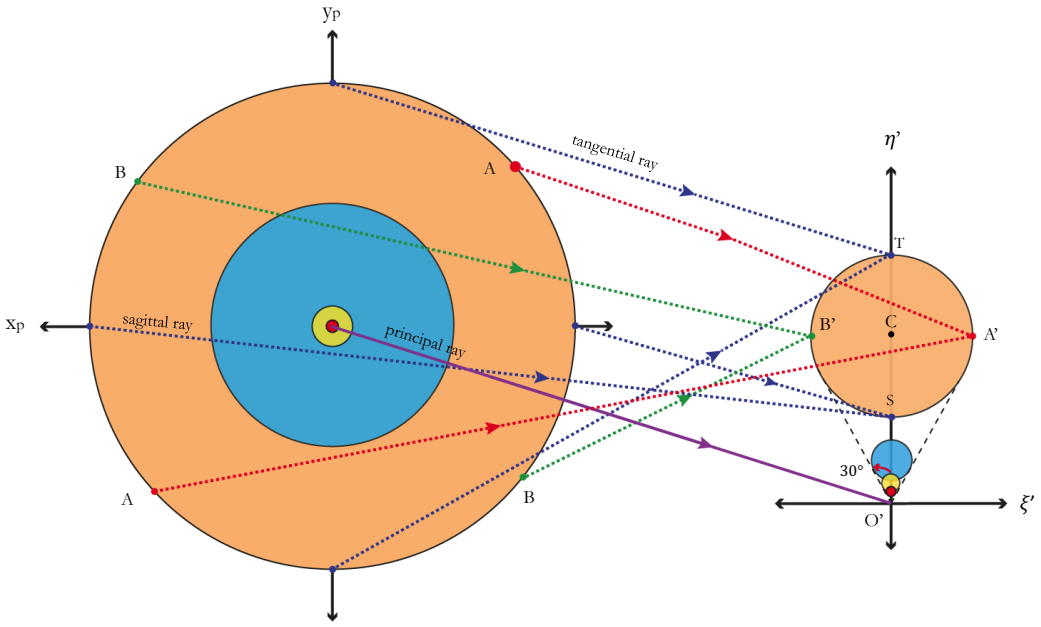

Figure 2.8: Ray construct from pupil to spot diagram.Wave aberration for coma, where the sagittal wave aberration is zero. The ray aberration for coma is non-zero.

Consider rays passing through the ExP with radius ρ, the principal ray is located at the Gaussian focus, while the marginal rays form a circle with a radius that is proportional to ρ^2. This circle is also decentered with respect to the principal ray position O' by a factor also proportional to ρ^2 [71]. The TRA for coma depicts this pupil dependency:

$$\delta\xi'_c = \frac{-R}{n} W_{131}\eta\rho^2 \sin 2\phi \tag{2.20}$$

and

$$\delta\eta'_c = \frac{-R}{n} W_{131}\eta\rho^2(2+\cos 2\phi), \tag{2.21}$$

where the sub-indices indicate the image point displacement in the presence of coma. The image circle occupies a region which is limited by segments of two straight lines at 30° angle to the radial direction and an arc of the largest aberration circle [68].

If the aplanatic condition is fulfilled for all aperture angles then the surface is free from all orders of spherical aberration and coma. In reality, this is difficult to achieve. The offence against the sine condition determines the transverse coma relative to the height of the paraxial principal ray yielding the residual aberration of that surface.

Aplanatic surfaces and lenses are characteristically free from coma. Symmetrical optical systems about the stop can correct coma as symmetry cancels aberrations with odd power in the field. It must be noted that in contrast, aberrations that possess field dependencies of even powers are additive in a symmetrical system. The stop shift equations are a well established approach, where the aperture stop position is utilised as a variable to minimise coma. This approach can only be applied if there is residual spherical aberration present described by the stop shift equation as the new value for coma can be calculated as S^*_{II}:

$$S^*_{II} = S_{II} = \delta E S_I, \tag{2.22}$$

where $\delta E = (\bar{h}_{new} - \bar{h}_{old})/h$ is the eccentricity with notation according to Table 2.2. In the case where spherical aberration is corrected, a shift of the stop position has no effect on coma.

For the stop positioned at the lens, the bending parameter can influence coma correction as coma depends on the principal ray described by the Seidel sum for coma in Table 2.2. Intentionally induced coma in a system by bending a lens can compensate the residual coma aberration elsewhere in the optical system. The presence of coma can be minimised by introducing tilt, although this is not correcting coma rather displacing the best centre of light concentration in the image point [79]. In more complex optical systems, where traditional approaches cannot be applied, such as fast lenses the introduction of a second aspheric surface

can be used for coma correction. Like the case of spherical aberration, coma correction can be distributed among several optical surfaces.

Astigmatism & Field Curvature

Astigmatism and field curvature are often grouped together as they share the same wavefront dependencies $\eta^2\rho^2$. If both W_{222} and W_{220} coefficients are non-zero the sagittal and tangential focal lines form curved surfaces. The degree of curvature of the tangential surface is determined by the signs and magnitudes of the coefficients generating a greater or lesser curvature than the sagittal [76] .

Astigmatism arises from a variation in sagittal and tangential focus positions. A single point in object space forms two separate line images, one at the sagittal and one at the tangential image planes. The tangential plane, also known as the meridional plane, lies in the $y-z$ plane containing the optical axis and the point object lying on the η axis [76]. The sagittal plane is perpendicular to the tangential plane and contains the PR.

If W_{222} is the only aberration present in the optical system, the rays from the tangential plane in the pupil will form a line image at T perpendicular to the tangential plane, i.e. on the sagittal plane. Similarly, the rays from the sagittal plane in the pupil will form a line image S on the tangential image plane, as illustrated in Fig. 2.9. The difference between the foci is the astigmatism present in the system. The segment TS increases with the square of the field and is known as Sturms interval [11].

The TRA for the tangential line image can be found from Eq.(2.13) for $\delta\xi'_A = 0$:

$$\delta\eta'_A = -\frac{2R}{n}W_{222}\eta^2\rho, \tag{2.23}$$

which has a length of $4RW_{222}\eta^2\rho/n$. For a variation in focus between focal lines the expression from Eq.(2.13) is rearranged so that $W_{020} = -(2R/n)W_{222}\eta^2$. The η variable vanishes and thus the rays converge to a line image along the ξ section.

Coddington derived equations to describe astigmatism in a ray bundle with infinitesimally small NA through a surface with skew angle of incidence [71]. These equations are:

$$\frac{n'\cos^2\bar{i}'}{l'_{tan}} = \frac{n\cos^2\bar{i}}{l_{tan}} + \frac{n'\cos\bar{i}' - n\cos\bar{i}}{R_{tan}} \tag{2.24}$$

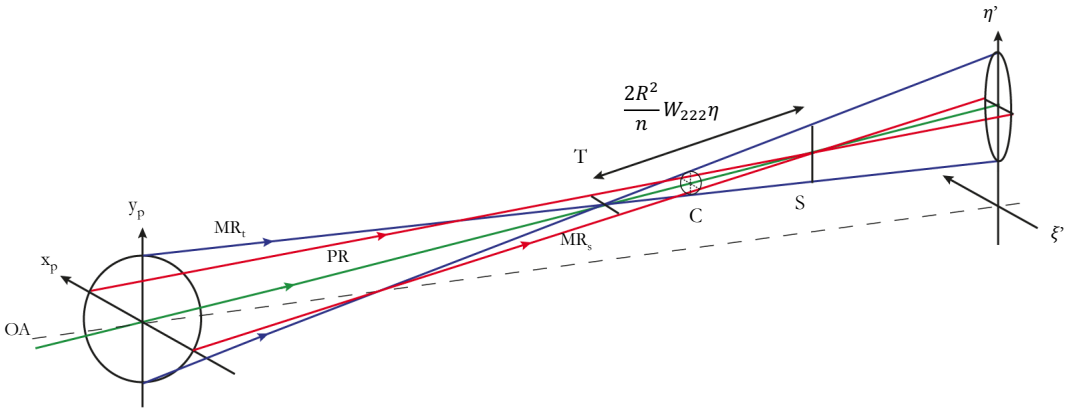

Figure 2.9: Formation of astigmatism where the PR is green, MR$_s$ is red and MR$_t$ is blue. The tangential and sagittal images are labelled by T and S, respectively.

and

$$\frac{n'}{l'_{sag}} = \frac{n}{l_{sag}} + \frac{n'\cos\bar{i}' - n\cos\bar{i}}{R_{sag}}, \tag{2.25}$$

where R is the surface radius and indices are denoted by n and n'. The intersection length before and after the surface for the small ray bundle in tangential and sagittal is measured along the principal ray. The only difference between Eqs. (2.24) and (2.25) is the incident principal ray angle ($\bar{i}$), so it can be understood that a change in $\bar{i}$ yields a change in astigmatism.

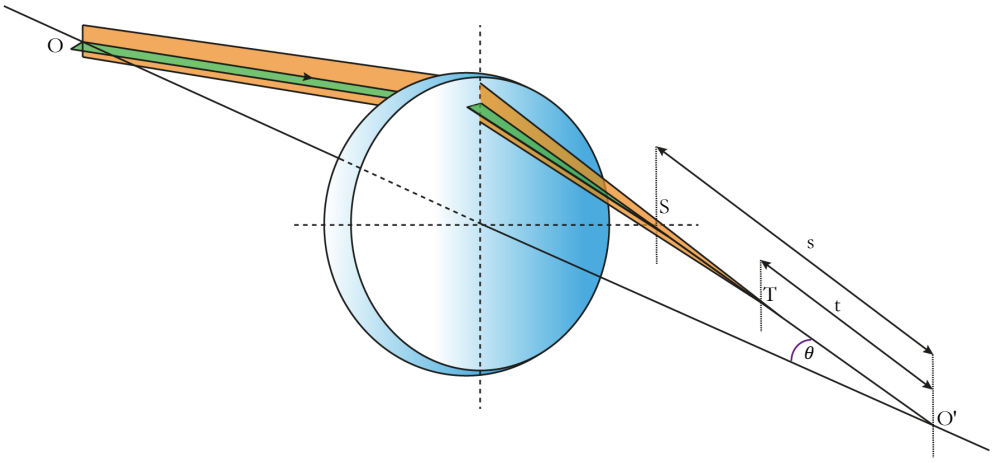

Figure 2.10: Criterion for quadratic field dependent aberrations traced as a small ray bundle through the pupil of the optical system.

As Fermat's principle and Abbe's sine condition ensure that an optical system is free from all orders of spherical aberration and coma, a criterion exists for correcting all quadratic field dependent aberrations. Satisfying the relation:

$$s(\theta) = \frac{t(\theta)}{cos^2(\theta)} = const, \tag{2.26}$$

where $t = O'T$ and $s = O'S$ illustrated in Fig. 2.10 [80; 81]. Equation (2.26) shows that the quadratic field dependent aberrations are affected by the center ray angle θ in image space, which corresponds to a pupil coordinate. From this relation the condition in Eq. (2.26) can be calculated for each point in the pupil similar to Fermat's principle and Abbe sine condition. Figure 2.10 shows the criterion for a finite object point. It is to be noted that Eq. (2.26) also holds for an object at infinity. Implementation of this principle uses Coddington's equations, where a thin bundle of rays is traced to obtain the tangential and sagittal image positions. Correcting all orders of spherical aberration, coma and quadratic field dependent aberrations requires a total of four degrees of freedom.

Bending of a lens to correct astigmatism is dependent on the stop position relative to the surface. The stop determines the principle ray angle which is critical for induced astigmatism. Therefore, the correctional ability of bending strongly depends on stop position. A shift of the stop position can minimise astigmatism, as shown by the third stop shift equation:

$$S^*_{III} = S_{III} + \delta E S_{II} + \delta E^2 S_I. \tag{2.27}$$

However, if spherical aberration and coma are corrected a stop shift has no effect on astigmatism. Cylindrical lenses are often used where the meridional power of the lenses varies to compensate astigmatism. The introduction of a third aspheric surface is often used for astigmatism correction and is usually placed away from the stop due to the astigmatic field dependency.

For an astigmatism-free lens, the tangential and sagittal image planes coincide. The image has a curved surface due to field curvature that arises from each lens contribution in the system. This is known as the Petzval surface. For a simple thin lens, the longitudinal distance between the ideal plane image surface and the Petzval surface is $\eta^2/2nf$, although the curvature can be altered due to the

presence of other aberrations. For a system of thin lenses with a small aperture the Petzval surface has a radius of curvature of:

$$\frac{1}{r_p} = -\sum_k \frac{1}{n_k f_k}, \tag{2.28}$$

where $n_{image} = 1$, the medium RI in image space is assumed to be air. The Seidel coefficient for Petzval curvature is S_{IV}. Generally not being considered for aberration correction, the Petzval condition can be used in generating starting designs for more complicated systems whose parameters are usually determined by paraxial optics. In reality, a lens generates a longitudinal positioning of images, where positive lenses produce image surfaces, which curve toward the lens while negative lenses produce image surfaces facing in the opposite direction. In the presence of primary astigmatism the Petzval surface serves only as a reference surface from which the sagittal and tangential images surfaces are measured.

As can be seen from table 2.4, the tangential astigmatism is associated with $3S_{III} + S_{IV}$, while sagittal astigmatism is only $S_{III} + S_{IV}$. The tangential surface is three times further away from the Petzval surface than the sagittal, illustrated in Fig.2.11(a). Balancing positive and negative power lenses of selected refractive indices minimises the field curvature in the image plane. The contribution that

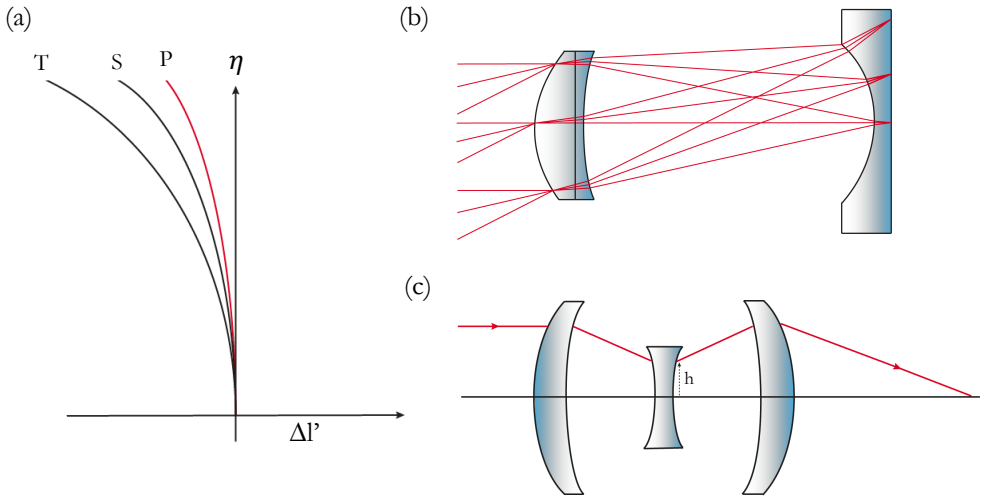

Figure 2.11: (a) longitudinal aberration for astigmatism and positive field curvature (b) field lens and (c) Cooke triplet.

Aberration	Wave	Seidel
Astigmatism	W_{222}	S_{III}
Petzval Curvature	$W_{220} - W_{222}$	S_{IV}
Sagittal Astigmatism	W_{220}	$S_{III} + S_{IV}$
Tangential Astigmatism	$W_{220} + 2W_{222}$	$3S_{III} + S_{IV}$

Table 2.4: Coefficients for astigmatism and Petzval curvature.

a lens element makes to the system is proportional to the product of its power and the height of the marginal ray. For a negative lens introduced in a suitable position the element power contribution can be substantial while the marginal ray height remains small. The additional contribution to the overall optical power is low despite having a significant influence on field curvature. A good example of such a design is the Cooke triplet illustrated by Fig. 2.11(c), where the negative element is located between two positive lenses reducing the field curvature [82].

Distortion

Distortion is a lateral displacement of the image point with respect to the paraxial image magnification. Distortion increases cubically with the field angle η described in Table 2.1 as an aberration of the PR $W_{331}\eta^3\rho\cos\phi$. Tilt in the wavefront generates a linear TRA, $\delta\eta$. Consider two spherical wavefronts with the same radius of curvature R, but having different tilt.

This tilt introduces a lateral offset of the image point. In reference to Fig. 2.14, where the image point is $\eta = z\tan\theta$ and the tilt in the wavefront is $w = \rho\tan\theta$. Differentiating both image point and tilt, the change in lateral image position and tilt is:

$$\delta\eta = z\sec^2\theta d\theta \tag{2.29}$$

$$\delta w = \rho\sec^2\theta d\theta \tag{2.30}$$

Solving Eqs.(2.29) and (2.30) for $\sec^2\theta d\theta$ and setting the expressions equal to each other, the relationship between wavefront tilt to lateral image position can be expressed as $(\delta\eta)/z = (\delta w)/\rho$ and rearranged to yield:

$$d\eta = \left(\frac{z}{\rho}\right)dw. \tag{2.31}$$

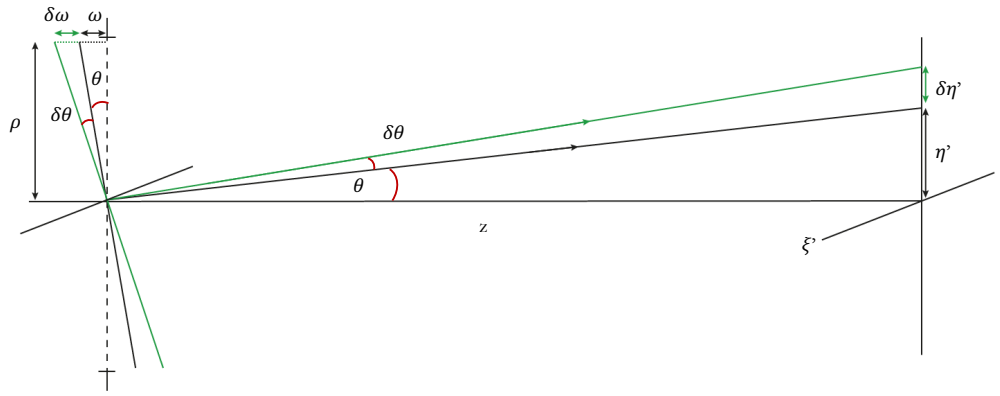

Figure 2.12: Tilt of the wavefront in the pupil. The wavefront radius is illustrated as planar for simplification.

If $z = f$ and $\rho = D/2$ with D being the finite diameter of the pupil, then it is clear to see that the lateral image displacement is directly proportional to the F-number and wavefront tilt in the pupil as described by $d\eta = 2(F\#)dw$ [83]. Recalling the equation for TRA in Eq.(2.13), this can be rewritten in terms:

$$\delta\eta' = -\frac{R}{\rho}W_{311}\eta^3. \tag{2.32}$$

Equation(2.32) can be multiplied across by a factor of $(\frac{2}{2})$ to encorporate the full pupil diameter:

$$\delta\eta' = -\frac{2R}{2\rho}W_{311}\eta^3. \tag{2.33}$$

The relation of $2R/2\rho = 2F\#$ and so the TRA is related to the linear tilt in the wavefront. When the tilt angle is $dw = -W_{311}\eta^3$, the field dependent tilt that is generated varies cubically over the field.

Distortion appears in two forms; barrel and pincushion named after their appearance. Sixth order distortion is identical in shape to fourth order. Distortion is independent of lens bending and conjugate position. It is interesting to note that distortion is proportional to spherical aberration in the exit pupil. For distortion to be independent of object position, then pupil spherical aberration must be zero such that $\tan\bar{U}'/\tan\bar{U} = constant$ for all field angles, where $\bar{U}$ and $\bar{U}'$ refer to the principle angle rays [71]. Distortion on the image plane is calculated by a simple formula:

$$Dist = \frac{y'_{real} - y'_{ideal}}{y'_{ideal}}, \tag{2.34}$$

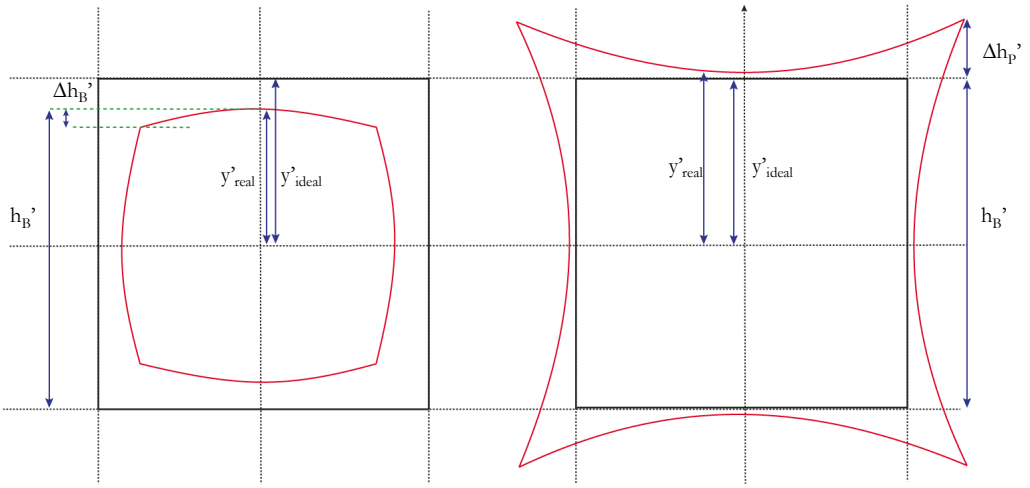

Figure 2.13: Distortion (a) barrel of hight h'_B and (b) pincushion with height h'_P.

where distortion can take the form of two shapes, which correspond to a positive or negative distortion value shown in Fig. 2.14. TV distortion is the amount of bending of the horizontal line $D_{TV} = \Delta h/h$. For a thin lens the distortion is heavily dependent on the stop position which is highlighted in Table 2.5.

Element Power (K)	Stop Position	PR height	Distortion
Positive	Behind	h<0	Positive
Positive	Front	h>0	Negative
Negative	Front	h<0	Negative
Negative	Front	h>0	Positive

Table 2.5: Distortion based on stop position for a thin lens.

2.5 Chromatic Aberration

For monochromatic light, the first five aberration families introduced in Section 2.2 have a RI variable that is generally a reference to the specific wavelength chosen. When considering polychromatic light, the dependency of RI with wavelength must be considered. Refractive index n of a material is the ratio of velocity

of light in a vacuum to the velocity of light in that material:

$$\frac{\lambda_0}{\lambda} = \frac{cf}{vf} = \frac{c}{v} = n \tag{2.35}$$

RI varies as a function of wavelength and is known as dispersion. For elements with positive optical power the focal position, both laterally and axially, varies spatially as a function of colour [83]. Therefore, images will be formed at discrete locations in image space for consecutive wavelengths.

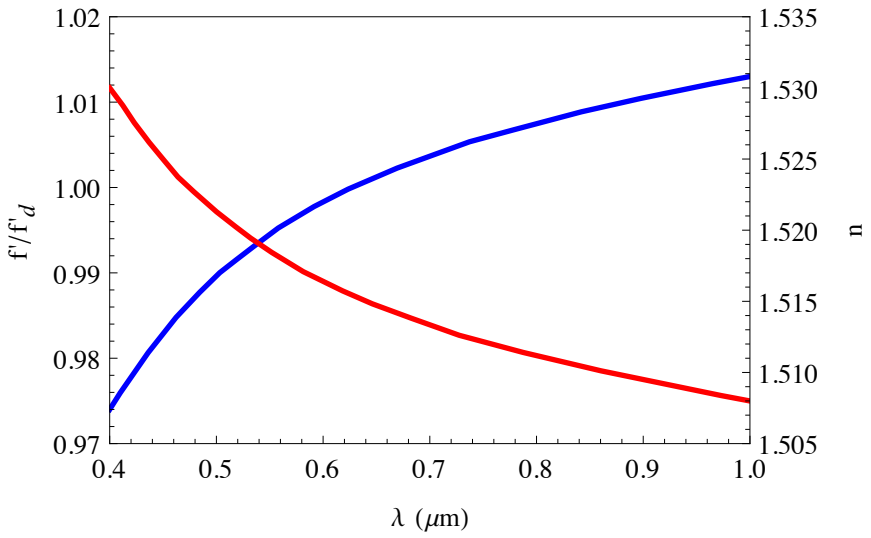

Figure 2.14: Variation of RI and focal length of a thin lens made from BK7 versus wavelength. The focal length is normalised by the focal length of the d line in the Fraunhofer spectrum.

All optical glasses and plastics have increasing refractive index with decreasing wavelength thus shorter wavelengths are refracted at larger angles than longer wavelengths:

$$\frac{dn}{d\lambda} < 0 \tag{2.36}$$

The mean deviation is measured from the incoming white light to the dispersed Fraunhofer d line, which lies between the F and C lines. The dispersiveness of a material is commonly described by the Abbe Number and defined as:

$$V = \frac{n_d - 1}{n_F - n_C} \tag{2.37}$$

where n_F, n_d and n_C are the refractive indices for the Fraunhofer F, d and C lines corresponding to $\lambda = 486.1$ nm , 589.3 nm and 659.3 nm respectively [68]. Optical glasses have Abbe numbers in the range of 10 to 120. A glass with a low Abbe number has a high dispersion and a glass with a high Abbe number has a low dispersion. The Abbe number is a relatively accurate measure of dispersiveness in the visible spectrum. However, as the Abbe number is weighted in the d line and therefore does not faithfully represent dispersion in the near infrared (NIR) range.

For polychromatic light refracted through a surface from one medium to another each wavelength undergoes dispersion described by Eq. (2.36). For a refracting optical surface such as a positive thin lens, the variation in refraction angle with wavelength gives rise to two effects on the image plane called LCA and transverse chromatic aberration (TCA). Primary chromatic aberrations appear in the paraxial approximation as the sum of the power in the pupil and field coordinate expansion is two, yielding the primary chromatic aberrations are second order wave aberration, and first order TRA.

For chromatic aberrations described in terms of wavefront aberration, the perturbations can be defined similarly to their monochromatic counterparts. The reference sphere in the exit pupil of the system for chromatic aberration is defined with wavelength λ and any departure from this reference wavelength $(\lambda + \Delta\lambda)$ will be termed a chromatic aberration with an OPD described by:

$$\delta W = [P_1 P_2], \tag{2.38}$$

where the reference wavefront in Fig. 2.15 is labelled P_1 and the aberrated wavefront P_2 [76]. The OPD in the pupil is measured along the ray between the P_1 and P_2. The ray may correspond to either of the two wavelengths such that the path length could be $n(P_1P_2)$ or $(n + \delta n)(P_1P_2)$, since $\delta n \ll n$, then the two are approximately equal [84].

The chromatic surface contribution for a single refracting surface can be derived from the thin lens equation with transverse magnification $M = \eta'/\eta = nl'/n'l$ to be:

$$\frac{\delta M}{M} = \frac{\delta \eta'}{\eta'} = \frac{\delta n}{n} - \frac{\delta n'}{n'}\frac{\delta l'}{l'} = \left(\frac{\delta n}{n} - \frac{\delta n'}{n'}\right)\frac{l'}{R}, \tag{2.39}$$

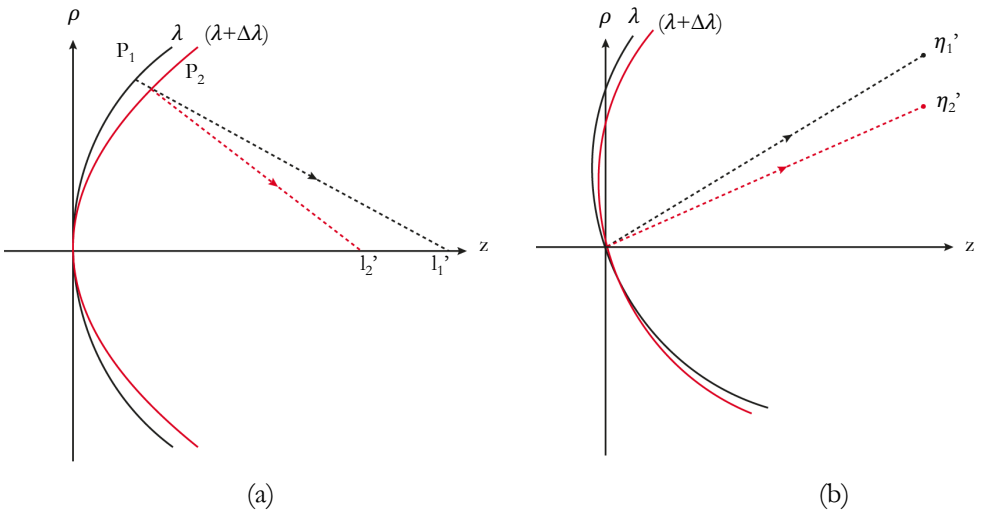

Figure 2.15: Axial colour as a wave aberration. The wavefronts are shown as spherical where the reference wavefront is coloured black and labelled λ while the aberrated wavefront is red and labelled $(\lambda + \Delta\lambda)$. The axis labels are ρ which represents pupil height and has an arbitrary value here, and $+z$ following the sign convention.

where $\delta\eta' = \eta'\delta M/M$ on the image plane describes the difference in principal ray height on the image plane $\eta'_\lambda - \eta'_{\lambda+\Delta\lambda}$ between η'_1 and η'_2 in Fig.2.15(b) showing that the fractional chromatic variation in magnification does not depend on image or object height. This chromatic variation in magnification is known as TCA or lateral colour. The variable $\delta l' = l'_\lambda - l'_{\lambda+\Delta\lambda}$ between l'_1 and l'_2 in Fig. 2.15 (a) is the longitudinal chromatic aberration. Transverse and longitudinal aberrations appear together in real optical systems, however to introduce them it is simpler to discuss them independently.

It can be more intuitive to understand the chromatic aberration surface contributions by looking at Seidel sums within the paraxial region. Recalling that LCA and TCA Seidel sums are:

$$C_I = \sum_j Ah\Delta\Big(\frac{\delta n}{n}\Big), \tag{2.40}$$

and

$$C_{II} = \sum_j \bar{A}h\Delta\Big(\frac{\delta n}{n}\Big), \tag{2.41}$$

it can be easily interpreted that surface contributions for chromatic aberration

are zero when the ray height is zero. For a surface that is concentric with the stop $\bar{A} = 0$, or for a surface that is concentric to the object/image the ray does not undergo refraction and therefore will not induce any chromatic effects.

The wavefront aberration coefficients for chromatic aberration can be converted to Seidel coefficients as shown in Table 2.6. The wavefront aberration, when considering the chromatic aberrations, can be written in terms of the Seidel sums found in Table 2.2:

$$W_\lambda(\eta, \rho, \phi) = \frac{C_I}{2}\rho^2 + C_{II}\eta\rho\cos\phi \tag{2.42}$$

Aberration	Wave	Seidel
Longitudinal Chromatic Aberration	$W_{020(\lambda)}$	$\frac{1}{2}C_I$
Transverse Chromatic Aberration	$W_{111(\lambda)}$	C_{II}

Table 2.6: Wave aberrations to Seidel notation for the primary chromatic aberrations.

The transverse expression for longitudinal chromatic aberration is:

$$W_{020(\lambda)}(h) = -W_{020(\lambda)}\tan U', \tag{2.43}$$

where U' is the marginal ray angle with the optical axis. Longitudinal chromatic aberration variation over the field should not be confused with lateral chromatic aberration. Generally a raytrace through the lens for multiple wavelengths is considered practical to determine the amount of chromatic aberration in a lens. Conrady developed a method for calculating chromatic aberration using one wavelength within certain limitations with exact raytracing [85]. The formula central to his method is:

$$W_\lambda = \sum_i \delta n_i (D_{PRi} - D_i), \tag{2.44}$$

where $\delta n = n'_F - n'_C$ for the visible spectrum, D_{PRi} is the length along the principal ray and D_i is the length along an other ray [86]. The summation in Eq. (2.44) extends over all spaces in the lens. It is noted that Conrady's formula applies to any chromatic variation in the optical system not just for LCA and TRA.

Transverse Chromatic Aberration

TCA also known as lateral colour is the chromatic change in magnification shown in Fig. 2.15(b). This effect arises from the chromatic variation of the principle ray and so has no presence if the principle ray passes through the centre of the lens, simply interpreted by the Seidel sum for C_{II}. The TRA for the displacement in image height as a function of λ can be described in terms of the wavefront aberration coefficient:

$$\delta\eta'_{\lambda} = -\frac{1}{n'u'}W_{111(\lambda)}, \tag{2.45}$$

where the positive value indicates a decreasing image size with increasing wavelength [76]. Every description of TCA includes variables outlining a variation in refractive index δn, which indicates the importance of a suitable material combination for lens groups within the lens. It is repeatedly discussed that TCA is dependent on the principal ray. Correction methods influencing the principal ray such as stop position can minimise the lateral chromatic effect. Symmetry about the stop can be applied due to the linear dependency on field. Higher orders of TCA will also be corrected by symmetry as they have an odd powered dependency in the field [71]. Stopping down the aperture has no effect on TCA as the aberration is independent of the aperture variable, the same is true for distortion.

Longitudinal Chromatic Aberration

Longitudinal chromatic aberration, also called axial colour, is a variation of image position with wavelength, simply a chromatic change in focus [86]. The distance between the two focus points indicates the amount of axial colour present. From Fig. 2.15(a), the distance between the chromatic image positions as described in Eq. (2.38) and so the change in focus at the image plane is denoted by Eq. (2.46). The displacement of the axial image position in terms of the wave aberration coefficient is written from interpreting Eq. (2.11):

$$\delta l'_{\lambda} = \frac{1}{n'u'}W_{020(\lambda)}, \tag{2.46}$$

u' being the marginal ray slope in image space. A positive value for $\delta l'_{\lambda}$ in Eq. (2.46) yields a focal shift toward the lens with an increasing RI. In the absence

of spherical aberration, a system illuminated with visible light, which has uncorrected LCA, forms a symmetrical spot surrounded with a purple halo arising from the blue and red light for a perfectly focused green image [82]. The image spot is rotationally symmetric about the optical axis.

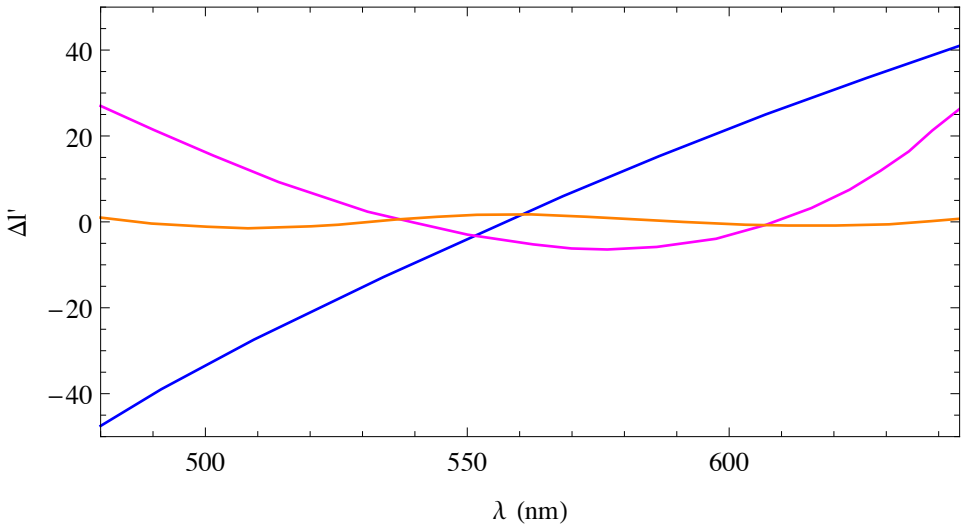

Figure 2.16: Residual chromatic aberration for three lenses with element powers denoted as positive (P) and negative (N): a BK7 singlet (blue), a P-N BK7-SF5 achromat (magenta) and a P-N-P FPL53-BAK1-SSKN5 apochromat (orange) where the magnitude of $\Delta l'$ is an arbitrary value scaled to fit all plots to the figure.

Figure 2.16 is a plot of the chromatic focal shift for three lenses. The variation in image distance $\Delta l'$ is an arbitrary value, as it is scaled to fit the plot. The chromatic focal shift for a singlet lens, plotted in blue, intersects the axis at a singular wavelength therefore graphically showing LCA about the image plane. Power combination is central for correcting LCA. Consider that the power of a thin lens in air denoted by K is written as:

$$K = (n-1)\left(\frac{1}{R_1} - \frac{1}{R_2}\right), \tag{2.47}$$

where R_1 and R_2 are the radii of curvature of the singlet lens. Equation (2.47) indicates that a single glass element does not have the available degrees of freedom to balance LCA, although LCA can be minimised with a low dispersive glass and

optimum radii selection. To correct LCA for two wavelengths, the variation in lens power ΔK must be negligible, which requires a minimum of two lenses of different materials. Ideally the value for ΔK would be zero, although this is not realistically feasible. The concept can be explained using thin elements of powers K_1 and K_2. The variation in optical power is ideally zero and so the criteria for minimising LCA can be described by:

$$K_{\sum} = \frac{K_1}{V_1} + \frac{K_2}{V_2} = 0, \tag{2.48}$$

where V_1 and V_2 are Abbe numbers of the two materials. It is the ratio of the Abbe numbers that controls the severity of the radii in the lens. If the variation between V_1 and V_2 is large, where the materials have a sufficient ratio, then the radii of curvature can have a weaker surface shape. Traditionally, one lens takes a positive shape and the other a negative and are arranged in a cemented doublet or air-spaced configuration.

Equation (2.48) generates the condition whereby an achromat can correct LCA for two wavelengths, shown in Fig. 2.16 by the magenta line crossing the image plane twice. The intersection points with the image plane ($\Delta l' = 0$) determine the corrected wavelengths. However, considering that visible light is represented by the F,d and C lines, the achromat is not corrected for green light d and so its residual is still present in the lens. This is referred to as the secondary spectrum. Calculating the extent of the secondary spectrum involves manipulation and reverse-engineering of Eq. (2.48), where the power of the lenses are equal for C and F lines $K_C = K = F$. The variation in power responsible for the secondary spectrum ΔK_{ss} between the corrected point and the residual image point is $\Delta K_{ss} = K_d - K_C$. The addition of another lens to balance the secondary spectrum requires a particular choice of glass which can be determined by the relative partial dispersion:

$$P_\lambda = \frac{n_d - n_F}{n_F - n_C}, \tag{2.49}$$

where the dispersion of the glass for C and F lines is established relative to the d line. A condition can be established from Eq. (2.49) which outlines the criteria for correcting three wavelengths using the total refractive power $K_1 + K_2 + K_3$:

$$T = V_{1+2} - V_3, \tag{2.50}$$

where V_{1+2} is the artificial Abbe number of the achromat. Reducing Eq. (2.50) into its constituent terms:

$$V_{1+2} = \frac{V_1(P_2 - P_3) + V_2(P_3 - P_1)}{P_2 - P_1} - V_3, \tag{2.51}$$

where the sub-indices refer to the element number [71]. The variable T is the measure of the distance between the Abbe number of the third element V_3 and the combined Abbe number of the achromat V_{1+2} on the glass map. Large values of T are the most effective. The correction ability of an apochromat is shown in Fig. 2.16, where the curve intersects the axis three times corresponding the corrected image points of lines F, d and C.

It is necessary to mention that axial colour exists beyond the chromatic variation of focal length. An example of this is spherochromatism; the variation of spherical aberration with wavelength. Other aberrations also exhibit chromatic effects although they are not considered as their impact is minimal on image quality.

2.6 Description of Optical Surfaces

The shape of an optical surface is referred to as the sagitta, or sag, of the surface. The sag is described as the distance of the surface from the vertex of the surface as a function of surface height y, shown in Fig 2.17.

The most common surface shape are spherical surfaces, which can be mathematically described as:

$$z(r) = \frac{cr^2}{1 + \sqrt{1 - c^2 r^2}}, \tag{2.52}$$

where $r = \sqrt{x^2 + y^2}$. A conicoid of revolution, often called a conic constant (κ), is a deviation from spherical surfaces that varies in eccentricity (ε):

$$\kappa = -\varepsilon^2 = \left(\frac{b}{a}\right)^2 - 1, \tag{2.53}$$

with a and b being the semi-axes of the surface. The radius of curvature of a surface at the vertex of $R = (\frac{1}{c}) = (\frac{b^2}{a})$, where c is the surface curvature. The shape of the surface can then be assigned to a conic constant as described in Table 2.7.

Conic constant (κ)	Surface shape
κ<-1	Hyperboloid
κ = -1	Paraboloid
κ=0	Sphere
κ> 0	Oblate ellipsoid
0>κ>-1	Prolate ellipsoid

Table 2.7: Conic constant values and related surface shapes.

Spherical and parabolic surfaces can be approximated to have equal sag for surfaces with equal radii of curvature R at the vertex and small surface heights, given as $z(y) = \frac{y^2}{2R}$. An optical surface with a conic constant that deviates from spherical can be described by:

$$z(r) = \frac{cr^2}{1 + \sqrt{1 - (1 + \kappa)c^2r^2}}. \tag{2.54}$$

A suitable choice of conic constant can reduce the use of excessive aspheric terms or other polynomial type terms. When designing optical surfaces with more com-

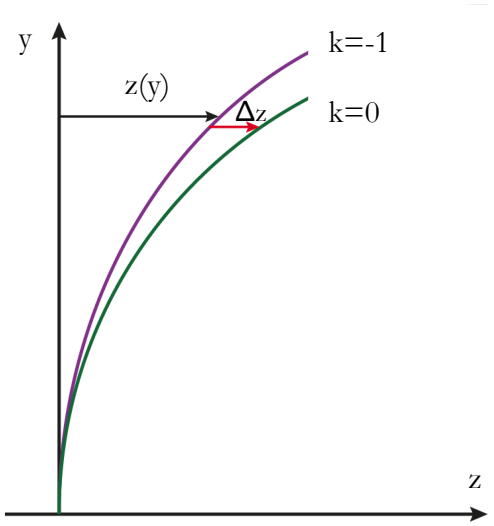

Figure 2.17: Surface sag of a spherical surface ($k = 0$) and parabolic surface ($\kappa = -1$). The variation in sag (Δz) between the sphere and parabola increases with surface height, which makes a parabolic surface suitable for correcting spherical aberration by modifying the intersection angles of the incident marginal rays with the surface.

plex surface descriptions, the deviation from the base shape is introduced by polynomial terms that are superimposed on the best fit sphere.

2.7 Zernike Polynomials

The aberration function for a circular aperture can be expanded using Zernike polynomials. These polynomials are orthonormal over the unit circle of constant weighting function. Defined in polar coordinates composed of a radial term $R(\rho)$ is dependent on azimuthal angle ϕ, Zernike polynomials are defined as:

$$Z_n^m(\rho,\phi) = \begin{cases} \sqrt{2n+1}R_n^m(\rho)\cos m\phi, & \text{for m} > 0 \\ \sqrt{2n+1}R_n^m(\rho)\sin m\phi, & \text{for m} < 0 \\ \sqrt{n+1}R_0^m(\rho), & \text{for m=0} \end{cases} \tag{2.55}$$

where the radial term can be calculated from:

$$R_n^m(\rho) = \sum_{s=0}^{(n-m)/2} \frac{(-1)^s(n-s)!}{s!\left[\frac{(n+m)}{2}-s\right]!\left[\frac{(n-m)}{2}-s\right]!} \cdot \rho^{n-2s} \tag{2.56}$$

Indices n and m are both integers and are both even or odd, fulfilling the condition $(n-m)$ always being even.

Zernike Fringe polynomials are a set of 37 low order terms based on the standard Zernike polynomials but are ordered following aberration theory. In the Zernike fringe notation, the angle ϕ is measured anti-clockwise from the local +x axis and the radial coordinate is the normalised dimensionless parameter $\rho = 1$ [87]. A conversion between the first fifteen standard and fringe terms are listed in Table 2.8.

Zernike polynomials are useful in optical design as they are orthogonal and complete polynomials [88]. The sag of a surface described by Zernike Fringe polynomials is a superposition of the terms described as:

$$z = \frac{cr^2}{1+\sqrt{1-(1+\kappa)c^2r^2}} + \sum_{i=1}^{8}\alpha_i r^{2i} + \sum_{i=1}^{N} A_i Z_i(\rho,\phi), \tag{2.57}$$

where c is the curvature of the surface, r is the radius where $r^2 = x^2 + y^2$, κ is the conic of revolution, the aspheric coefficient terms are denoted by α_i, A_i is the coefficient on the ith Zernike Fringe term.

Fringe $Z_i(\rho,\phi)$	Polynomial	Standard $Z_n^m(\rho,\phi)$
$\mathrm{Z}_1(\rho,\phi)$	1	$\mathrm{Z}_0^0(\rho,\phi)$
$\mathrm{Z}_2(\rho,\phi)$	$\rho\cos\phi$	$\mathrm{Z}_1^1(\rho,\phi)$
$\mathrm{Z}_3(\rho,\phi)$	$\rho\sin\phi$	$\mathrm{Z}_1^{-1}(\rho,\phi)$
$\mathrm{Z}_4(\rho,\phi)$	$2\rho^2-1$	$\mathrm{Z}_2^0(\rho,\phi)$
$\mathrm{Z}_5(\rho,\phi)$	$\rho^2\cos(2\phi)$	$\mathrm{Z}_2^2(\rho,\phi)$
$\mathrm{Z}_6(\rho,\phi)$	$\rho^2\sin(2\phi)$	$\mathrm{Z}_2^{-2}(\rho,\phi)$
$\mathrm{Z}_7(\rho,\phi)$	$(3\rho^3-2\rho)\cos\phi$	$\mathrm{Z}_3^1(\rho,\phi)$
$\mathrm{Z}_8(\rho,\phi)$	$(3\rho^3-2\rho)\sin\phi$	$\mathrm{Z}_3^{-1}(\rho,\phi)$
$\mathrm{Z}_9(\rho,\phi)$	$6\rho^2-6\rho^2+1$	$\mathrm{Z}_4^0(\rho,\phi)$
$\mathrm{Z}_{10}(\rho,\phi)$	$\rho^3\cos 3\phi$	$\mathrm{Z}_3^3(\rho,\phi)$
$\mathrm{Z}_{11}(\rho,\phi)$	$\rho^3\sin 3\phi$	$\mathrm{Z}_3^{-3}(\rho,\phi)$
$\mathrm{Z}_{12}(\rho,\phi)$	$(4\rho^4-3\rho^2)\cos 2\phi$	$\mathrm{Z}_4^2(\rho,\phi)$
$\mathrm{Z}_{13}(\rho,\phi)$	$(4\rho^4-3\rho^2)\sin 2\phi$	$\mathrm{Z}_4^{-2}(\rho,\phi)$
$\mathrm{Z}_{14}(\rho,\phi)$	$(10\rho^5-12\rho^3+3\rho)\cos\phi$	$\mathrm{Z}_5^1(\rho,\phi)$
$\mathrm{Z}_{15}(\rho,\phi)$	$(10\rho^5-12\rho^3+3\rho)\sin\phi$	$\mathrm{Z}_5^{-1}(\rho,\phi)$

Table 2.8: Conversion between Fringe and standard Zernike polynomial ordering.

Chapter 3

Dual-Wavelength Illumination for Extended Depth of Field

3.1 Introduction

Longitudinal chromatic aberration has been demonstrated to facilitate an extension in depth of field for fixed focus lenses. However, previous approaches are generally realised with the aid of post-processing and image reconstruction. A comprehensive review of these approaches are presented in Chapter 1. For current commercial devices computational algorithms can be increasingly demanding on the device battery. In this chapter a method of extending the depth of field using dual-wavelength illumination is presented. The aim of this study was to design a low-cost mobile phone lens for a front-facing camera with the purpose of iris recognition in user authentication. The iris is illuminated with two NIR LEDs and imaged with a singlet lens whose parameters are designed with a known longitudinal chromatic aberration. The singlet lens focuses both illumination wavelengths on to a fixed image plane from two separate finite distances in object space. The material featured in this chapter is a combined study of peer reviewed work from Optics Express [89] and the International Optical Design Conference [90].

An introduction to chromatic aberration and associated effects in imaging are discussed in Section 2.5. In most cases, longitudinal chromatic aberration is an undesirable effect due to the limitation of digital correction. However, LCA has positive uses in depth sensing and imaging in areas such as microscopy.

The theory presented in this chapter introduces the approach of how a plano-convex singlet can be used to generate the desired axial chromatic aberration to increase the range of distances in object space that are in focus on the im-

age plane. To finely tailor the induced chromatic aberration, a second lens can be added, whereby depending on the glass and power of the lens induced chromatic aberration can be tuned by extending or reducing the separation of the wavelengths.

Depth of Field Asymmetry in a Thin Lens

Establishing the asymmetry between the near and far depth of field regions about the object point with respect to the front vertex of a thin lens is central to this study. Chapter 1 introduced a widely used pair of equations, Eqs. (1.28) and (1.29) found in Smith and Laikin [7][12], to calculate the near and far regions for the depth of field of photographic lenses. The following derivation shows the foundation of the depth of field equations for a thin lens which are derived for the purpose of this study. The proof begins with the thin lens equation:

$$\frac{1}{l'} + \frac{1}{l} = \frac{1}{f}, \tag{3.1}$$

where l is the object position, l' is the image position and f is the focal distance of a thin lens. Rearranging Eq. (3.1) the reciprocal of the image distance can be isolated:

$$\frac{1}{l'} = \frac{1}{f} - \frac{1}{l}. \tag{3.2}$$

Equation 3.2 can be further simplified to isolate the expression for image distance:

$$l' = \frac{fl}{-f + l}. \tag{3.3}$$

Recalling depth of focus Δz for finite conjugate lenses discussed in Chapter 1 described by Eq. (1.22), is denoted as:

$$\Delta z = 1.22\lambda \frac{l'^2}{D^2} \times 2 \approx 2\lambda \frac{l'^2}{D^2}, \tag{3.4}$$

where the angular term for the Airy disk is multiplied by the image distance l' as for finite conjugate systems.

Conjugating the depth of field and depth of focus regions of the lens for finite object position, the thin lens equation can be modified such that the image position is represented by $l' \pm \Delta z$ and object region by $l \pm \Delta Z$:

$$\left(\frac{1}{l' + \Delta z}\right) + \left(\frac{1}{l - \Delta Z}\right) = \frac{1}{f}. \tag{3.5}$$

Rearranging Eq. (3.5) so that the object side parameters are separated from the image side parameters, the expression yields:

$$\left(\frac{1}{l' + \Delta z}\right) - \frac{1}{f} = -\left(\frac{1}{l - \Delta Z}\right). \tag{3.6}$$

Simplifying Eq. (3.6) similar to Eq. (3.3) gives:

$$l - \Delta Z = -\frac{f(l' + \Delta z)}{f - l' - \Delta z}. \tag{3.7}$$

Inserting the expression for the depth of focus from Eq. (3.4) into Eq. (3.7) an expression for the depth of field can be generated as:

$$\Delta Z^{\diamond} = l + \frac{f(l' + 2\lambda(l'^2/D^2))}{l' + 2\lambda(l'^2/D^2) - f}. \tag{3.8}$$

It is important to note the sign convention in the derivation for conjugating depth of focus to depth of field, Equation (3.8) can be rearranged to contain grouped variables:

$$\Delta Z^{\diamond} = l + \frac{f(1 + 2\lambda(l'/D^2))}{1 + 2\lambda(l'/D^2) - f/l'} \tag{3.9}$$

Considering that the image distance can be described by rearranging the thin lens equation in Eq. (3.3), a new variable can be defined as $\bar{Z}$:

$$\bar{Z} = 2\lambda\left(\frac{l^2}{D^2}\right), \tag{3.10}$$

where this expression is commonly known as the average depth of field. Substituting this relation into Eq. (3.9) yielding the thin lens expressions for the near and far depth of field are derived, Eqs. (3.11) and (3.12).

$$\Delta Z^{\diamond} = l - \frac{l^2 + f\bar{Z}}{(\bar{Z} + l)} = -\bar{Z}\frac{l + f}{l + \bar{Z}} \tag{3.11}$$

$$\Delta Z^* = -l - \frac{l^2 - f\bar{Z}}{(\bar{Z} - l)} = -\bar{Z}\frac{l - f}{l + \bar{Z}} \tag{3.12}$$

In this notation, the near region is denoted by $\Delta Z^\diamond$ and the far region by ΔZ^*, as shown in Fig. 3.1. They have to be derived separately as they do not share the same symmetric property as the depth of focus. Rather, $\Delta Z^* > \Delta Z^\diamond$, for $l \approx f$ then $\Delta Z^* \approx \Delta Z^\diamond$. However, for $l \gg f$, ΔZ^* departs from $\Delta Z^\diamond$.

Equation (3.10) describes the average value of the depth of field two regions;

$$\Delta Z = \frac{(\Delta Z^\diamond + \Delta Z^*)}{2} = \bar{Z} \tag{3.13}$$

In the case where the individual regions do not need to be known separately but rather the overall sum, then Eq. (3.10) can be used. It is to be noted that this relation holds for $\bar{Z} \leq l$, where l is much smaller than the hyperfocal distance [12].

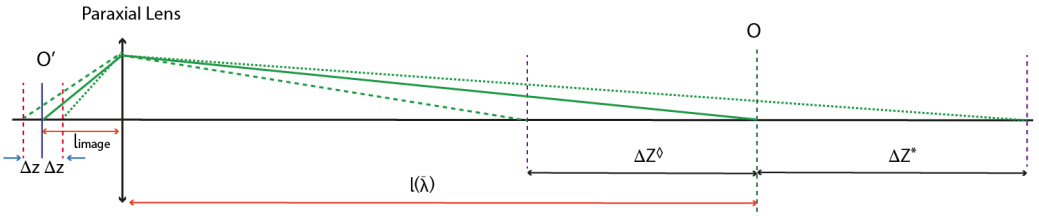

Figure 3.1: Effective depth of field for object position $l(\bar{\lambda})$, where $\bar{\lambda}$ is the average of the chosen illumination wavelengths. The lens is reversed for clarity when referencing the following reverse raytrace method.

3.2 Dual-wavelength illumination and Iris Imaging

In this section the method of extending depth of field relies on intrinsic LCA by means of a dual-wavelength illumination. Refocussing in this approach is carried

out by simply changing the position of the user relative to the front vertex of the lens, as shown in Fig. 3.2.

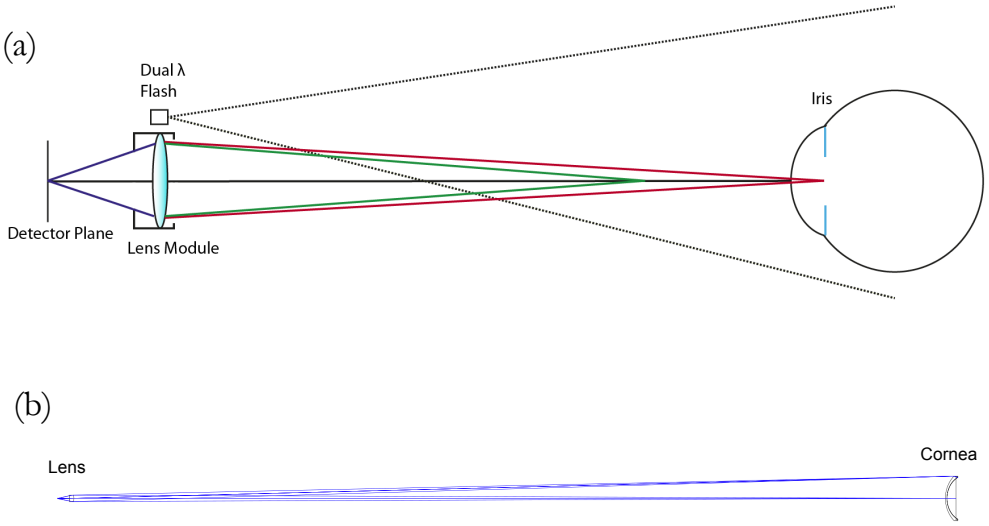

Figure 3.2: (a)EDOF concept: the dual-wavelength flash illuminates the iris which then reflects the NIR light. The lens is designed with a predefined amount of axial chromatic aberration such that the iris image remains in focus in one of the two colours shown in the top schematic which is not to scale. (b) Zemax raytrace to scale from the detector into object space showing the cornea and the iris.

The difference in this approach compared to previous methods of extending depth of field using LCA is that the sharp image is obtained in real time without computationally intensive algorithms.

Plastic commercial lenses can be mass-moulded for a few cents therefore using this method the lens can avoid requiring a refocusing system with voice coils. Mechanical refocusing can increase the cost of the camera module in a mobile phone by 10 %.

The illumination wavelengths were determined by the physical properties of the eye, shown graphically in Fig. 3.3. In the near infrared (NIR) the iris shows more structural detail, which is essential for iris recognition and authentication of the user [3]. Another advantage of illuminating in the NIR is the fact that in this spectral region there is a reduction in solar radiation, which helps to reduce the unwanted NIR background in daylight imaging (λ = 880 nm to 920 nm).

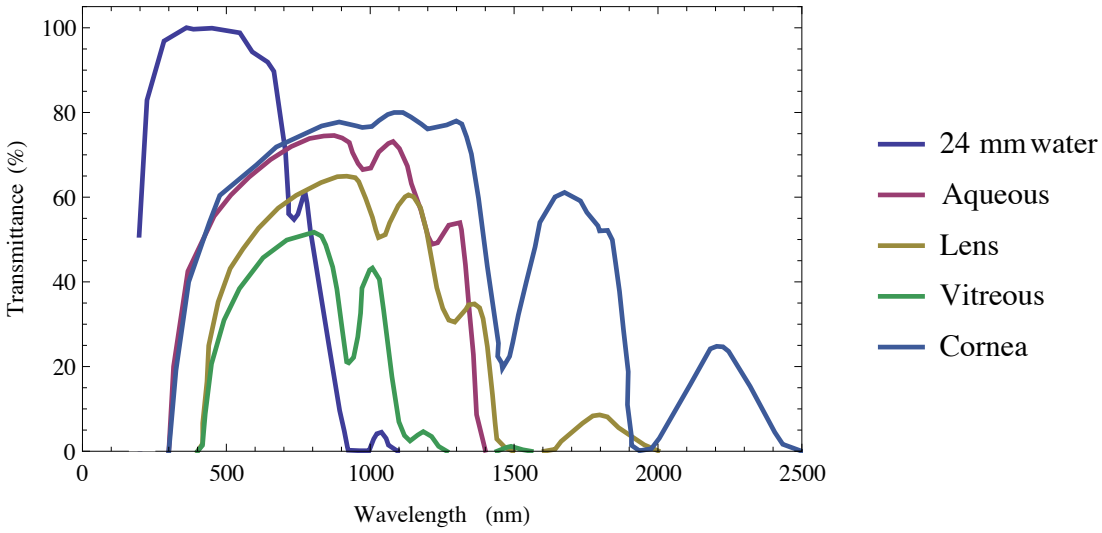

Figure 3.3: Percentage transmittance of the human eye, recreated with reference to [3].

The concept of EDOF using dual-wavelength illumination is presented by considering a plano-convex singlet. Iris illumination is formed by two commercial NIR LEDs, λ_1 and λ_2, of known bandwidth $\Delta\lambda$, where $\lambda_1 < \lambda_2$ and $\Delta\lambda \ll \lambda_2 - \lambda_1$.

In a conventional singlet lens, illuminating with a finite bandwidth introduces longitudinal chromatic aberration (LCA). One can exploit that feature with dual-wavelength illumination where consideration is given to the dispersive nature of the glass when optimising LCA of the lens. For a fixed image plane one could form either sharp image at λ_1 from a near distance and image at λ_2 from a far distance with both images being sharp at the conjoined plane between them located at $(\lambda_1 + \lambda_2)/2$ in object space. Determining the limits of this region is presented analytically and lens examples are discussed.

3.3 Analytical derivation of lens parameters

To describe the analytical method, paraxial raytracing using Welford's notation [76] is used to trace a marginal ray through the lens:

$$n'_j u'_j - n_j u_j = -h_j \phi_j \tag{3.14}$$

$$h_{j+1} = h_j + u'_j d'_j, \tag{3.15}$$

where u is marginal ray angle, h is ray height at the surface and ϕ is the optical power of the surface, described as $\phi_j = (n'_j - n_j)/R_j$ with R_j being the radius of curvature. The refractive index of the medium before and after the surface is denoted by n_j and n'_j, respectively.

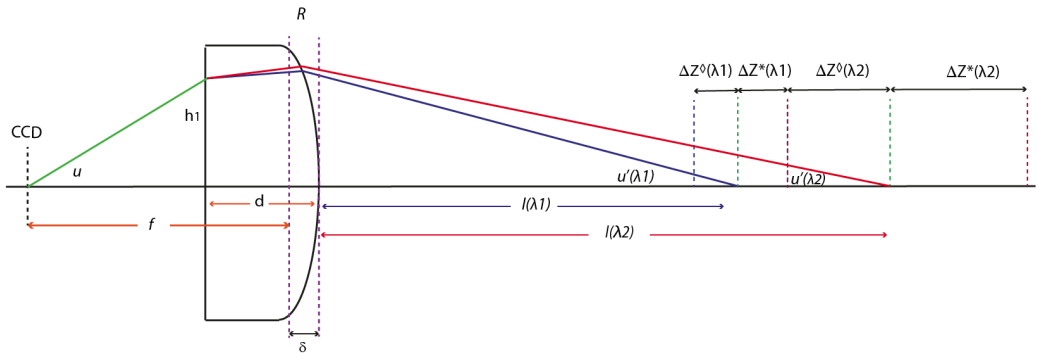

Figure 3.4: Reverse marginal ray trace through a plano-convex singlet showing LCA and the depth of field regions of $l(\lambda_1)$ and $l(\lambda_2)$.

Figure 3.4 shows the raytrace of a marginal ray through a plano-convex lens for wavelengths λ_1 and λ_2. Note that our approach employs reversed raytracing, that is the ray starts at the detector and propagates through the lens into object space. The principal planes of the singlet are drawn by dashed purple lines, where the front principal plane coincides with the vertex of the front surface of the lens. The second principal plane can be found by calculating the separation of the planes, δ, known as the interstitium [76].

Following the sign convention in optics, the radius of curvature for the posterior refracting surface of the singlet in air is negative ($R_j < 0$), the optical power of the surface is then written as:

$$\phi_j = \frac{(1 - n_j)}{R_j}. \tag{3.16}$$

In the case of a plano-convex singlet, Eq. (3.16) determines the overall optical power of the lens. Further consideration must be given to the use of multiple lenses and the ratio of the optical power for each surface with respect to the other yielding the overall desired induced LCA. This is discussed later in the chapter.

Reverse raytracing allows us to derive an expression for the final angles $u'(\lambda_1)$ and $u'(\lambda_2)$ for illumination wavelengths of λ_1 and λ_2, which correspond to different object positions due to LCA, see Fig. 3.4. The intrinsic amount of chromatic aberration in the singlet is denoted by the difference in chromatic object positions, $\Delta l = l(\lambda_2) - l(\lambda_1)$, where $l(\lambda_1)$ is chosen at the initial design stage.The choice of $l(\lambda_1)$ determines the radius of curvature R in the singlet for a chosen refractive index, $n(\lambda_1)$. The far object point is then a product of the lens material chosen, as the dispersion in the NIR is known. The choice of lens material is discussed in Section 3.4.

Using paraxial raytracing Eqs.(3.14), (3.15) the ray path can be derived through the plano-convex singlet lens for the two illumination wavelengths, λ_1 and λ_2 as:

$$u'(\lambda_1) = \frac{1}{f(\lambda_1)} + \frac{n(\lambda_1) - 1}{R} = -\frac{1}{l(\lambda_1)} \tag{3.17}$$

and

$$u'(\lambda_2) = \frac{1}{f(\lambda_2)} + \frac{n(\lambda_2) - 1}{R} = -\frac{1}{l(\lambda_2)} \tag{3.18}$$

The focal length f in Eqs. (3.17) and (3.18) is an unknown so to find its value for a thin lens, we note first that the separation of the principal planes δ is found as:

$$\delta(\lambda) = d - \frac{d}{n(\lambda)}, \tag{3.19}$$

where d is the central thickness of the lens. It should be noted that the above equation, Eq. (3.19), is an approximation since the quadratic term with respect to d has been omitted due to its dependency on optical power, which is an unknown in our approach. Using Eq. (3.19) and selecting the distance from the detector to the flat surface of the lens, which is the BFD in imaging mode, the focal length of the lens is found as:

$$f(\lambda) = BFD + d/n(\lambda), \tag{3.20}$$

which is illustrated in Fig. 3.4. For a chosen $l(\lambda_1)$, the radius of curvature is isolated from Eq. (3.17) to give:

$$R = f(\lambda_1)l(\lambda_1)(1 - n(\lambda_1))/(f(\lambda_1) + l(\lambda_1)) \tag{3.21}$$

For a selected lens material, whose dispersion properties are characteristic to that material, and the second illumination wavelength λ_2, one can calculate the refractive index as a function of wavelength $n(\lambda_2)$ and find the object position corresponding to that wavelength $l(\lambda_2)$ from Eqs. (3.21) and (3.18):

$$l(\lambda_2) = R/(1 - n(\lambda_2) - R/f(\lambda_1)) \tag{3.22}$$

The analytical method outlined above provides three lens parameters, namely, f, R and $l(\lambda_2)$ when λ_1, λ_2, lens material, $n(\lambda_1)$, $n(\lambda_2)$ as well as BFD and d are known from lens design specification. The depth of field associated with both object positions must overlap to ensure sufficient sharpness over the extended region $\Delta l + \Delta Z^{\diamond}(\lambda_2) + \Delta Z^{*}(\lambda_1)$ in object space, see Fig. 3.4.

To avoid excessive defocus in the mid region one requires to fulfil the condition for having no gap between $\Delta Z^{*}(\lambda_1)$ and $\Delta Z^{\diamond}(\lambda_2)$, that is:

$$\Delta Z^{\diamond}(\lambda_2) + \Delta Z^{*}(\lambda_1) \geq \Delta l. \tag{3.23}$$

Using the approximation for depth of field where both regions are of equal distance, $\Delta Z^{\diamond} = \Delta Z^{*} = \Delta Z$ and ΔZ is found from Eq. (3.10), assuming $\lambda = \lambda_1$, we can find the largest pupil diameter that satisfies this condition:

$$2\lambda_1 \left(\frac{l^2(\lambda_1)}{D^2} + \frac{l^2(\lambda_2)}{D^2} \right) \geq \Delta l, \tag{3.24}$$

which is equivalent to the expression $D^2 \leq 2\lambda_1[l^2(\lambda_1) + l^2(\lambda_2)]/\Delta l$. The condition for F-number is modified to be:

$$F\#^2 \geq \frac{f^2 \Delta l}{2\lambda_1[l^2(\lambda_1) + l^2(\lambda_2)]} \tag{3.25}$$

If the F-number from Eq. (3.25) is too large, i.e.the lens is too slow, it is possible to reduce λ_2 and therefore decrease Δl at the price of reducing the extension of EDOF for the lens. A trade-off exists between increasing Δl and attaining competitively low F-number, this is discussed further in the next section.

3.4 Optical system examples

The validity of the proposed analytical method is demonstrated with two examples using a plano-convex lens made of highly dispersing flint, N-SF5, and a commercially available moulded plastic, E48R.

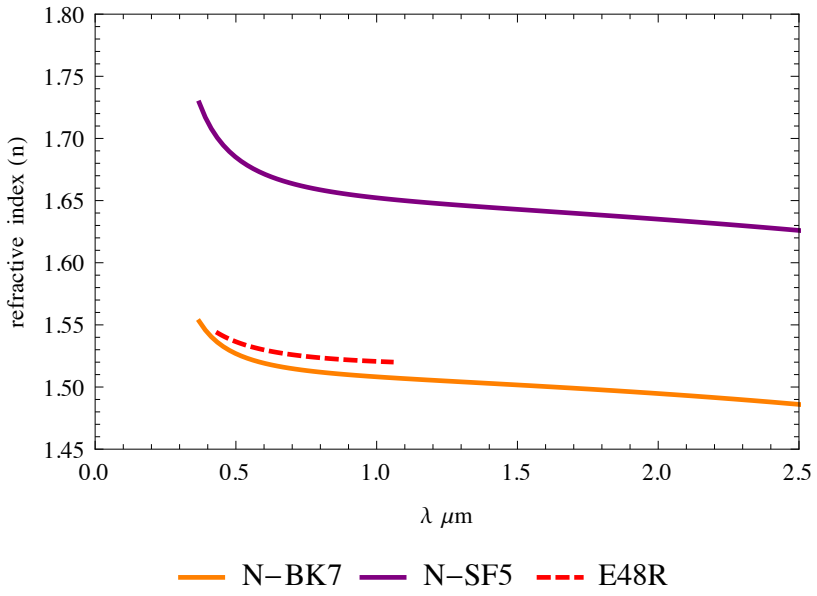

Figure 3.5: Dispersion plot for N-SF5, N-BK7 and E48R. Data provided from Schott [4] and Zeon [5].

For the chosen wavelengths to image the iris at $\lambda_1 = 780 \pm 15$ nm and $\lambda_2 = 870 \pm 20$ nm, according to the dispersion plot shown in Fig. 3.5 to maximise the longitudinal chromatic aberration in object space a highly dispersive glass should be chosen, thus leading to a larger depth of field. N-SF5 glass is a dense flint which is highly dispersive. The user defined input parameters are listed in Table 3.1.

Parameter	Abbe #	d (mm)	back focal length (BFL) (mm)	$l(\lambda_1)$ (mm)
Value	32.2	1.5	4	300 mm

Table 3.1: Input parameters for plano-convex singlet

Knowing the input parameters Eqs. (3.20) - (3.22) can be used to find the parameters for the lens as listed in Table 3.2.

Parameter	f	R	$l(\lambda_2)$	$\Delta l = l(\lambda_2) - l(\lambda_1)$
Value	4.90 mm	-3.182 mm	432.37 mm	132.37 mm

Table 3.2: Lens parameters for plano-convex singlet solved from Eqs. (3.20) - (3.22)

The condition for the F-number from Eq. (3.25) yields $F\# \geq 2.72$. For the smallest value $F\# = 2.72$, the corresponding diameter of the lens is $D = 1.8$ mm. The approximate formula predicts the depth of field as $\Delta l + 2(\lambda_1 l(\lambda_1)^2 + \lambda_2 l(\lambda_2)^2)/D^2 = 275$ mm. Note that at the near object distance $l(\lambda_1)$ the $F\#$ and working $F\#$ differ by approximately 1.5% and this discrepancy is to some extent compensated by the approximation of the principal planes made in Eq. (3.19). The exact value for the focal length verified in Zemax is $f = 4.825$ mm with corresponding F-number for an object at infinity is $F\# = 2.68$ and working F-number $F_w\#= 2.72$.

Equations (3.11) and (3.12) are used to determine the exact depth of field is $\Delta l + \Delta Z^{\diamond}(\lambda_1) + \Delta Z^{*}(\lambda_2) = 302$ mm. Figure 3.6 shows the exact depth of field where the near object point is taken as the origin for the horizontal axis. Depth of field at the far object point is 2.4 times longer than that of the near object point. Thus it is always more challenging to extend depth of field at near object distances.

Considering a single wave illumination at $\bar{\lambda} = (\lambda_1 + \lambda_2)/2$, which corresponds to the object distance $l(\bar{\lambda}) = 359.8$ mm, depth of field is $\Delta Z^{\diamond}(\bar{\lambda}) + \Delta Z^{*}(\bar{\lambda}) = 144.6$ mm. For this average wavelength ($\bar{\lambda}$), lens design with the dual wavelength illumination offers depth of field 2.09 times longer than that of single wavelength (λ_1) illumination design. Most importantly this extended depth of field allows

the user to exploit object distances in a closer proximity to the lens.

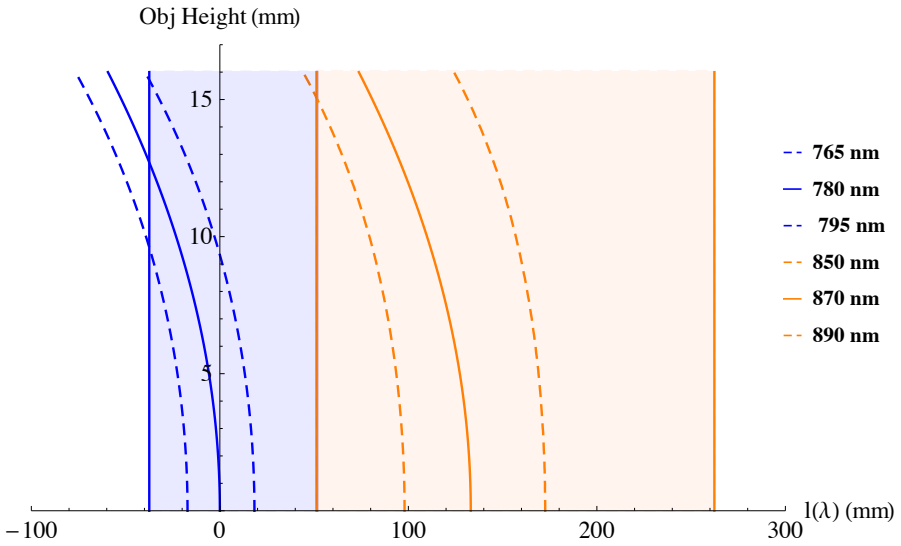

Figure 3.6: Plot in object space showing the depth of field for an N-SF5 singlet fulfilling the no-gap criterion for dual-wavelength enabled EDOF.

The singlet is assigned two aspheric surfaces, described by the following equation:

$$z = y^2/2R + Ay^4 + By^6 \tag{3.26}$$

The front surface of the lens has $A = 1.6736x10^{-3}$ mm^{-3}, $B = 2.877x10^{-4}$ mm^{-5} and conic constant $\kappa = -1$. The posterior surface has a conic constant $\kappa = -1$, $A = 2.7392x10^{-4}$ mm^{-3} and $B = 6.9758x10^{-4}$ mm^{-5}. Two aspherical surfaces allow to correct for spherical aberration and coma. The full field of view is limited by astigmatism to approximately 6 deg, while attaining diffraction-limited image quality. At the near object distance, $l(\lambda_1)$ the maximum object size is 32 mm for 6 deg flat field, which is sufficient to image the full iris of a single eye.

Figure 3.8 shows the aberration correction on the detector when the lens is in the imaging mode. The image quality is limited by astigmatism, but this does not compromise the centering of the eye on the detector as can be seen from Fig. 3.7, where we used Zemax raytracing software to simulate the impact of the lens aberrations on the image of the eye. Axial colour resulting from the finite bandwidths (30 and 40 nm) of the illumination sources is well within the depth of

focus and does not reduce image quality of the lens, see Fig. 3.6. For aberration analysis in Fig. 3.8 we assumed that the object is not a plane but a paraboloid of revolution with 1.63 mm radius of curvature at the vertex. This object surface indicates the optimum off-axis eye placement with respect to the lens when one needs to take into account the curvature of the object field as indicated by the solid lines in Fig 3.6. The iris is modelled as a flat surface. This allows one to widen the field of view to approximately 8° and also accounts for protruding facial features such as the eyebrow and nose.

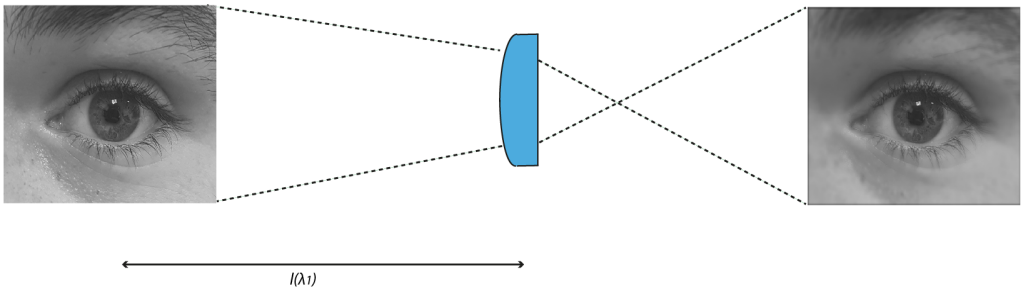

Figure 3.7: Iris imaging with an aspheric, plano-convex singlet lens described in Table 3.2. The features of the iris required for identification remain sharp, while the effect of astigmatism is noticeable outside the central field.

The spot diagrams for the two object distances $l(\lambda_1)$ and $l(\lambda_2)$ shown in Fig. 3.8 are plotted for on axis and approximately 4 deg off-axis field at six wavelengths, $\lambda_1 = 780 \pm 15$ nm and $\lambda_2 = 870 \pm 20$ nm. Block 1 shows six spot diagrams for near distance $l = l(\lambda_1)$ being in focus (λ_1 shown in blue), with the upper row for on axis and lower row for 3.7 deg off-axis field point. Block 2 corresponds to far object distance $l = l(\lambda_2)$ being in focus (λ_2 shown in green). Spherical aberration and coma are well balanced, whereas astigmatism and axial colour are present, as can be seen in the bar diagram for Seidel aberrations in Fig. 3.8.

An optical polymer can also be used as an example to explore the feasibility of extending depth of field. E48R from the *Zeon* catalogue has an Abbe number of 56.04, thus having a similar dispersive nature to a crown glass such as N-BK7. Table 3.3 lists lens parameters for both lens designs for comparison. Since the plastic material is less dispersive than N-SF5 glass, the plastic lens has a smaller $\Delta l = 61.74$ mm for the same illumination sources. As a result one can use an F-number as fast as 2.1.

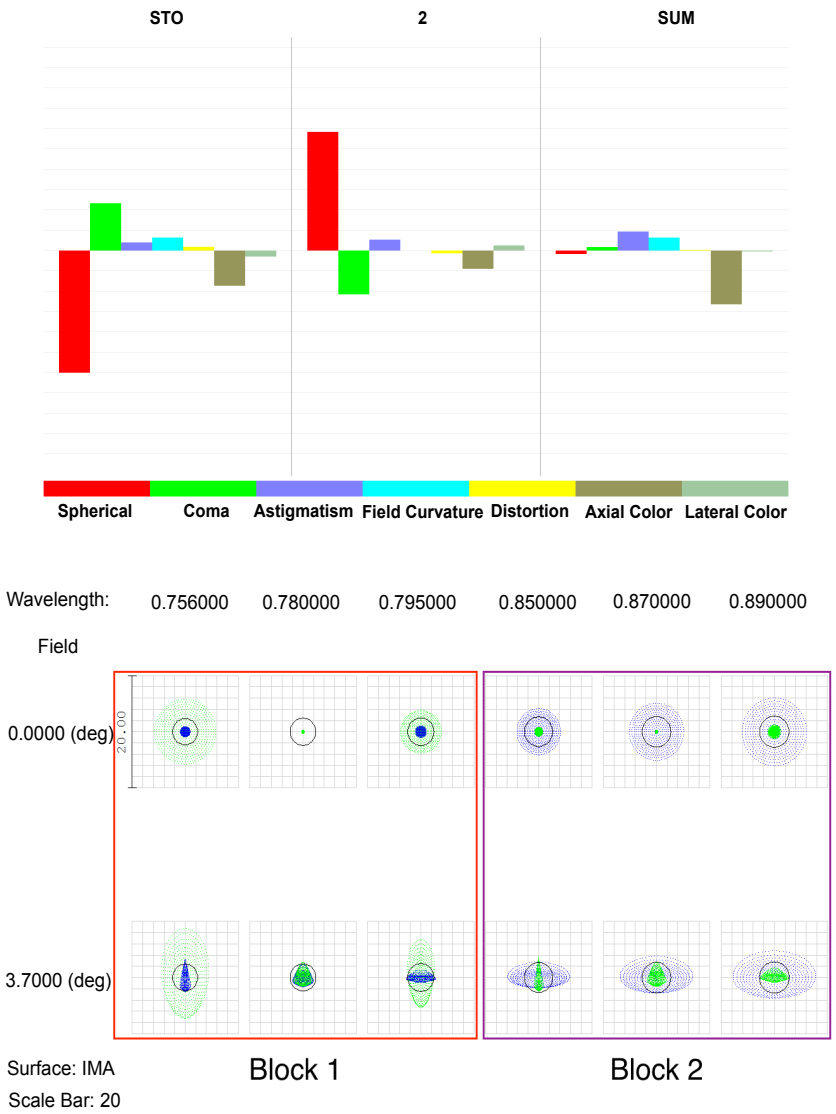

Figure 3.8: Seidel aberrations for the high dispersion N-SF5 singlet in image space (top). Maximum aberration scale is 0.00500 mm. The Block 1 and 2 of spot diagrams for the dual flash illumination on the image plane (bottom). The Airy disk is shown in black with a radius of 2.376 μm.

The illumination scheme is such that the image is obtained in a sequential manner. The sharper image can be selected based on sharpness criterion or the interpupilary distance if it can be found from the image. In practice, the method with the least power consumption will be chosen. For the mid position where both images are equally defocussed, we take the image with the longer distance

	$n(\lambda_1)$	$n(\lambda_2)$	f (mm)	R (mm)	$l(\lambda_2)$ (mm)	Δl (mm)	D (mm)	$F\#$	2 ω (deg)
N-SF5	1.6595	1.6560	4.90	-3.182	432.36	132.36	1.9	2.7	7.5°
E48R	1.52505	1.52348	4.98	-2.573	361.74	61.74	2.36	2.1	6°

Table 3.3: N-SF5 glass and E48R optical plastic aspheric singlets with parabolic object surface.

flash which ensures more flux and greater signal to noise ratio.

Visual representation of the data provided in Table 3.3. Figure 3.9 shows how the variation in object separation Δl changes with F-number to fulfil the no-gap criteria.

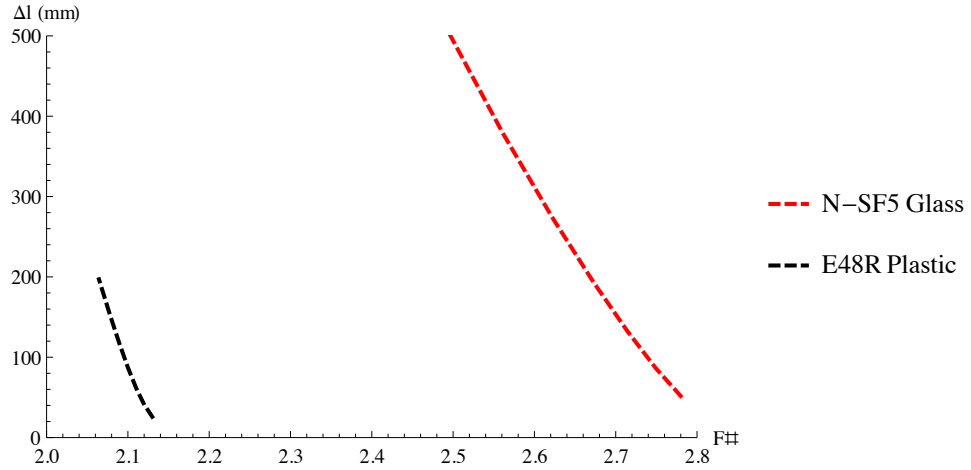

Figure 3.9: Δl dependencies of N-BK7 and N-SF5 singlet lenses on $F\#$.

The effect of near object position on the extended depth of field is shown in Fig. 3.10 for two plano-convex singlets made from N-SF5 glass and E48R plastic.

Cornea effects

The cornea was modelled in Zemax with data from previously published papers [91],[92]. Figure 3.11 shows the rms wavefront error in waves for $\lambda_1 \pm \Delta\lambda$. The

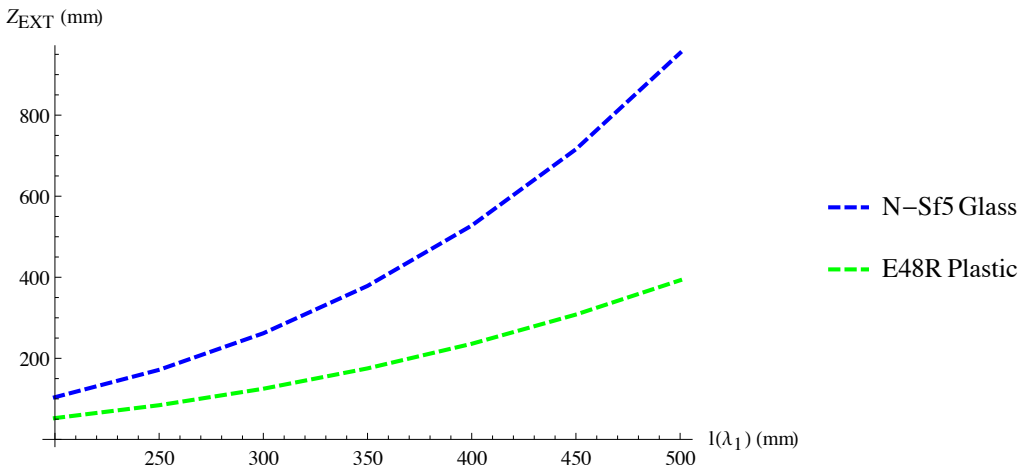

Figure 3.10: Extended depth of field as a function of object position $l(\lambda_1)$.

diffraction limit of the system when imaging through the cornea is 0.072 waves outlined by the Nijboer-Maréchal criterion [69], corresponding to 0.056 μm at λ_1 = 780 nm. A minimum of 2 cy/mm is required to image the fine details of the iris which corresponds to 150 cy/mm on the detector. This is outlined by the ISO requirements [93].

Figure 3.12 is the MTF of the lens and cornea where the modulus of the OTF at 150 cy/mm is 0.56. In our model, the presence of the cornea does not compromise image quality. A -9% distortion was induced by imaging through the cornea which can be easily corrected computationally as distortion does not blur the image. We also assume here that the detector has a pixel size of 1.19 μm to satisfy the Nyquist sampling criterion for the Airy disk radius of 2.38 μm.

The impact of lens shape factor and near object position

Optimising for a parabolic object surface allows one to have additional depth of field by decentering the eye and bringing it closer to the lens. That is by increasing the height in object space and following the curvature of the parabolic surface, see Fig. 3.6, one gains extra depth of field at the near object point. However, this parabolic surface lies between tangential and sagittal foci (for lens

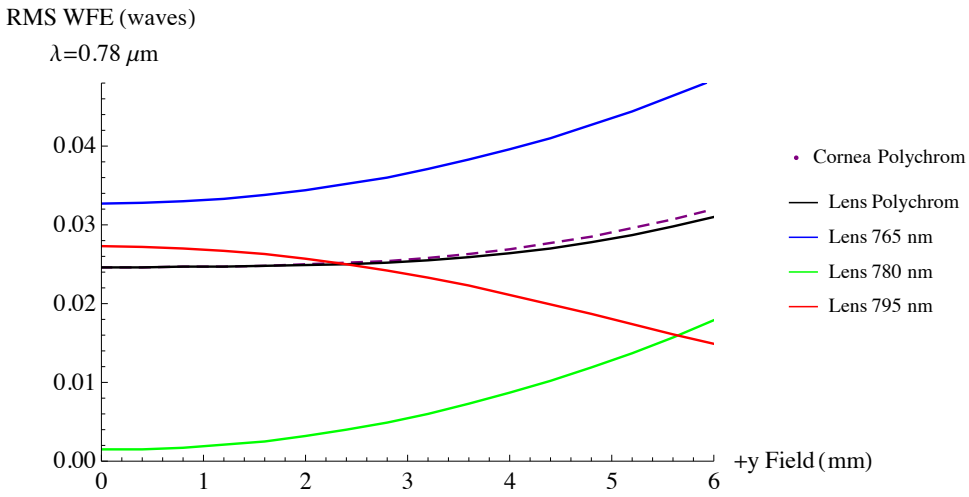

Figure 3.11: Rms wavefront error vs field for the singlet illuminated by $\lambda_1 \pm \Delta\lambda$. The effect of introducing the cornea on the rms wavefront error is seen by the dashed purple line.

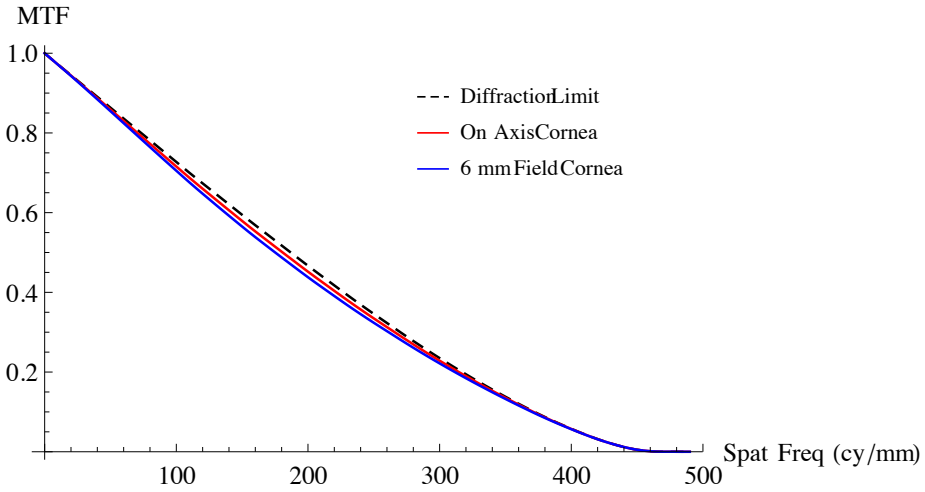

Figure 3.12: MTF for singlet lens and cornea.

working in reverse mode). Therefore, with increasing object height the possibility of imaging the iris as a whole becomes more challenging due to the astigmatism. The image quality of the iris imaged at 15 mm off-axis when the eye is positioned on the parabolic surface with a radius of 1.63 mm at 240 mm, shown in Fig. 3.14,

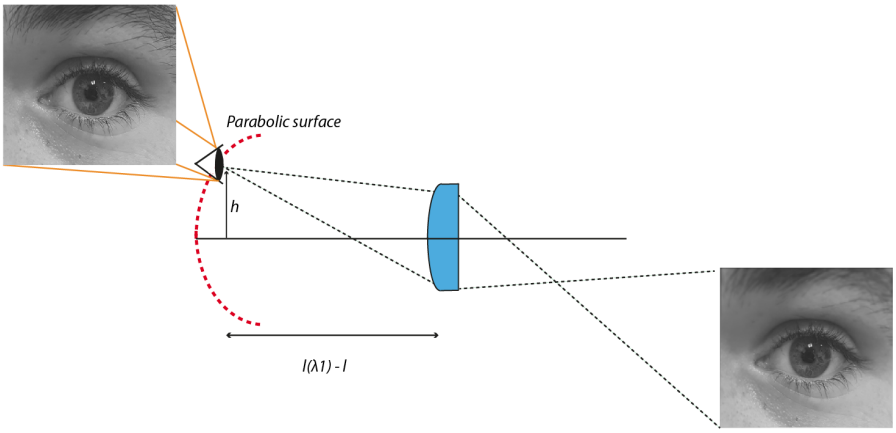

Figure 3.13: Iris imaging with an aspheric, plano-convex singlet lens centred at object height 15 mm positioned on the parabolic object surface at a distance 240 mm from the lens where l is the sag of the parabola at h=15 mm.

gaining additional 60 mm in depth of field at the near object point.

The plano-convex singlet presented in this study is chosen for the requirement of having F# $\leq$ 2.7. We have considered the use of other singlet lenses with different shape factor and studied its impact on our application, seen in Fig 3.15. A singlet with a back surface being concentric to the lens focus can offer a small reduction in Δl. For this lens design, the effect of each wavelength on object distance l can be calculated using the equation where the front radius R is solved as a function of λ_1 and then one could find $l(\lambda_2)$ as a function of λ_2 and R. Reversing the orientation of the plano-convex lens such that the planar surface is facing the object has the capability to increase Δl and field of view shown in table 3.4. The radius of curvature and far object point $l(\lambda_2)$ can be calculated

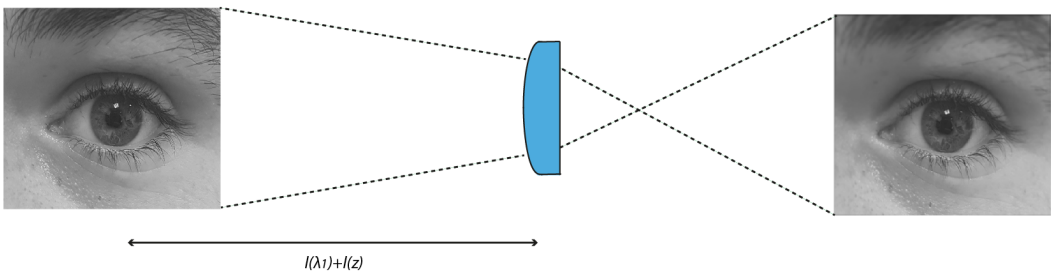

Figure 3.14: Iris imaging with a aspheric, plano-convex singlet lens centred at object height 15 mm positioned at $l(\lambda_1)$= 240 mm.

from $u'(\lambda) = 1/f(\lambda) + (n(\lambda) - 1)/R = -1/(l(\lambda) - d/n(\lambda))$ where R and $l(\lambda_2)$ are found as a function of λ_1 and λ_2 respectively.

$$\frac{n(\lambda)}{(BFD + d)} + \frac{(1 - n(\lambda))}{R} = \frac{-1}{l(\lambda)}, \tag{3.27}$$

where the front radius R is solved as a function of λ_1 and then one could find $l(\lambda_2)$ as a function of λ_2 and R. Reversing the orientation of the plano-convex lens, such that the planar surface is facing the object, has the capability to increase Δl and field of view shown in table 3.4. The radius of curvature and far object point $l(\lambda_2)$ can be calculated from:

$$u'(\lambda) = \frac{1}{f(\lambda)} + \frac{(n(\lambda) - 1)}{R} = \frac{-1}{(l(\lambda) - d/n(\lambda))} \tag{3.28}$$

where R and $l(\lambda_2)$ are found as a function of λ_1 and λ_2 respectively.

Freeing both radii in a singlet lens allows one to find an optimum lens shape for best aberration correction. In this case, the front object point is anchored at

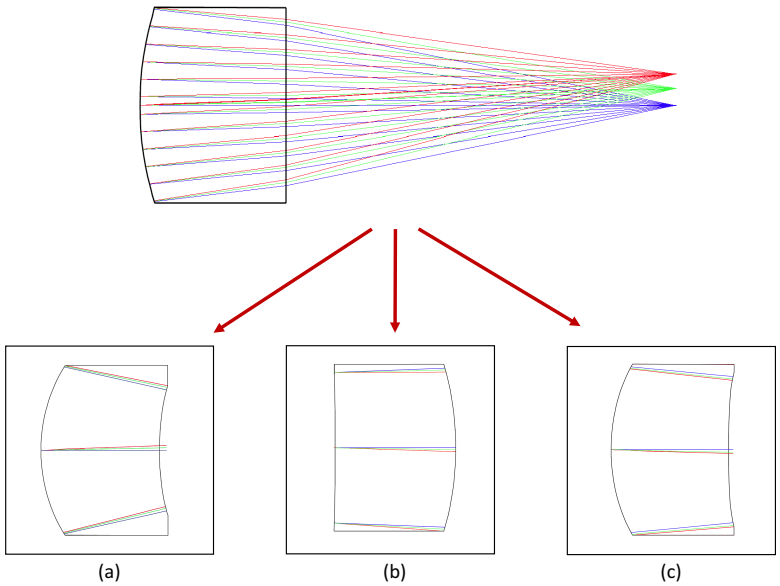

Figure 3.15: Singlet lenses in imaging mode: (a) concentric surface singlet, (b) reverse plano-convex singlet and (c) meniscus singlet.

Singlet	Concentric	Plano-Convex	Rev Plano-Convex	Meniscus
Δl	126.1 mm	132.37 mm	202.79 mm	230 mm
2ω CP	7.4 °	7.4°	12.8°	13°
2ω FP	6 °	6.5°	9.8°	10.3°
F #	2.6	2.7	3	3.1
SF	3.35	-1	1	-1.30

Table 3.4: Shape factor: Lens data for N-SF5 singlet where CP for the object surface as a parabola, FP is a flat object plane, SF is shape factor and 2ω is the full field of view

$l(\lambda_1)$=300 mm and the lens is optimised for parabolic object surface. The singlet lens geometry converges to a negative meniscus lens with an increased diffraction limited field to 13° and 10° for a planar object. The separation of object points, Δl, increases to approximately twice Δl of the initial plano-convex lens example. This extension in Δl occurs at the expense of increased F-number, as larger Δl

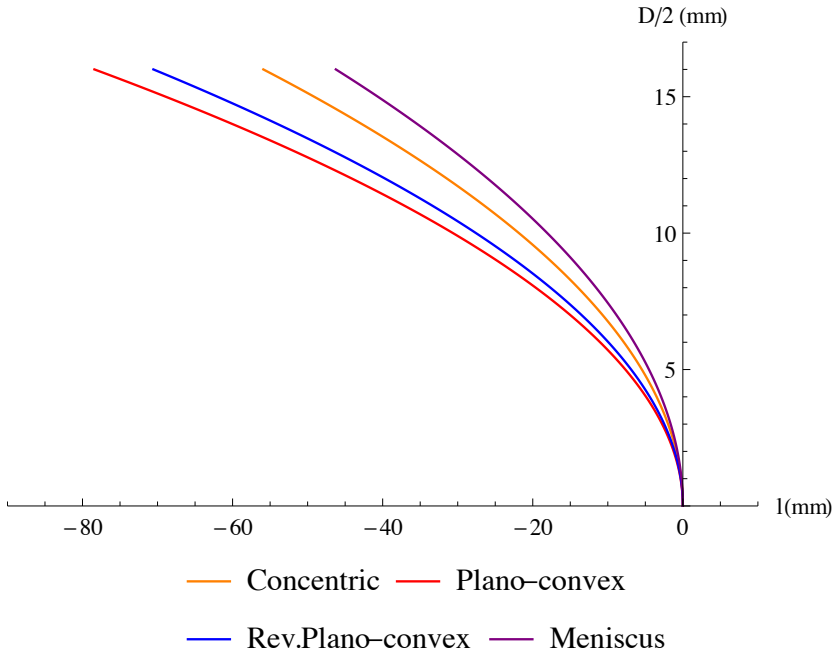

Figure 3.16: Optimised radius for Parabolic object surface for N-SF5 singlet lenses with different shape factor.

requires a slower lens. Table 3.4 includes a list of design parameters for different shape factors of a singlet made from N-SF5 having different shape factors:

$$SF = \frac{R_2 + R_1}{R_2 - R_1}, \tag{3.29}$$

where R_n is the radius of curvature of the n^{th} surface. Each singlet lens requires an optimised parabolic object surface with a specific radius shown in Fig. 3.16

A singlet lens with aspherical surfaces has the degrees of freedom to correct spherical aberration and coma. However, the residual astigmatism can be minimised by optimising the parabolic object surface. Four variations on the singlet is presented; plano-convex, reversed plano-convex, meniscus and concentric. The concentric lens is orientated such that the back surface is concentric to the lens focus.

A visual representation of the variation in parabolic object surface with shape factor is then shown in Fig. 3.16. The surfaces correspond to Table 3.4.

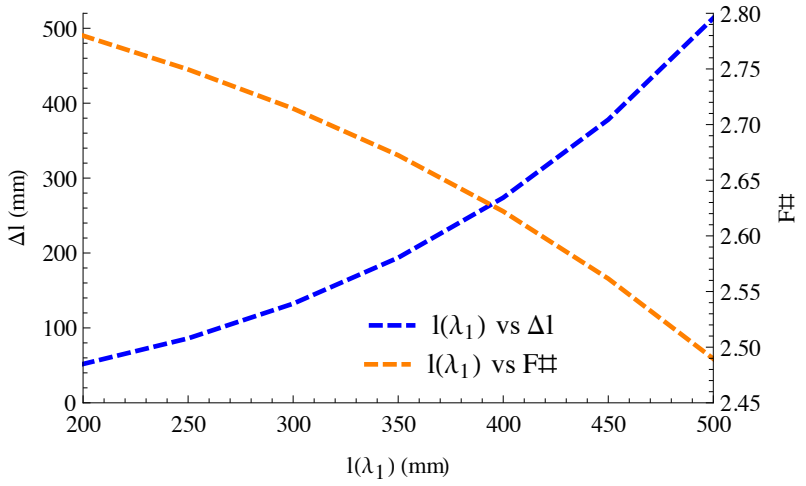

Figure 3.17: Changes to F-number and Δl as the distance of the near object point is varied.

Special constraints must be introduced when applying this methodology to

the visible spectrum. LCA in the visible region must be controlled such that Δl does not exceed a certain value to avoid a slow lens associated with a larger Δl. The separation of LED central wavelength of the two sources can be reduced to 50 nm in the mid region (yellow) of the visible spectrum where slope of refractive index versus wavelength is not as steep compared to shorter wavelengths (blue region), thus one could achieve a usable F-number suitable for a mobile phone camera. Additionally, materials of high Abbe number can be chosen inducing low dispersion that brings Δl to similar values as we presented for the NIR region. Alternatively, one could consider introducing two elements with a partial compensation of axial chromatic aberration to gain better control of chromatic aberration in the visible.

It is interesting to note that one could also vary the near object distance to control Δl, however as one can see from Fig. 3.17 bringing near point closer to the lens reduces Δl and depth of field and at the same time increases F-number which again shows the challenge of extending the depth of field at regions closest to the lens.

3.5 Conclusion

An extension in depth of field has been analytically derived and shown for a singlet lens. The method presented in this chapter focuses on a singlet lens which uses dual-wavelength illumination to extend the depth of field. This study includes the feasibility of both low and high dispersion materials and their effect in achieving an extended depth of field. The performance of this method also includes a model of the cornea and the possibility of induced aberrations by reflecting from the cornea. This analysis shows that -9% distortion is introduced and does not deteriorate the MTF.

Chapter 4

Two Iris Imaging over an Extended Depth of Field

4.1 Introduction

A single iris imaged in Chapter 3 is feasible due to the small FOV needed. A singlet lens was shown to have enough degrees of freedom to carry out such a task. A larger FOV is required to capture two irises. An increased FOV gives rise to higher amplitudes of field dependent aberrations. Increasing the degrees of freedom in the lens, that is introducing a mixture of surfaces and lens materials, these aberrations can be minimised on the image plane.

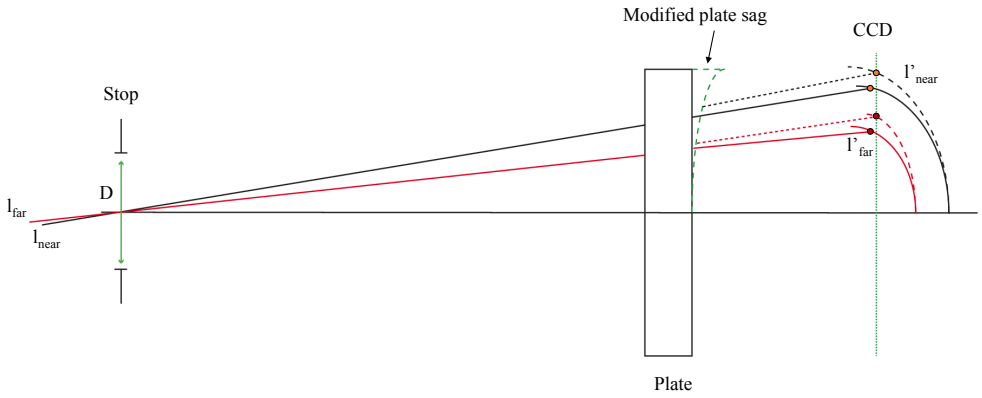

Figure 4.1: Schematic for off axis behaviour of image surfaces. The continuous curved line represents the image surface produced by a planar plate while the dashed line corresponds to the shift in the displacement of the image point due to a variation in the plate thickness as a function of height.

A lens-plate design combination for imaging two irises over an extended depth

of field is introduced in this chapter. The novelty of the design is central to a variable thickness planar element adjacent to the CCD plane, a simplified illustration is shown in Fig. 4.1. The preceding elements with non-zero optical power are responsible for aberration correction. These elements are also optimised for specific regions in the field corresponding to iris locations separated by a fixed interpupilary distance (IPD). In the case where the lens has no residual aberrations present, one can consider that a variation in object position will affect the image position in a non-linear profile due to the Petzval curvature in the field. The planar element is responsible for displacing the image points by varying the thickness with respect to the principal ray of each field angle by a well known relation for thickness variation of a planar plate determining the shift in image position along the optical axis. Varying the thickness for a range of principal ray angles corresponding to the iris movement in object space, therefore creates a continuous region in which the irises can move along the optical axis with respect to the lens with a sagittal field containing the irises. The work presented in this chapter is an extended study based on a proceedings paper presented at SPIE Optical Systems Design [94].

4.2 Iris positioning for plate design

In Chapter 3 it was shown that multiple individual regions of focus from discrete wavelengths can be summed together to extend the depth of field by using the lens parameters [89]. Such intermediate calculations can be avoided by generating a continuous depth of field from a single illumination source. In this chapter a range of elements are presented which have the capability of extending depth of field up to 3 times compared to a conventional lens conjugate to the same object. The EDOF element is positioned adjacent to the detector plane after the main refracting elements of the lens. Two spatially varying object configurations are presented, images that horizontally vary across the detector and images that vary both vertically and horizontally with respect to object position. Figure 4.2 illustrates the two geometries used in designing the elements by illustrating the image position on the detector plane. The first orientation (shown in red) is based

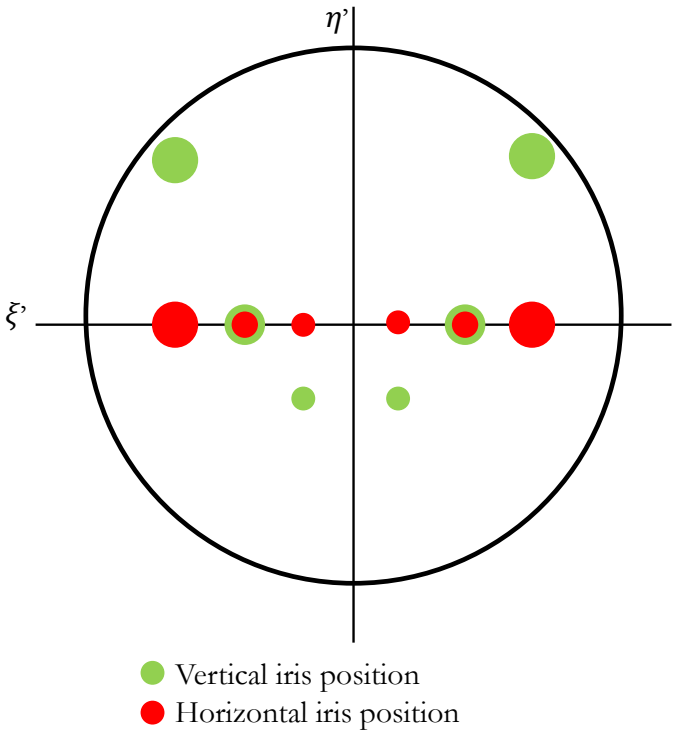

Figure 4.2: Iris image positions on the CCD plane. The red circles indicate the movement of the head along the optical axis, where the the separation of iris images is dependent on the principal ray angle. The green circles correspond to the head repositioning laterally with respect to central object position in order to further separate the images formed on the sensor.

on the iris movement parallel to the optical axis, fundamentally relying on the variation in principal ray angle to separate the images on the CCD. The second (shown in green) introduces a small lateral variation in iris position from the optical axis (±y) to utilise more of the detector for EDOF. As the irises shift axially, the PR is modified to a skew ray whose incident angle varies with respect to iris distance from the lens. The circle shown in red with green edge is the lens conjugate position centred at y=0 and x=$\pm D_p/2$. PR incident angle on the image plane ranges from $(-\xi, +\eta)$, $(0, \eta)$, $(+\xi, -\eta)$ as the irises move from the nearest to furthest resolvable distance from the lens $l_n \rightarrow l_f$, for simplicity notation here follows Fig. 4.4.

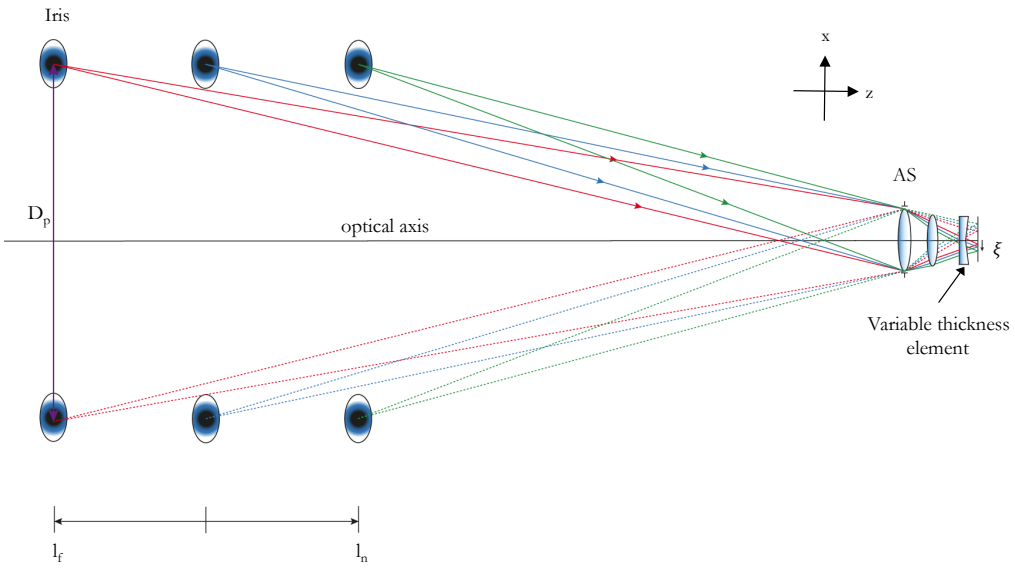

Figure 4.3: X-Z coordinate system illustration for imaging two irises over an extended depth of field.

4.3 EDOF plate for radially varying iris images

The first object orientation is based on the simple geometry that, for a fixed interpupillary distance, an axial variation in object distance yields a change in the PR angle illustrated in Fig 4.3.

According to ideal imaging, a point object positioned at O in the field i.e. has non-zero x coordinate, at $+x$ from the optical axis forms a perfect point image O' at $-x'$ in image space. However, departing from the paraxial region aberrations influence the performance of the optical system. Consider an object positioned at an object distance l with a fixed horizontal position $+x$ from the optical axis in object space, its image is formed at $-x'$ from the axis on the image plane at l'. Intuitively, an object positioned at $l \pm \Delta l$ at that same fixed height will form an image at $l' \pm \Delta l'$ with at a lateral position of $x' \pm \Delta x'$. For a range of discrete object distances $l_1, l_2 ... l_n$ with a fixed height $+x$ from the optical axis, the field angle θ varies with respect to the object position, see Fig. 4.3. This change in

PR angle produces a lateral shift (along x') in image position with respect to the object. For two-iris imaging applications, the fixed horizontal position is half the IPD at $\pm x$. The variation in object position Δl will also cause a longitudinal displacement of the image whose profile is dependent upon the lens. The presence of residual field curvature in the lens can influence the longitudinal shift in image position. In this application, the distribution of images laterally is advantageous for the correction of the longitudinal image displacements as a radial variation in thickness along an element adjacent to the sensor can individually compensate this error. The lateral displacement also allows for each iris position to be imaged at separate discrete positions on the CCD.

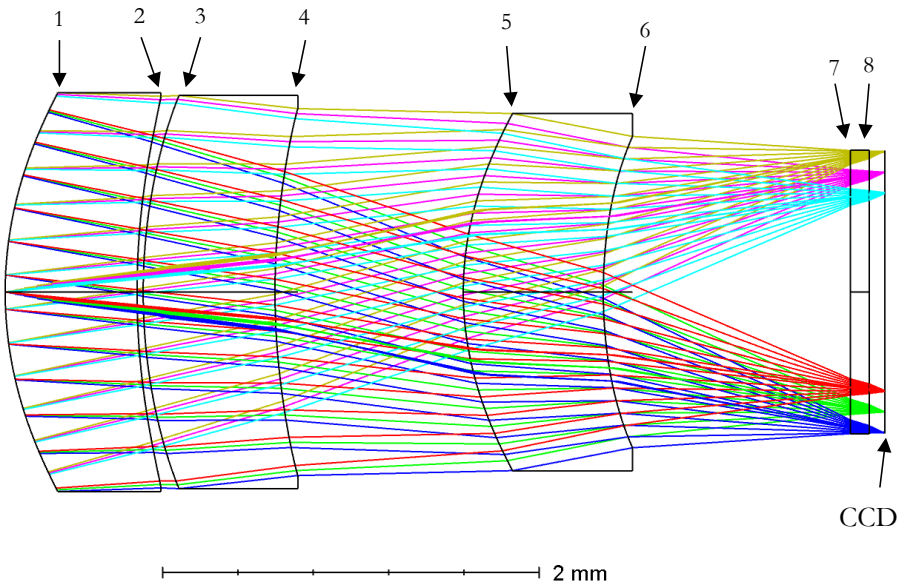

Figure 4.4: Zemax layout for the lens and PP for the prescription in Table 4.1 for objects positioned at ± 41 mm, ± 35 mm and ± 29 mm in x from the optical axis at maximum image height on the CCD.

4.3.1 Lens for axially varying iris images

The lens presented in this section was designed for the purpose of this study. Once optimally designed, the lens for imaging the axial iris movement is presented at the beginning of the study as the lens will remain fixed while the plate designs

are modified. The lens data is provided in Table 4.1. Surfaces 7 and 8 are shown as a parallel plate for the initial design with a fixed central thickness such that any modifications to the plate will retain the overall track length. This study includes a comparison between profile modifications to surface 8, labelled in Fig. 4.4. It is important to note that once optimised, the lens parameters and aspheric terms for surfaces 1 to 6 are fixed for the study. Therefore, the comparative study exists between the ability of each plate surface to improve the spatial frequency response for the designated iris region over the EDOF region.

Design simplicity of the lens and material choice is due to the nature of the application. The lens is aimed at a high yield market and so the lenses are designed in plastic which is commonly moulded for consumer optics. For iris imaging, the fine details of the iris are captured in the NIR and so illumination is provided by a commercially available narrowband NIR light emitting diode (LED) with wavelength $\lambda = 940 \pm 20nm$.

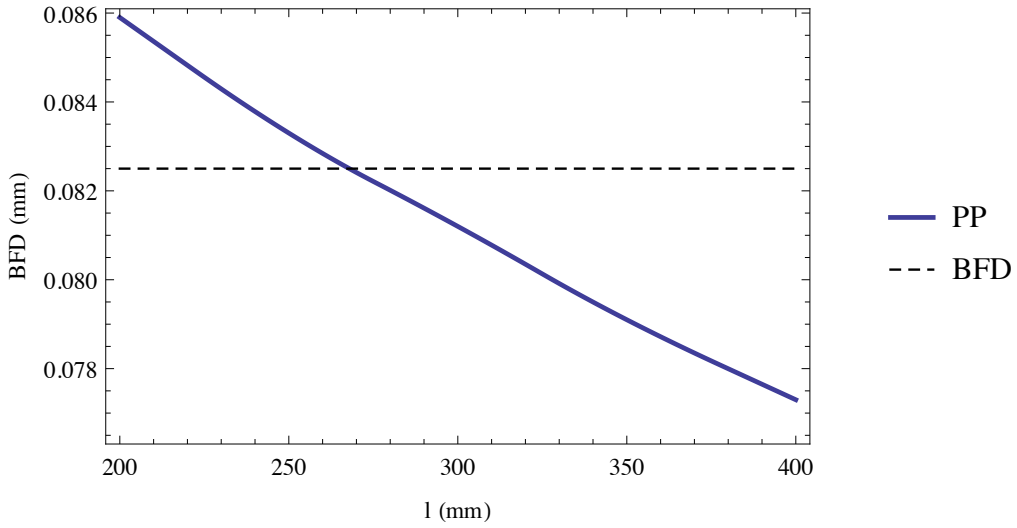

Figure 4.5: Variation in image position with respect to object position for the lens with parallel plate listed in Table 4.1.

The track length of the lens is 4.67 mm, with an entrance pupil diameter of 2.0 mm and focal length of 3.59 mm, fitting within the current design space for smartphone cameras. The stop is located at the front surface as is typical for fast systems such as smartphone lenses to control the principal ray angle. The

average working F-number for this lens is $F\#_w = 1.81$. The average F-number is quoted as the working F-number is dependent on object position, which varies in this application. The discrepancy in $F\#_w \leq 0.014$ for the largest separation of object positions $|l_f - l_n| = 200$ to 400 mm. The back focal distance for the lens is chosen conjugate based on the image position such that the plate will not collide with the CCD plane. In this study the conjugate distance is chosen to be 260 mm, as the BFD intersects the image plane at this point shown in Fig. 4.5.

Surf	Rad (mm)	Thick (mm)	Material	Conic
1	2.0233	0.7000	PMMA	-1
2	3.9039	0.0327	Air	-1
3	3.0250	0.7000	E48R	-1
4	3.7860	1.0000	Air	-1
5	1.6975	0.7436	E48R	-1
6	2.6900	1.3122	Air	-1
7	Infinity	0.1000	E48R	0
8	Infinity	0.0825	Air	0

Table 4.1: Lens data for lens and parallel plate with horizontal iris positioning.

Surf	A (mm^{-3})	B (mm^{-5})	C (mm^{-7})	D (mm^{-9})
1	5.4171×10^{-3}	-4.094×10^{-4}	-1.207×10^{-3}	-1.212×10^{-3}
2	-7.871×10^{-4}	-1.038×10^{-3}	-8.575×10^{-4}	-3.139×10^{-3}
3	3.0920×10^{-3}	2.4618×10^{-3}	7.6209×10^{-4}	1.4719×10^{-3}
4	-0.0106	-5.785×10^{-3}	7.7281×10^{-3}	5.1188×10^{-3}
5	9.0604×10^{-3}	-0.0127	-8.518×10^{-3}	7.1745×10^{-3}
6	0.0702	-0.0255	9.8339×10^{-3}	8.591×10^{-3}
7	0	0	0	0
8	0	0	0	0

Table 4.2: Aspheric coefficients for lens presented in Table 4.1 with horizontal iris positioning 4^{th}, 6^{th}, 8^{th} and 10^{th}.

Irises are a good example of objects positioned off-axis at a fixed position. This position is known as the IPD denoted by D_p ranges from 58-70 mm for the average

person. We define the separation of the fixed object horizontally positioned from the axis origin as half the interpupillary distance $D_p/2 = \pm x = 35 \pm 6$ mm. The allowable image height in our design $\pm y$ is ± 5 mm enclosing the iris and accounting for the eyelid obstruction of the upper and lower segments of the iris.

A good starting design is critical to the performance of any imaging system. The lens was designed for optimal aberration correction. The lens with the parallel plate is optimised for off-axis points only between ± 29 to 41 mm along the sagittal plane, where the irises are located with respect to the optical axis. The selected field containing the irises are weighted during optimisation, where the central field is neglected as it is not useful in this application. The central field can be sacrificed to boost the MTF of the more peripheral regions that contain biometric information.

The lens parameters are provided in Table 4.1, and aspheric coefficients in Table 4.2. The simplicity of the lens design and material choice is due to the nature of the application. The lens is aimed at a high yield market and so the lenses are designed in plastic which is commonly moulded for consumer optics. For iris imaging, the fine details of the iris are captured in the near infrared therefore illumination is provided by a commercially available narrowband NIR LED with wavelength $\lambda = 940 \pm 20nm$. As a consequence of imaging in the NIR, the choice of plastics is limited to those that provide refractive index vs. wavelength data for the NIR spectrum.

The first element in the lens is an air-spaced doublet, where two plastics are chosen to be achromatic with the lens, shown in Fig. 4.4, for a chosen light source. The lens has -0.15 μm of lateral colour that comfortably lies inside the Airy disk. The Airy radius has a value of $2.09\mu m$ at the largest PR angle. The lens and plate combination has a maximum distortion of 0.4% at $l = 200$ mm in the area of interest which encloses the irises, decreasing with an increasing value of l.

As the lens is conjugate to a fixed position in object space, for $l = 260$ mm the average depth of field would be described by Eq.(1.26) for central wavelength $\lambda = 0.94$ μm and have a value of $\Delta Z = 63.54$ mm. All extensions in EDOF for horizontally varying iris images will we compared to this calculation throughout our study.

For this lens, inclusive with the parallel plate, the back focal position varies

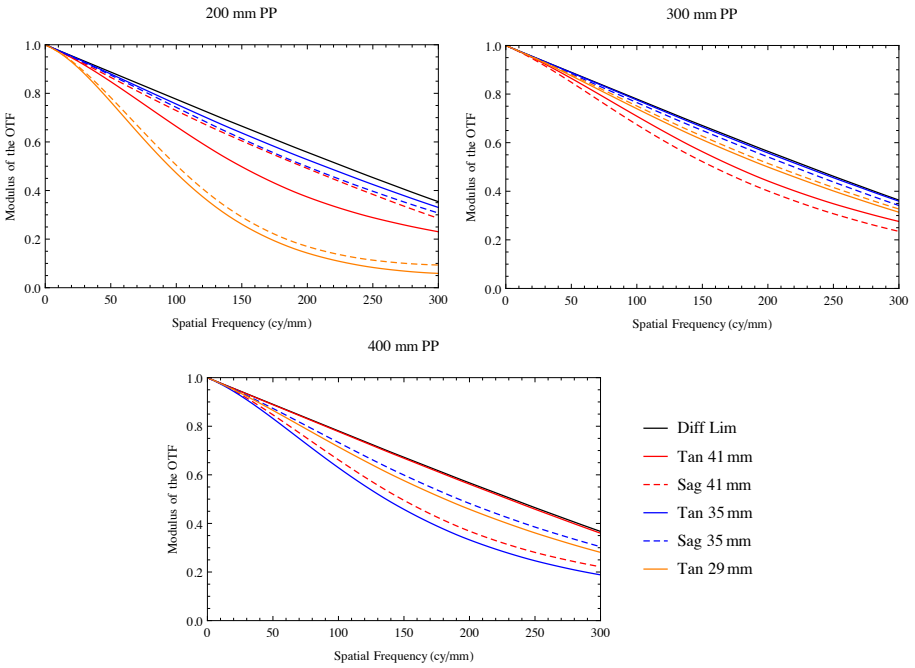

Figure 4.6: MTF for object positions with PP plate for discrete object positions of 200, 300 and 400 mm.

with object position. The off-axis object-image relation is shown in Figure 4.25. The discrepancy in back focal position is $\Delta l' = 0.0083$ mm. This variation in back focal distance can be compensated by inserting a plate which has a variation in thickness as a function of plate height.

In the following sections an EDOF plate is introduced which does not have optical power but instead, a variation in thickness is introduced through a non-planar surface described by high order polynomials. These polynomial surfaces create a continuous depth of field region by displacing the discrete image positions with respect to the ray height.

Table 4.3 lists the spatial frequency requirements for imaging the iris in image space at 2 lp/mm. The optical power of the lens remains constant, therefore the spatial frequency requirements are listed for $200 \leq l \leq 400$ mm as follows.

The MTF plots in Fig. 4.6 show the lens performance for three selected object positions, 200, 300 and 400 mm. From Table 4.3 it can be interpreted that the lens has the capability for sufficiently imaging the irises at 2 lp/mm at 200 to 300

Object (mm)	Spatial Frequency (lp/mm)
200	110
300	165
400	221

Table 4.3: Image space spatial frequency requirements for 2 lp/mm in object space imaged with the lens presented in Table 4.1.

mm but does not satisfy the spatial frequency requirement at 400 mm.

4.3.2 High order polynomial plate (AP)

The first iteration of minimising the variation in BFD is assigning an aspheric polynomial consisting of only odd terms to surface 8. Throughout the study this plate will have the acronym AP. The first linear term and the second quadratic term are neglected as shaping the slope of the central region is not required when the rays do not propagate through this area. It is interesting to note that the non-continuous apex that arises from the use of the first linear term does not generate a faithful representation of the plate performance as the parabasal ray cannot be used as a reference ray. The change in slope desired to generate the thickness variation for compensating image displacement with respect to iris position is provided towards the peripheral region of the plate. The sag of an aspheric surface is described by Eq. 2.19. As the plate has no optical power the first term vanishes and leaves the sum of the remaining terms to determine the shape the surface.

The depth of focus is defined with respect to the optical axis. Imaging off-axis objects introduces a small deviation in the principal ray angle, where the depth of focus is defined with respect to. However, this angle is small so we can apply the small angle approximation and treat the depth of focus parallel to the image surface.

For the aspheric terms described by Eq. 2.19 the corresponding values are listed in Table 4.4. The sag of the aspheric surface is shown in Fig. 4.7, both cross-sectional profile (left) and a full surface sag profile (right). The aspheric

Term	Value		Term	Value
y^3	3.0725 $\times 10^{-4}$ mm^{-2}		y^{11}	3.96516$\times 10^{-10}$ mm^{-10}
y^5	-3.525$\times 10^{-5}$ mm^{-4}		y^{13}	-2.034$\times 10^{-12}$ mm^{-12}
y^7	1.5388$\times 10^{-6}$ mm^{-6}		y^{15}	6.1903$\times 10^{-16}$ mm^{-14}
y^9	-3.406$\times 10^{-8}$ mm^{-8}		y^{17}	2.1191$\times 10^{-17}$ mm^{-16}

Table 4.4: Aspheric coefficients used in the high order EDOF AP.

element is rotationally symmetric therefore the radial angle at which the cross section is taken is irrelevant. The plate creates an annular region imaging the field which allocates equal weighing in optimisation for x and y, although containing no biometric information along the vertical plane.The P-V difference in the optimised aspheric surface sag is 0.0251 mm for the region involved in iris imaging.

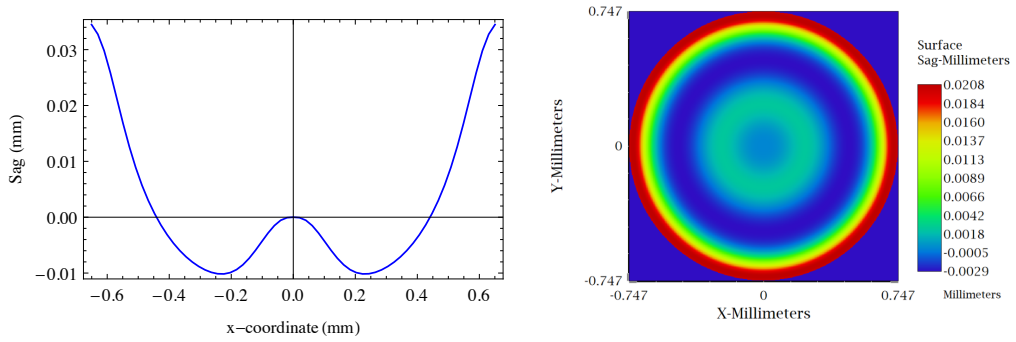

Figure 4.7: Cross section of the sag and surface sag profile for the AP.

The lens and aspheric plate design has a maximum of 1.27% distortion in the region where the irises are located in the field. The MTF response are plotted in Fig. 4.8 for discrete object positions of 200, 300 and 400 mm in the presence of the aspheric plate. Analysing the improvement over the usable EDOF shows a degradation in image quality for images formed at small field angles seen in Fig. 4.9. This is noticable for both original PP and AP MTF plots for 400 mm in Fig. 4.6 and Fig 4.8. This degradation is due to the nature of the polynomial when attempting to compensate the peripheral images.

The plate is optimised for an object range of 200 mm to 400 mm. From Fig.

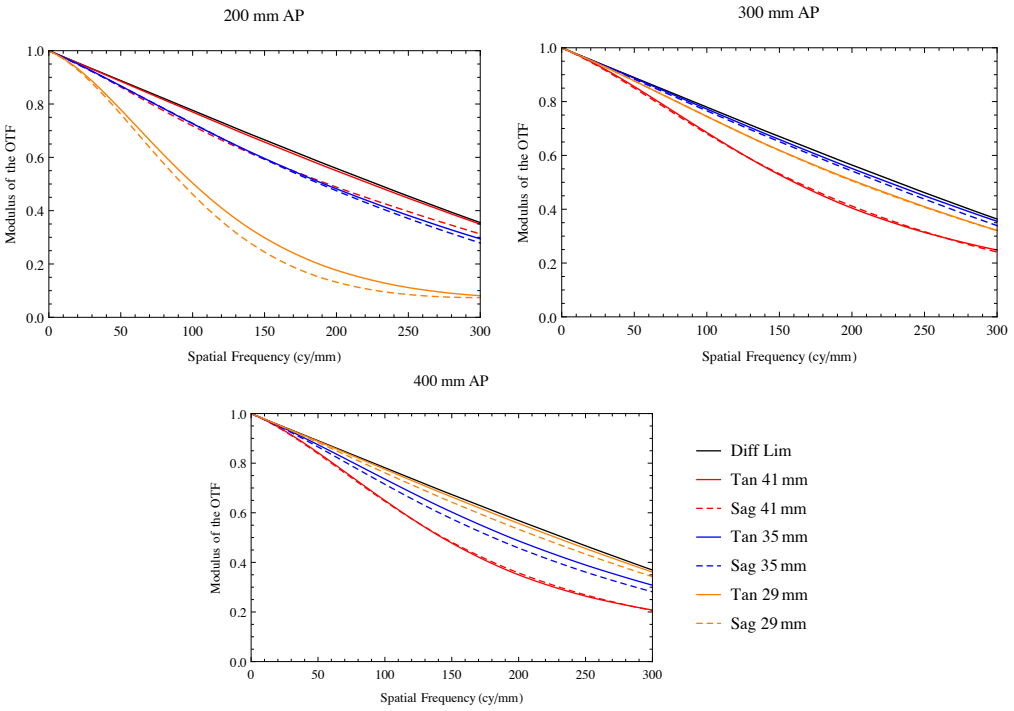

Figure 4.8: MTF for object positions for AP

4.9, it can be interpreted that the effective EDOF extension for the aspheric plate is limited to 200 to 350 mm by the spatial frequency requirement for iris imaging which is 40% contrast at 2 cy/mm in object space. This gives an extension to the depth of field by a factor of 2.3 times when compared to a lens conjugate to

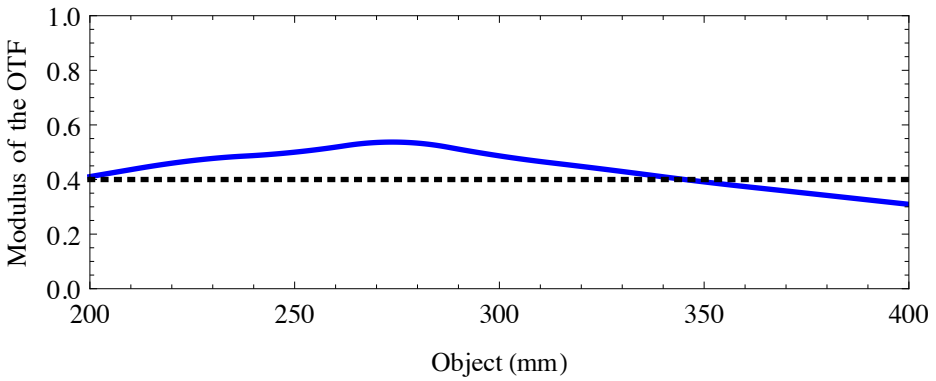

Figure 4.9: MTF variation across desired object region of the AP for maximum inter-pupillary distance $D_p = 70$ mm.

a finite object position with the same lens parameters.

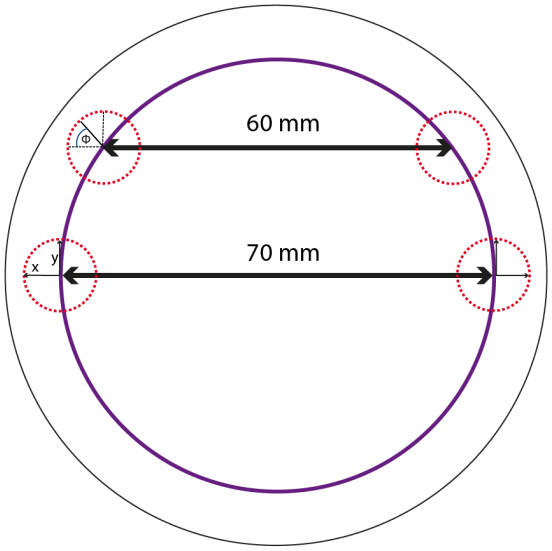

Figure 4.10: Iris separation over the AP with misalignment, where the x and y within the red dashed circle are the height and width if the imaging region.

For generalised off-axis imaging over an extended depth of field, the rotationally symmetric EDOF plate element has many advantages. One is that the element allows one to ustilise misalignment for adaption to different user interpupillary distances, as seen in Fig. 4.10. The initial design has set the interpupillary distance as D_p =70 mm. To allow for the variation in interpupillary distance the eyes can be displaced within the same annular zone which allows for a reduction in interpupillary distance. The orientation of blurring for the edge of the irises is dependent on the angle ϕ as indicated in Fig. 4.10.

The usable EDOF region for the displaced irises shown in Fig. 4.11 ranges from 260 to 400 mm yielding an extension of 2.2 times within a region further from the front vertex of the lens.

4.3.3 Zernike fringe polynomial plate (ZP)

An introduction to Zernike polynomials is given in Chapter 2. Imaging two off-axis objects of a fixed height with rotationally symmetric optics can offer the advantage of compromising the central region of the field to achieve a higher spa-

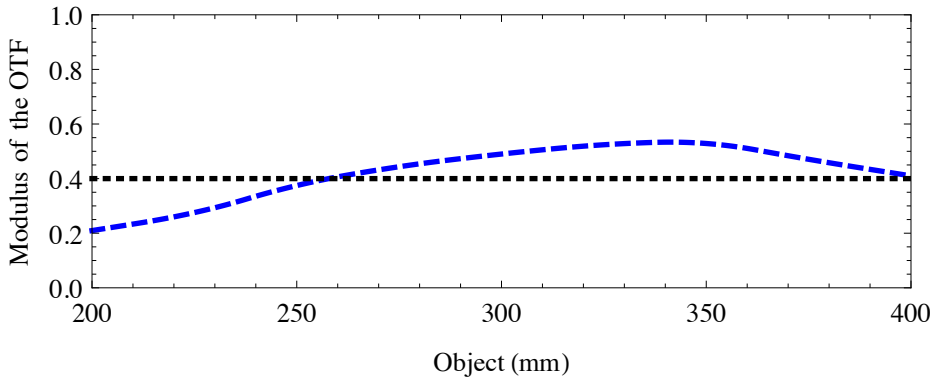

Figure 4.11: MTF variation at 2 lp/mm across desired object region of the AP for displaced irises with $x = 32 \pm 6$ mm and y=4 ± 6 mm corresponding to an interpupillary distance of $D_p = 60$ mm labelled in Fig.4.10

tial frequency towards the peripheral of the field, where the irises are located. Departing from classical optics can benefit the range of field points required for EDOF imaging. Non-rotationally symmetric surface profiles can boost the spatial frequencies in the targeted areas of interest containing ray bundles at the expense of the performance at the unwanted regions of the field. This is employed by introducing Zernike polynomials to describe the surface, where terms with a dependency in x are a priority. The basis shape for the surface must be plane symmetric about the vertical meridian as the irises are assumed identical from the bridge of the nose. This plate will be referred to as ZP in all associated plots. Already established that the image position changes in ξ' with object position l, we can also note that the relative change in η' is small. As an annular field is not a requirement, we can prioritise the meridian in x as this plane determines the field of view. Therefore, breaking rotational symmetry can offer a boost to the MTF of the lens across a range field angles along the sagittal plane. A circular aperture is most common in photography thus the reasoning behind the choice of polynomials is clear. As the modified surface, Surface 8, is simply described by a combination of Zernike terms, the sag of the plate is reduced to the sum of the terms:

$$z = \sum_{i=1}^{N} A_i Z_i(\rho, \phi) \tag{4.1}$$

4.3. EDOF plate for radially varying iris images

Zernike polynomials are widely used for surface description in freeform optics for aberration correction[95; 96]. In this application, the non-rotationally symmetric nature for a combination of polynomial terms can be advantageous for displacing multiple ray bundles by a single surface. Surface 8 is assigned a Zernike Fringe surface, where the base terms used to create the sag have a dependency on x, primarily the astigmatism family, and additional terms to compensate for the y field listed in Table 4.5. The plate is optimised for the same object region ranging from 200 to 400 mm,as described in Section 4.3.2,.

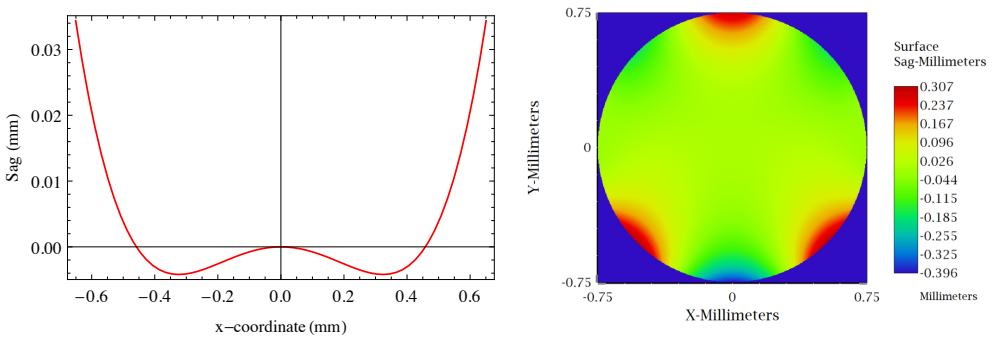

Figure 4.12: Cross section of the sag of the Zernike surface along the x-axis and surface sag profile.

Zernike Term	Coefficient	Value (Waves)
4	$2\rho^2 - 1$	7.7714×10^{-5}
5	$\rho^2 \cos\phi$	8.3556×10^{-4}
11	$\rho^3 \sin 3\phi$	-1.960×10^{-4}
12	$(4\rho^2 - 3)\rho^2 \cos\phi$	-5.037×10^{-6}
20	$(5\rho^2 - 4)\rho^3 \cos 3\phi$	-4.696×10^{-8}
21	$(15\rho^4 - 20\rho^2 + 6)\rho^2 \cos 2\phi$	6.1341×10^{-9}
27	$\rho^5 \sin 5\phi$	1.354×10^{-6}
28	$(6\rho^2 - 5)\rho^4 \sin 4\phi$	-1.005×10^{-8}
32	$(56\rho^6 - 105\rho^4 + 60\rho^2 - 10)\rho^2 \cos 2\phi$	9.1824×10^{-12}

Table 4.5: Zernike terms for the non-rotationally symmetric plates.

A cross section along the sagittal plane is also shown in Fig. 4.12 (left). The

sag difference in the meridian of interest, along x, is 0.034 mm. Sag peaks visible on the top and bottom of the surface profile are a consequence of optimisation for a non-rotationally symmetric image area. This sag could be modified at the manufacturing stage to exclude the sag peaks, the regions shown in red. That is, the cross-sectional area of interest on the ZP in which the ray bundles for imaging the iris can be prescribed in ISO drawings. Areas of the ZP that include element sag not required for imaging critical ray bundles can be manufactured or polished to have a gradual slope inclination that is more suitable for tolerancing and opto-mechanical mounting. Distortion along the ξ-meridian has a maximum value of 0.21% in the regions where the irises are imaged.

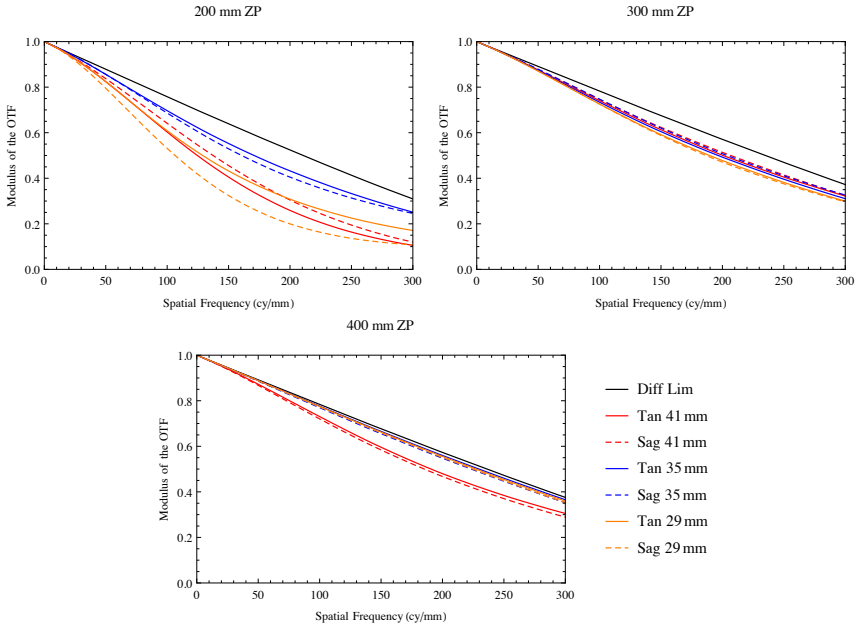

Figure 4.13: MTF for object positions with ZP plate

The improvement in spatial frequency response for the three chosen discrete object positions is shown in Fig. 4.13. The MTF at the critical spatial frequency for iris imaging across a range of object positions is shown in Fig. 4.14

The Zernike plate has the capability to image the two irises from 200 to 400 mm inclusive yielding an increase in depth of field of $\Delta Z = 3.1$ times that of the conventional lens introduced in Section 4.3.1.

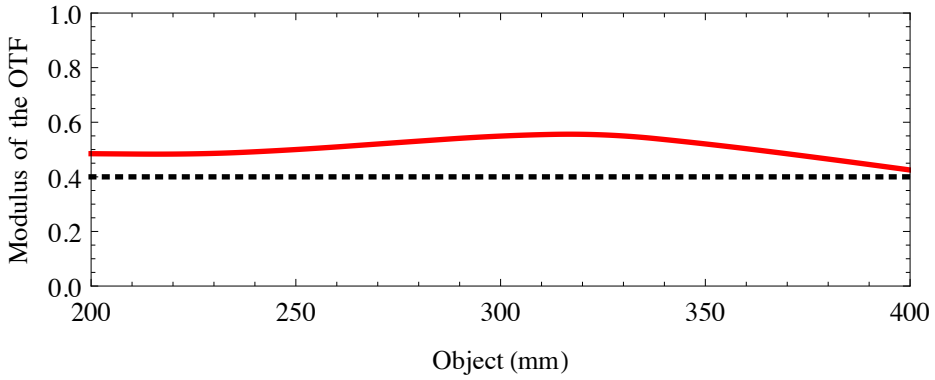

Figure 4.14: MTF variation across desired object region for Zernike modified plate.

4.3.4 Curved plate (CP)

The compensatory effect of a curved plate is compared to the planar plate with a singular polynomial surface for EDOF in Section 4.3.1, and is denoted as CP. The three proceeding lenses, surfaces $1-6$, remain unchanged from the examples previously presented in this study, where central thickness of surface 7 element and the back focal distance of surface 8 are constant. The radii of curvature for surfaces 7 and 8 are optimised, for the condition where $R_7 = R_8$ with a conicoid of revolution of $\kappa = -1$ on both.

Surface	Radius	Thickness	Material	Conic
7	-5.0387	0.1	E48R	-1
8	-5.0387	0.0825	Air	-1

Table 4.6: Lens data for the curved-plate system, all lens data including thicknesses remain the same as all other solutions. Surfaces 7 and 8 are optimised to have radii of curvature $R_7 = R_8$.

The lens data for the curved plate is presented in Table 4.6. For the modified lens the optical power is modified thus the focal length is decreased to $f = 3.61$ mm and $\mathrm{F}\#_w = 1.825$, reducing the speed of the lens-plate combination compared to the planar versions due to the additional power provided by the curved plate. Surface 8 is also assigned a polynomial surface described by Zernike polynomials in Eq. (2.57) where the terms are listed in Table 4.7.

Zernike Term	Coefficient	Value (Waves)
5	$\rho^2 \cos\phi$	0.0157
11	$\rho^3 \sin 3\phi$	-0.0630
12	$(4\rho^2 - 3)\rho^2 \cos\phi$	0.0194
21	$(15\rho^4 - 20\rho^2 + 6)\rho^2 \cos 2\phi$	2.2845 $\times 10^{-3}$

Table 4.7: Zernike terms for the non-rotationally symmetric curved plate.

The ag difference of the curved plate including the Zernike surface is shown in Fig.4.15. The maximum sag deviation of the curved plate along the x-meridian is 0.030 mm, which can be attributed to the radius of curvature of the two surfaces.

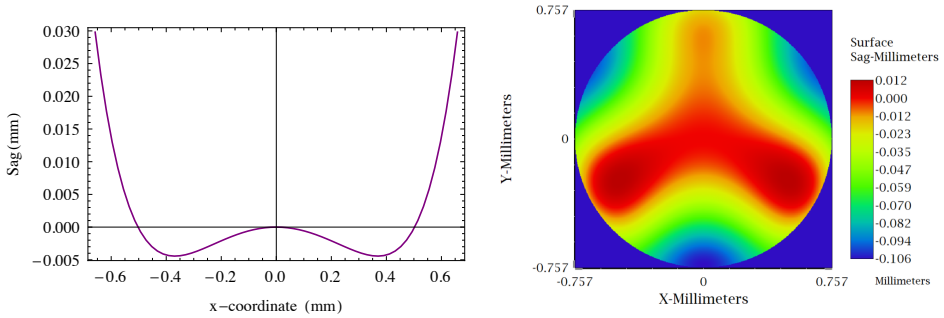

Figure 4.15: Cross-section sag difference between surfaces of the CP. Surface sag of surface 10, where the sag is the combined radius of curvature and Zernike fringe terms.

Critical spatial frequency of 40% modulation is different from the planar plate designs as the optical power is altered with a non-zero radius of curvature for surface 7 and 8 . The modified spatial frequencies are listed in Table 4.8.

Object (mm)	Spat Freq (lp/mm)
200	109
300	164
400	220

Table 4.8: Spatial frequency in image space required to image the iris at 2 lp/mm.

MTF plots shown in Fig. 4.8 show the curved plate performing well at larger object distances and reducing quality with increased image height from the axis.

This can be attributed to the radius of curvature suiting images formed in close proximity to the optical axis.

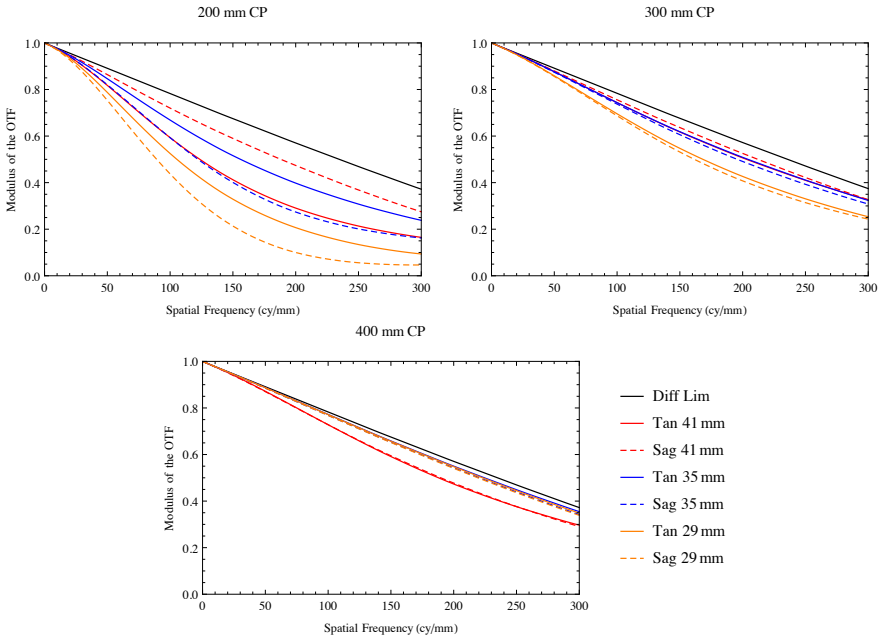

Figure 4.16: MTF for object positions with curved plate CP

The EDOF region in which the irises can be sufficiently detected ranges from 240 - 400 mm, shown in Fig. 4.17, yielding an improvement of $\Delta Z = 2.5$ times.

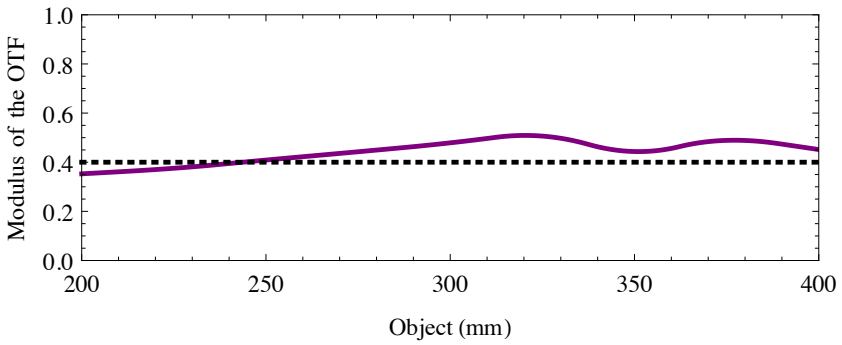

Figure 4.17: Usable EDOF region with curved plate CP.

Comparative analysis of radial plates

The polychromatic rms wavefront error (WFE) across the field for all plates is presented in Fig. 4.18. For the full field plot (top), it can be clearly seen that the regions about the axis can be compromised for larger field angles, which have rms WFE values visibly above 0.4 waves. It is noted that the aspheric plate at 200 mm, plotted in a continuous blue line, has a sharp increase in rms WFE at the field point ±38 mm.

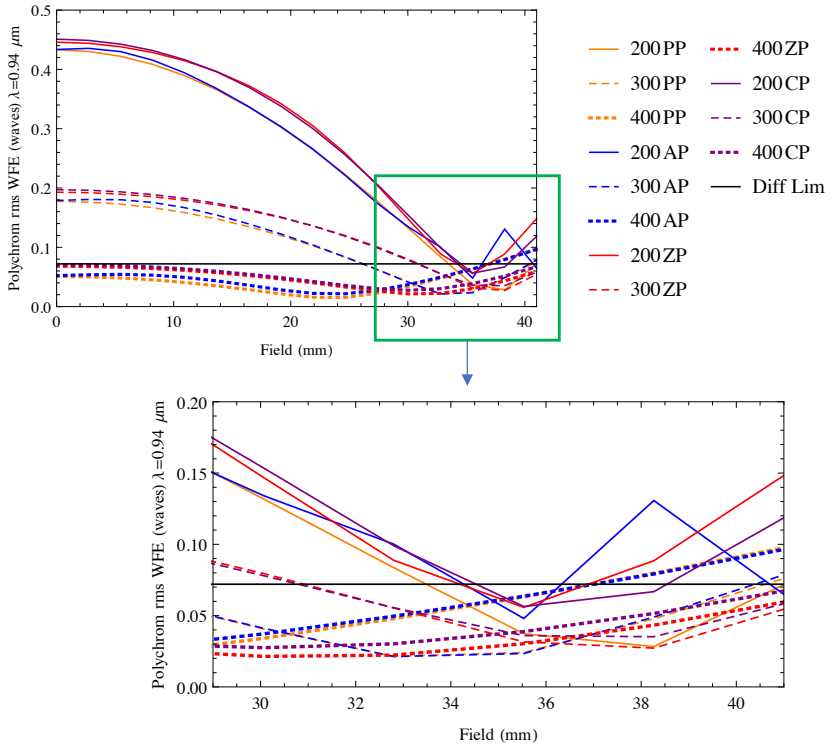

Figure 4.18: Comparison of rms vs field (+x) for $\lambda = 0.94\mu m$ with PP - planar plate, AP - aspheric plate, ZP - Zernike plate.

The region of interest is the area surrounding the irises, ±x= 35 ± 6 mm. The plot containing the irises (bottom) shows that the initial lens with the parallel plate can capture 350 and 400 mm while performing very poorly at large field angles as the irises approach the lens at 200 mm. An increase in WFE arises with the aspheric surface struggling with the variation in radial profile required to compensate the image position.

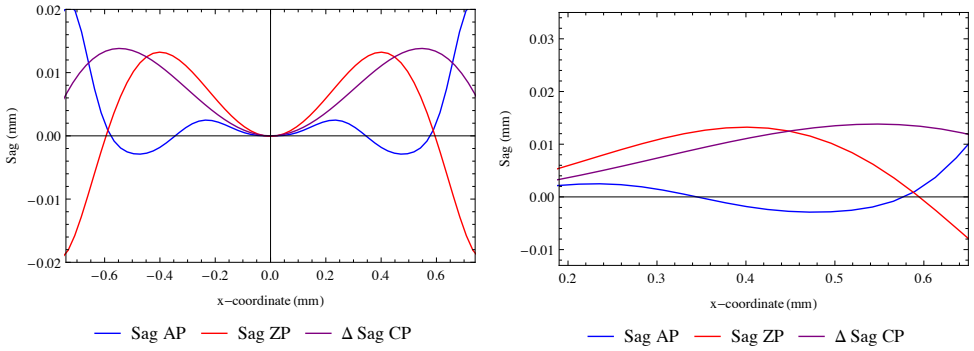

Figure 4.19: Sag difference of all modified plates, full element diameter (left) and the the illuminated region shown (right).

The aspheric plate shows that for the regions of interest the contrast at 200 remains low although shows an improvement on the parallel plate for the same region. This is reiterating the incapability of the lens and aspheric plate combination to meet the 40% at 2 cy/mm in object space for large field angles. The difference in sag for the iris region of interest can then be plotted, shown in Fig. 4.19. In the case that the y-field is zero, the surface sag of the three elements would appear similar in shape with varying surface slopes. However, due to the non-zero y-field that encloses the height of the irises the ZP and CP can be modified by adding y-dependent polynomial terms in Eq.(4.1), which adjusts the sag encompassing all field points. The aspheric plate does not share this characteristic, described by Eq.(2.19).

The extended range of object positions over which the lens can image the irises is one metric for determining the suitability of the plates to the application. The extension in depth of field can be quantified by comparing the MTF performance between 200 mm and 400 mm as shown in Fig. 4.20. The optimised lens with the parallel plate is shown to struggle with large field angles but achieve an increase of two-fold in depth of field. The aspheric lens can correct for the large field angles, but cannot compensate for the long object distances. The Zernike plate shows a variation in performance across the EDOF range while all are above 40% contrast.

The combined lens and plate sensitivity to misalignment of the user is plotted by the dashed lines in Fig. 4.20. The CP and ZP can be seen to be unaffected by

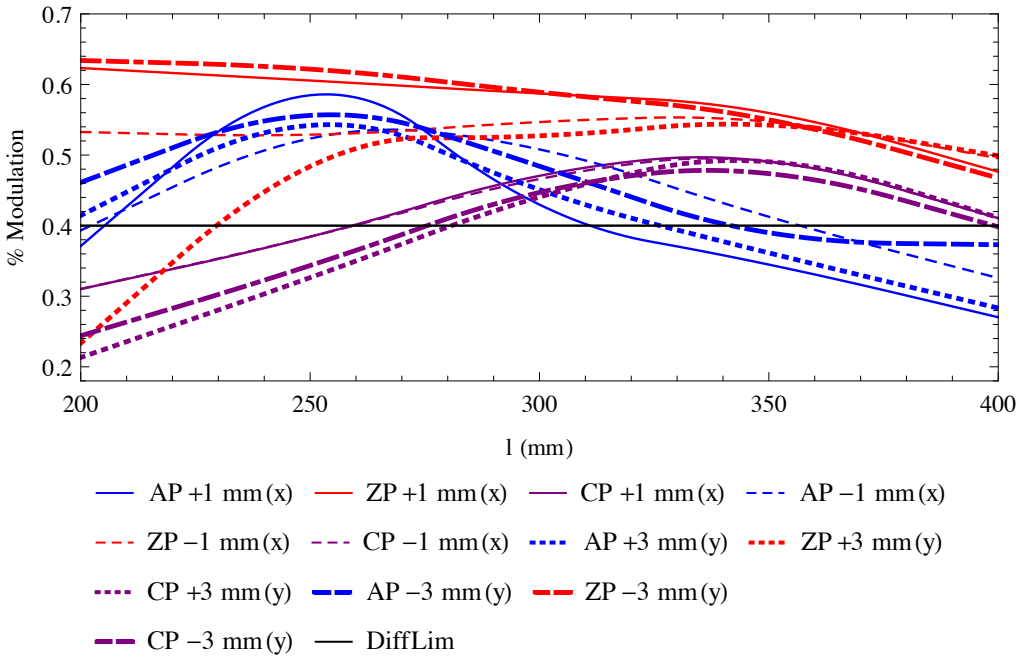

Figure 4.20: MTF as a function of object position for misalignment or iris position

the misalignments. The misalignment of the Zernike plate by +3 mm vertically falls below the limit of iris recognition at distances closer to the lens. From Fig. 4.12 (right) it can be seen that the sag changes toward the bottom of the surface such that a decenter with a positive height (+y) will generate a lateral shift in the image in the opposite direction generating a longitudinal image shift that moves the image point further from the CCD plane. It can also be noted that a tilt of the head with respect to the lens, which is within the depth of field and below a 10 percent tilt will have a negligible effect as both irises will be positioned in different zones of the lens and so remain imaged. Figure 4.20 shows the apparent inability of the curved plate to image with good quality at large field angles. The radius of curvature which was initially thought to aid the refraction angles for imaging lowering image quality.

The back surface of the plate in this design is solely responsible for image point displacement with respect to the object positions. Figure. 4.22 shows a footprint diagram of Surface 8, where all ray bundles propagate through the plate surface together. It can be observed that the ray bundles are overlapping, in

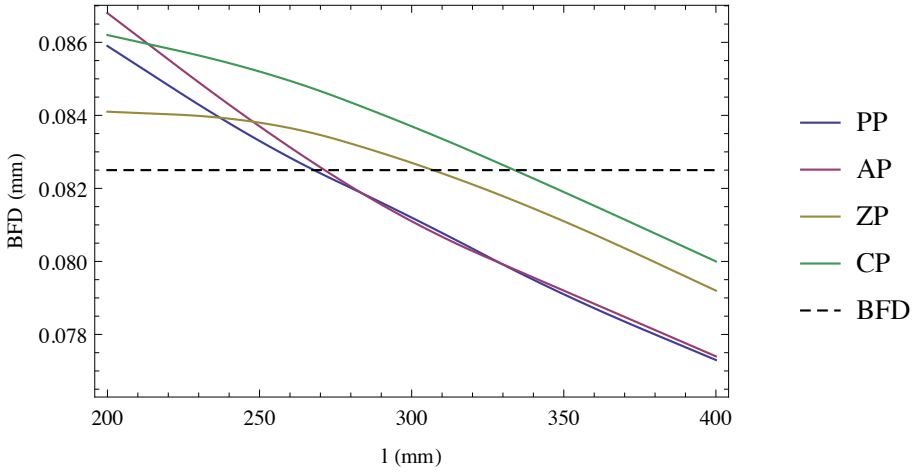

Figure 4.21: BFD vs object position for all plate designs

particular as the bundles approach the center of the plate. These overlapping ray bundles create a demanding variation in sag across the element surface. This solution proves too sensitive to misalignment for use in miniature devices due to the natural movement of the user and the handheld device. However, for a fixed

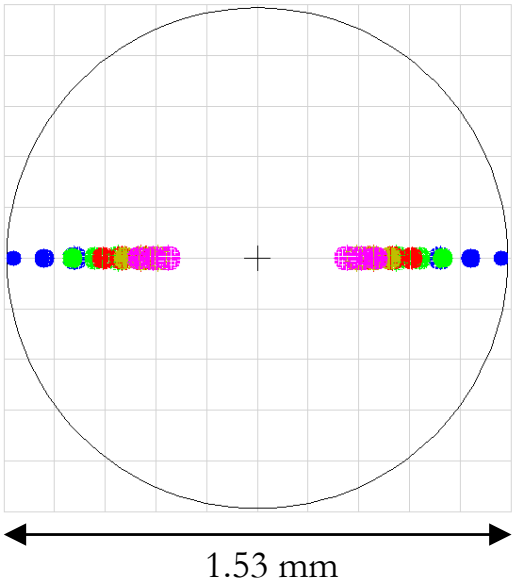

Figure 4.22: Footprint of EDOF element with horizontal variation taken from Zemax.

position camera such as in automotive biometric cameras this design could prove to be a valuable asset for refocusing.

4.4 Irises varying in height

The second configuration presented in Section 4.2 is the vertically varying iris position. The iris images on the detector are now separated spatially in both x and y. Re-optimisation of the lens from Section 4.3.1 is carried to suit modifications made in object positioning in the field. The corresponding data is presented in Table 4.9 and 4.10. The lens consists of three plastic components where the first is an air-spaced doublet which is achromatic within the lens compensating for chromatic aberration induced by the plate and third lens. The lens parameters are optimised for the object distances and respective heights as listed in Table 4.11 with a parallel plate, indicated by surfaces 7 and 8. These surfaces are modified during the study in Sections 4.4.1 and 4.4.2.

Surf	Rad (mm)	Thick (mm)	Glass	Conic
1	3.0032	0.7000	PMMA	-1
2	-27.7637	0.0327	Air	-1
3	1.2552	0.7000	E48R	-1
4	0.7984	1.000	Air	-1
5	2.2545	0.7436	E48R	-1
6	-5.8871	1.3122	Air	-1
7	Infinity	0.1000	E48R	0
8	Infinity	0.0875	Air	0

Table 4.9: Lens data for lens and parallel plate with the vertical positioning of irises with object position.

Figure 4.23 presents the lens layout as modelled in Zemax with an entrance pupil diameter of 2 mm and a focal length of 3.48 mm, yielding an average working F-number of $F\#_w$=1.76. The average F-number is taken as multiple object positions are imaged with this lens. The total track length of the lens is 4.67 mm where the stop is positioned on Surface 1. For vertical iris movement the

Surf	A (mm^{-3})	B (mm^{-5})	C (mm^{-7})	D (mm^{-9})
1	0.0254	1.1204 $\times 10^{-3}$	-3.941 $\times 10^{-3}$	-2.445$\times 10^{-5}$
2	0.0212	-7.258 $\times 10^{-3}$	-4.273 $\times 10^{-3}$	-8.878 $\times 10^{-6}$
3	-6.818 $\times 10^{-3}$	-0.0220	-3.429$\times 10^{-3}$	-1.6362 $\times 10^{-5}$
4	0.0205	-0.0629	8.8140$\times 10^{-3}$	-1.126$\times 10^{-4}$
5	-0.0133	-0.0207	-1.508$\times 10^{-3}$	8.0644$\times 10^{-5}$
6	8.3403$\times 10^{-3}$	-0.0275	3.8030$\times 10^{-3}$	1.1654$\times 10^{-4}$
7	0	0	0	0
8	0	0	0	0

Table 4.10: Aspheric coefficients for lens and parallel plate with the vertical positioning of irises with object position, where A, B and are even aspheric coefficients of 4^{th}, 6^{th}, 8^{th} and 10^{th}.

performance of the modified lens-parallel plate combination will be denoted as PPV.

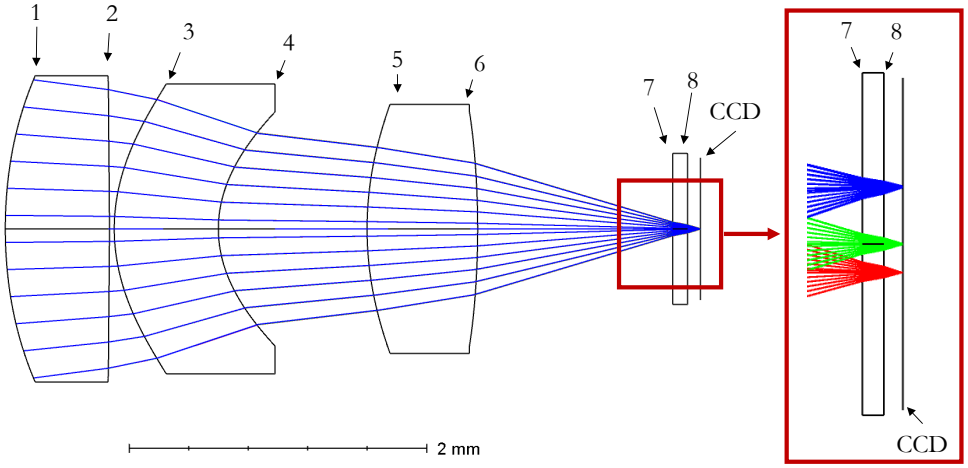

Figure 4.23: Lens layout from Zemax with prescription from Table 4.9 with a y-z coordinate system. The diagram corresponds to the irises positioned at 300 mm from the vertex of the lens in the main diagram. All three object-image conjugates are shown in the red box where the red bundle of rays corresponds to an object at 400 mm, green at 300 mm and blue at 200 mm with heights according to Table 4.11.

The lens has -0.26 μm of lateral colour which lies inside the Airy disk of radius

2.02 μm at the largest field angle. A maximum distortion of -0.69% is induced at l = 200 mm around the area of interest enclosing the irises, decreasing with an increasing value of l.

Object (mm)	Y-Field (mm)	X-Field (mm)
200	− 15	32 ± 6
300	0	32 ± 6
400	+ 15	32 ± 6

Table 4.11: Iris positioning in object space, where the average interpupillary distance is taken as 32 mm.

The back focal distance for the lens presented in Table 4.9 over a range of object distances from 200 to 400 mm is plotted in Fig. 4.25. The choice of the furthest distance of 400 mm is the to the limit of angular resolution of the lens with a fixed diameter of 2 mm. The shift in back focal distance is Δ_{BFD}= 0.0187 mm. The lens presented here has a depth of focus of Δz = 0.0062 mm, meaning that the nearest and furthest object distances of the parallel plate design will lie outside the depth of focus, resulting in a blurred image in which the irises cannot be resolved. As the image blur is a result of defocus, a shift in the image position to within the depth of focus can image quality to sufficiently resolve the irises. It is clear from Fig. 4.25 that a parallel plate does not influence a change in the BFD therefore the profile of the BFD with a displacement of image position is

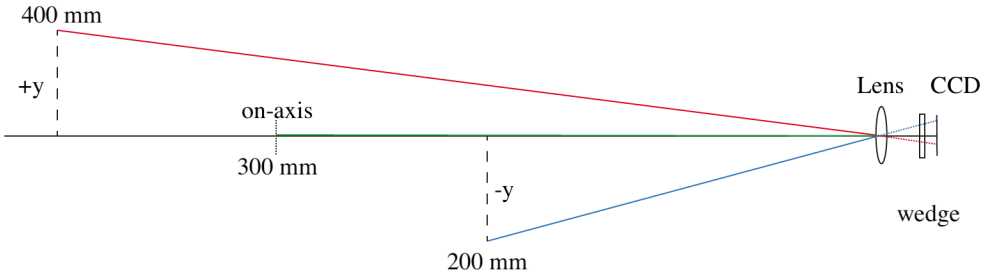

Figure 4.24: Visual representation of Table 4.11 where the irises for discrete object positions are positioned at separate heights in the field to be imaged on the separate regions of the detector.

determined by the lens and aspheric terms. To compensate the BFD variation shown in Fig.4.25, two solutions are proposed. The first is a simple wedge element where the planar surface of Surface 8 is tilted in Section 4.4.1. The second is a cylindrical-wedge element where Surface 7 is cylindrical and Surface 8 is tilted, this is presented in Section 4.4.2.

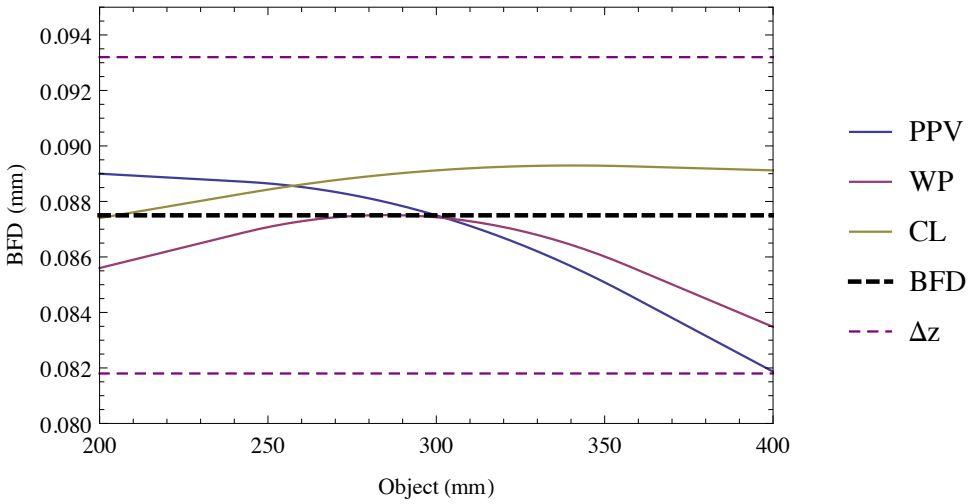

Figure 4.25: Variation in image position with respect to object position for the lens with parallel plate listed in Table 4.1. The linear trend produced by the parallel plate can be compensated by replacing the plate with a novel optical element. Comparative study includes parallel plate with vertical iris position (PPV), linear wedge plate (WP), and cylindrical lens (CL).

The image is conjugate to an object at positioned at 300 mm. The total depth of field for this lens would be $\Delta Z = 69.91$ mm. All extensions in depth of field for this design orientation will be compared to this value.

4.4.1 Planar wedge element (WP)

The irises are positioned at a fixed vertical height with respect to object distance with positions laid out in Table 4.11, and visually represented in Fig. 4.24. To compensate the variation in the back focal distance, a simple wedge solution is proposed where the thickness of the wedge decreases from bottom to top, abbreviated in all figures as WP.

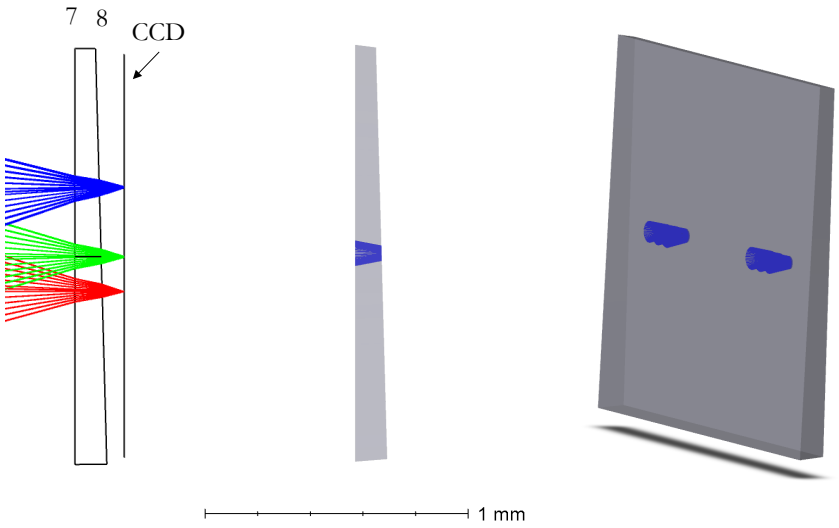

Figure 4.26: Lens with planar wedge where the tilt of surface 8 is optimised to compensate the variation in BFD

A tilt about x of -1.56 deg is assigned to Surface 8 creating a wedge element which keeps the original central thickness but now is thicker towards the bottom and thinner at the top compensating for the irises when positioned as in Table 4.11, shown in Fig. 4.26. The wedge element has the same horizontal profile $\pm x$ with a change in $\pm y$ and so the interpupillary distance correction is dependent on the field correction of the preceding lenses. The variation in BFL for this element is shown in Fig. 4.25 (plotted in purple) which shows that on-axis the wedge solution can displace the image points sufficiently to resolve the irises over the given object range. To analyse the performance of the wedge the the irises are misaligned and the results are shown in Fig. 4.27. The wedge offers an extension in depth of field of 2.15 times compared to a lens of similar parameters.

Misaligning the eyes with respect to the lens results in a loss in contrast at the furthest object regions, reducing the usable depth of field for the wedge. Further consideration is required to make the wedge more robust and less sensitive to misalignment. The wedge and lens have -0.2559 μm of lateral colour and an Airy radius that varies from 2.02 to 2.01 μm which indicates that lateral colour is not problematic in this design. The maximum field curvature present is 0.60% for the field containing the irises.

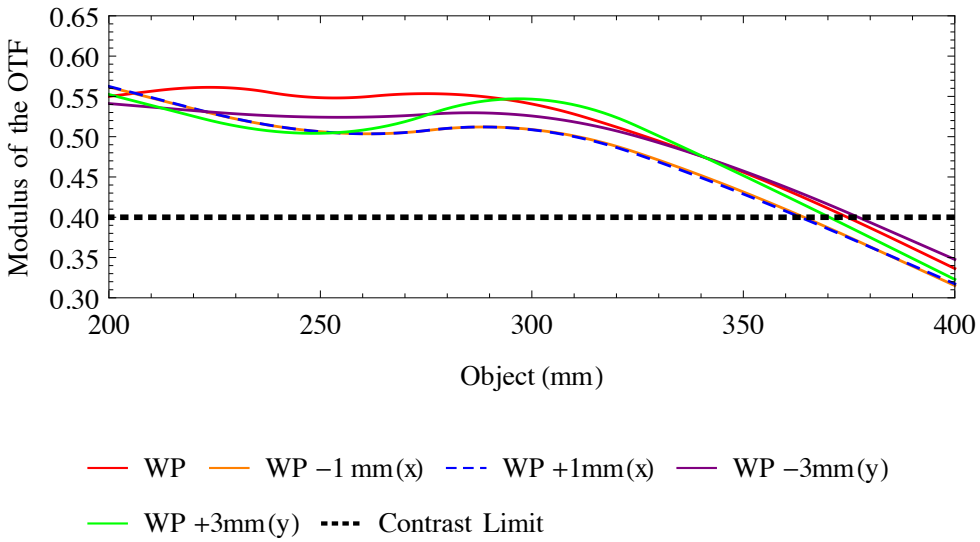

Figure 4.27: Misalignment of irises with respect to the lens and plastic wedge element.

4.4.2 Cylindrical wedge element (CL)

To increase the EDOF region of the simple wedge, a solution is proposed to minimise the refraction through the plate. This is done by conjugating surface 7, the front surface of the plate, to the aperture stop, creating a CL. When considering the principal ray, the exit pupil is the conjugation plane, however the aperture stop is chosen here as the best position for minimising refraction of both principal and marginal rays.

The front surface of the wedge is assigned a biconic surface, which can be described as:

$$z(x,y)_{biconic} = \frac{c_x x^2 + c_y y^2}{1 + \sqrt{[1-(1+k)c_x^2(x^2+y^2) - (1+k)c_y^2(x^2+y^2)]}}, \tag{4.2}$$

where the radius of curvature $R_x = 1/c_x$ is set to zero to generate a cylindrical surface:

$$z(x,y)_{cylinder} = \frac{c_y y^2}{1 + \sqrt{[1-(1+k)c_y^2(x^2+y^2)]}}. \tag{4.3}$$

The vertical radius is concentric to the exit pupil of the lens with R_y= -4.589 mm and the horizontal radius R_x remains planar. As R_y is concentric to the aperture stop, the refraction angles of the principal ray and marginal rays are reduced at

Surface 7. The back surface is optimised for a tilt to create the optimum thickness variation with height over the wedge to compensate the variation in BFD, the tilt on the wedge in our design is -3.13 deg. The lens and cylindrical plate combination has a maximum of -0.53% in x for the closest object position. The Airy radius has a value of 2.04 to 2.02 μm for the object range 200 to 400 mm. A maximum of -0.2 μm of lateral colour is induced which can be considered negligible when compared to the diameter of the Airy disk.

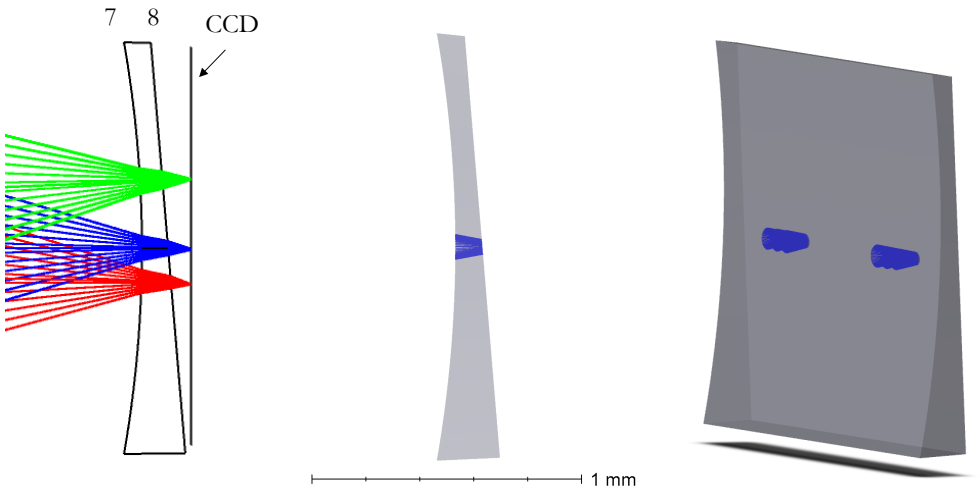

Figure 4.28: Lens with biconic wedge where the R_y of surface 7 is concentric to the exit pupil of the lens. The tilt of surface 8 is optimised to compensate the variation in BFD

The cylindrical lens can achieve an imaging range of 200 to 400 mm object space, yielding an extension in depth of field of 2.9 times compared to the initial PP design.

Figure 4.29 shows that the irises can be misaligned with respect to the lens and remain above the imaging criteria. The plate is also insensitive to varying IPD as this would depend on the ability of the lens to balance field dependent aberrations. As this element accommodates all IPDs, this plate would be suited to a commercial market since the plate can be applied to any user without prior knowledge of the user IPD.

4.4.3 Comparative analysis of wedge plates

Figure 4.30 shows the rms wavefront error over the horizontal field. From this plot, it can be seen that the peripheral regions of the field, which contain the irises, are prioritised in the design of the lens. It is understood that the three elements preceding the EDOF plate are responsible for correcting the field aberrations. It is also evident that the performance about the optical axis is compromised, especially at large field angles when the irises are positioned at 200 mm yielding an rms WFE of 0.45 waves at λ= 940 nm.

There is very little difference in performance between the tilted wedge and biconic wedge elements with central positioning of the irises i.e. positioned within the designated region. The rms WFE for all object distances varies from 0.02 to 0.025 waves. However, the main difference between the wedge and cylindrical elements lies in the sensitivity to misalignment. Comparing misalignment of the irises for both elements is shown in the respective sections. Figure 4.27 represents the achievable MTF for the spatial frequency at 2 lp/mm for imaging the iris.

As expected the irises can be misaligned with respect to the lens-plate combination with little decrease in MTF. It is also seen that the wedge cannot

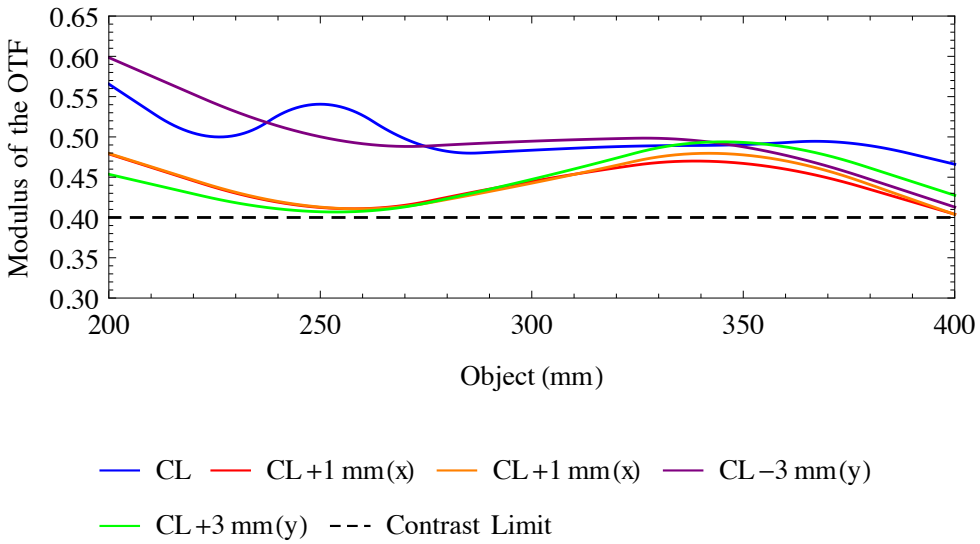

Figure 4.29: MTF over the EDOF region with iris misalignments.

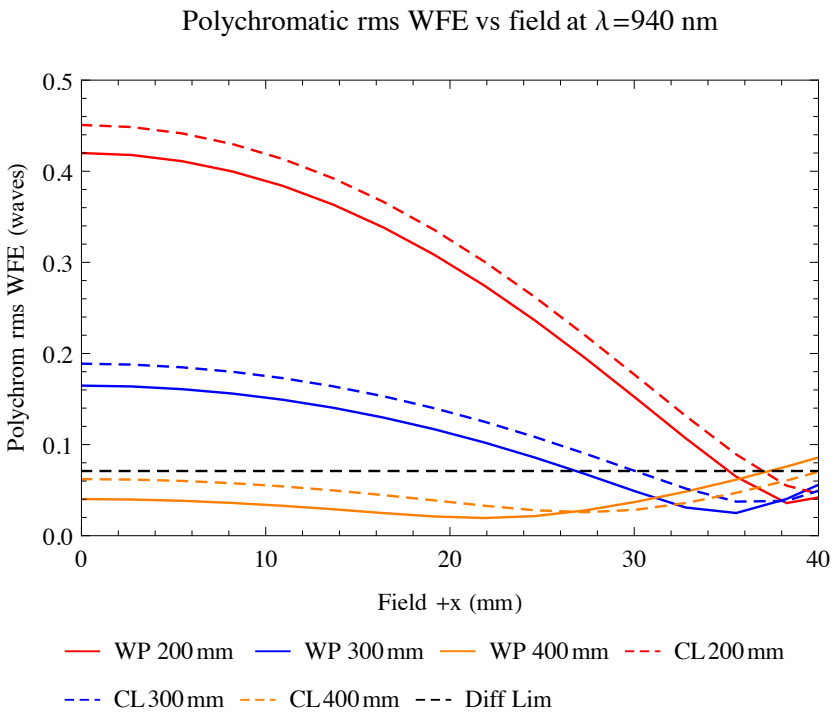

Figure 4.30: Root mean squared wavefront error across field (+x) for the tilted wedge WP and cylindrical lens CL. Little effect between the wedge and biconic designs on-axis.

compensate the image position for large object distances with a tilt of Surface 8. Misalignments of the irises for the cylindrical lens is shown in Fig. 4.29. The total Seidel aberrations at the image plane are shown for all variations of the vertical plate in Fig. 4.31. A variation in field curvature, shown by the green box, demonstrates the advantage of implementing the cylindrical surface and tilted surface combination. This combination also induces coma such that there is a positive residual, seen in the third column of Fig.4.31. The modification of the plates have a minimal effect on chromatic aberration and so are not shown. Image surfaces are shown with respect to the CCD plane in Fig. 4.32. Parabolas are used to plot the image surfaces for simplicity. The centre field image points are formed behind the CCD plane which allows for the field curvature to allow for the off-axis images to be formed about the CCD plane.

Image surfaces can be grouped by conjugate object distance and scaled, shown in Fig. 4.33. The leftmost box represents the image surfaces produced by irises

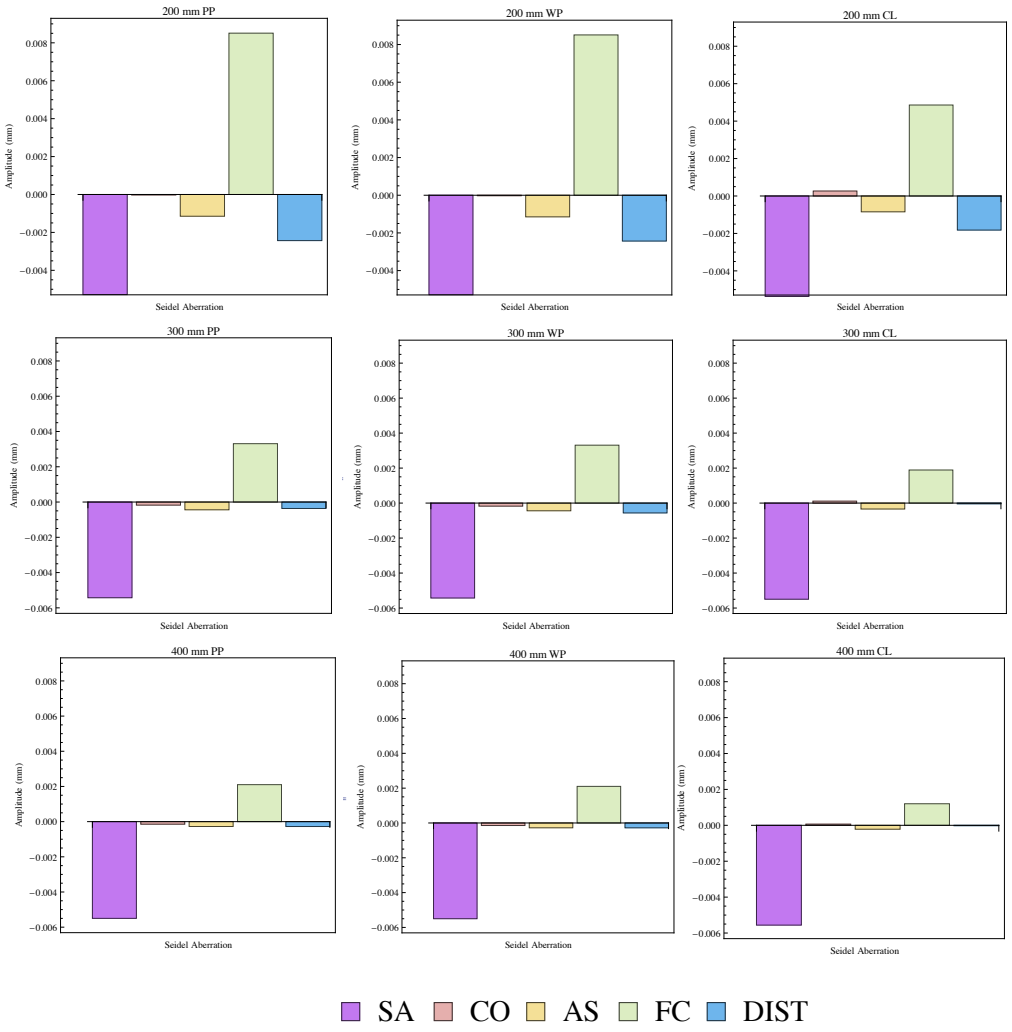

Figure 4.31: Total lens monochromatic Seidel aberrations for all vertically varying plates: first column represents the lens-parallel plate PP combination, the second column contains aberrations of the lens-wedge plate WP, and third column shows the monochromatic aberrations of the lens-cylindrical lens WP combination.

positioned for $l = 200$ mm at $y = -15$ mm, $l = 300$ mm at $y = 0$ mm in the centre box, and rightmost box contains the image surfaces for $l = 400$ mm at $y = +15$ mm.

Image surfaces for $l = 200$ mm show that both the wedge and cylindrical surface modifies the position of the images with respect to the parallel plate images. Minimal modifications are ideal for objects at 300 mm as the lens is optimised

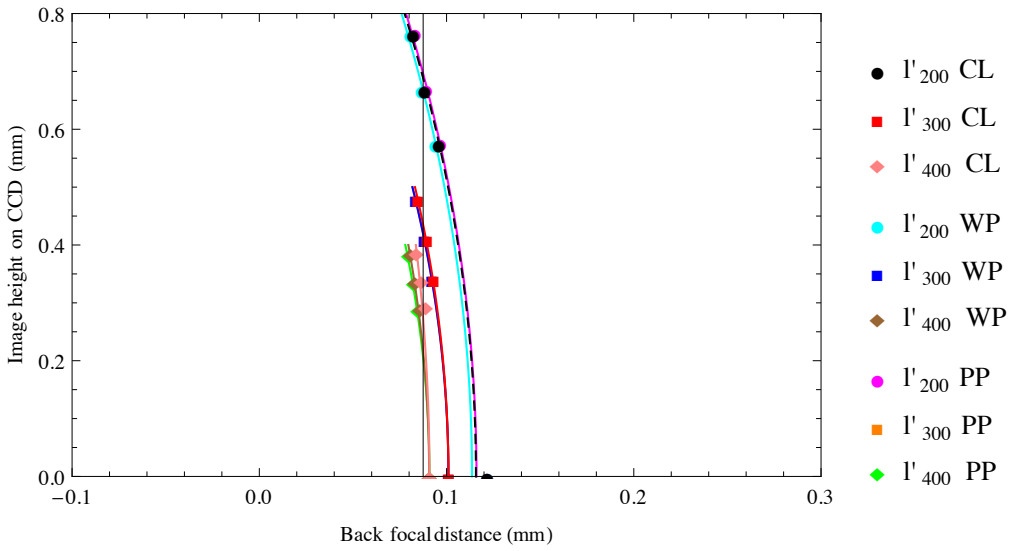

Figure 4.32: Image surfaces for objects positioned at (left) 200 mm, (middle) 300 mm and (right) 400 mm as defined in Table 4.11 with height in +x.

for this position. Wedge and parallel plate image surfaces demonstrate identical behaviour with coinciding parabolas while the introduction of the cylindrical surface displaces the image surface, due to the decrease in field curvature seen in Fig. 4.31. The rightmost box containing the image surfaces for objects positioned at $l = 400mm$. The thickness of the plate required to displace the image points is larger than the central thickness of the plate. The wedge plate shows a modest change in surface shape. However, it is the cylindrical lens that successfully displaces the image points toward the CCD plane where the images can satisfy the spatial frequency criterion for imaging the iris at 2 lp/mm, already seen in Fig. 4.29. The modest displacement of image points shown by the wedge explains the inability of this solution to image the furthest object region, seen in Fig. 4.27.

There is much focus in the consumer industry on principal ray angles incident on the CCD plane. Detector manufacturers suggest keeping the edge-most PR angle below 35 degrees for most commercial sensors. Figure 4.34 shows that the designs presented here adhere to detector guidelines and should not create problematic crosstalk between pixels.

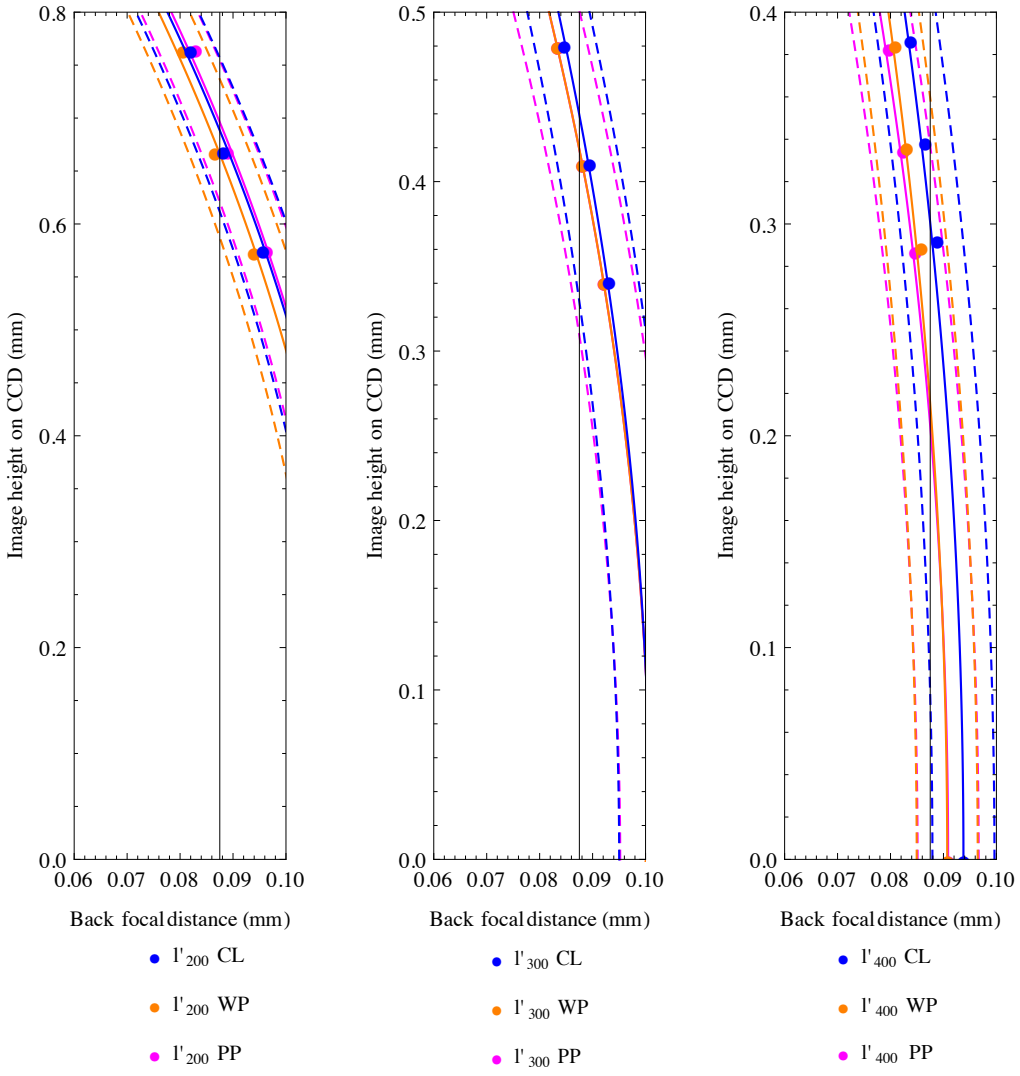

Figure 4.33: Image surfaces for objects positioned at (left) 200 mm, (middle) 300 mm and (right) 400 mm as defined in Table 4.11.

4.5 Conclusion

Two design configurations for imaging both irises over an extended depth of field are presented. Each design configuration presents multiple solutions. The iris dimensions are chosen for the case of maximum separated irises, an IPD of 35 ± 6 mm. A smaller IPD can be chosen for a specific user. Although this design is based upon simple geometry and therefore decreasing the IPD will decrease

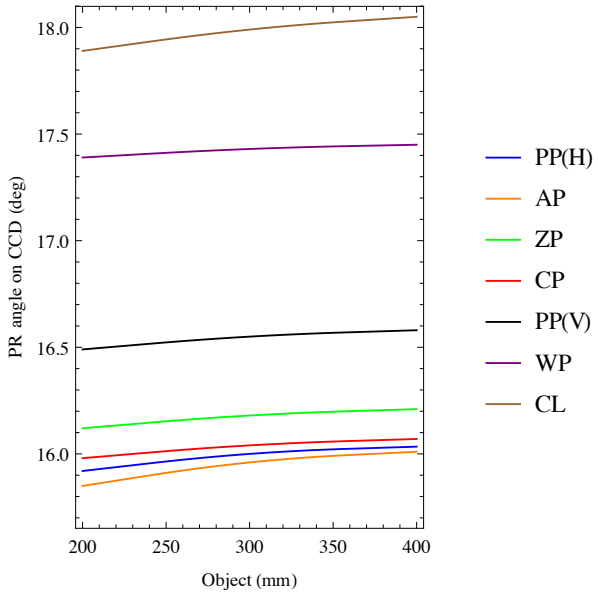

Figure 4.34: PR angle incident on CCD plane for all plate solutions.

the principle ray angle and so reducing the required image displacement. This statement only holds for a lens of the same parameters. Considering all lenses, smaller interpupillary distances have smaller field angles and so do not induce large amplitudes of field dependent aberrations. It is important to note that the degree of variation of the sag across the plate surface is fundamentally dependent on the lens preceding the plate. The sole purpose of the plate element should be for image point displacement.

Two viable solutions for the high yield consumer market would be the Zernike radially varying plate and the cylindrical lens vertically-varying plate. Both plates are capable of extending the depth of field of their associated lenses by 3.1 and 2.9 times respectively. Both solutions show an acceptable tolerance range, where the Zernike plate shows a critical decrease in MTF at large principle ray angles as the irises are displaced vertically. One aspect to note in design is that the radially varying thickness plates should be produced specifically for a user specific IPD due the demanding sag variation required. This is not the case for the vertically thickness varying plates as the statistical variation in IPD is corrected for in the fundamental field dependent aberration correction with aspheres on surfaces 1 to

6. It is this reason that the vertically thickness varying plates would be the best solution for a high yield market such as the consumer imaging market. As the lens-plate combination can be used by all IPDs, then the specificity for biometric imaging would be dependent on the calibration and software.

Chapter 5

Dual F-Number Widefield Lens with Variable Depth of Field

5.1 Introduction

This chapter addresses depth of field in widefield photographic lenses for imaging in the visible spectrum. In contrast to the previous chapters, the lens presented here is not limited to strict spatial frequency requirements for biometric identification. Instead, this work demonstrates more traditional optical design methods to achieve an extended depth of field over a large field of view.

Traditional smartphone lenses have low F-numbers with four to six plastic elements comprised of highly aspheric surfaces. The term traditional in this sense refers to the extreme element shapes required for aberration correction over a short TTL in miniaturised cameras. The fundamental parameter for these lenses is the TTL, that is the depth of the lens barrel from the front vertex to the image plane. The TTL is assigned by the manufacturer of the device. In the past, this thickness typically had a value of 5 mm. This fundamental design restriction ultimately formed the guidelines associated with smartphone lens design such as the aperture stop position at the front lens vertex. Stop position determines the field dependent aberration correction ability of the lens. The number of elements within the lens module is restricted to the design space. Wafer level lenses were proposed, but the resolution proved much lower than standard refractive elements [97]. To balance aberrations over the FOV current miniature camera lenses take on extreme shapes described by polynomial series. These shapes are non-intuitive for optimal aberration balancing and so brute force optimisation methods are required to find a suitable global minimum solution.

Advances within the field of optical design for smartphone lenses has resulted in exploring the feasibility of alternative surface profiles [98] [99], where improvements are effective but small due to the underlying design restrictions. Many of the recent advances in the field of mobile device imaging are computationally based, including digital refocusing and image blurring for portraiture imaging. It is proposed that if the defining parameter of these lenses could be increased, all subsequent thickness-dependent parameters could be relaxed. With this in mind, a novel lens orientation is presented where the module is repositioned within the device housing as shown in Fig. 5.1. Here, the front lens coincides with the corner of the phone or device.

A reorientation of the lens position which can be incorporated without modifying the external housing is presented in Fig. 5.1. Employing this new design concept can offer new possibilities for commercial imaging. The target application for the proposed lens is video conferencing where a large field of view is desirable. The field can be sub-sectioned such that the central field has a shallow depth of field with high resolution. The larger fields prioritise identifying others participating in the meeting, where the scene has a lower image quality but has a large depth of field that is less sensitive to a person's seating position. This effect is realised by a dual F# lens where the incoming ray bundles are vignetted to reduce the F# at larger fields. The loss of intensity on the CCD can be recovered by employing binning at the edge of the scene.

5.2 Dual F-number Widefield Lens Design

A wide angle lens is presented in this section which has a maximum TTL of 15 mm, approximately three times the TTL of camera modules found in current conventional smartphones. This extra design space is feasible by re-positioning the lens within the device housing so that the front lens is orientated at the corner of the phone or device. The combination of design space demonstrates the possibility of implementing fast lenses that resemble classical optics. An increased TTL implies that the aperture stop position can become a design parameter. Freeing the aperture stop position offers a benefit in correction of principal ray

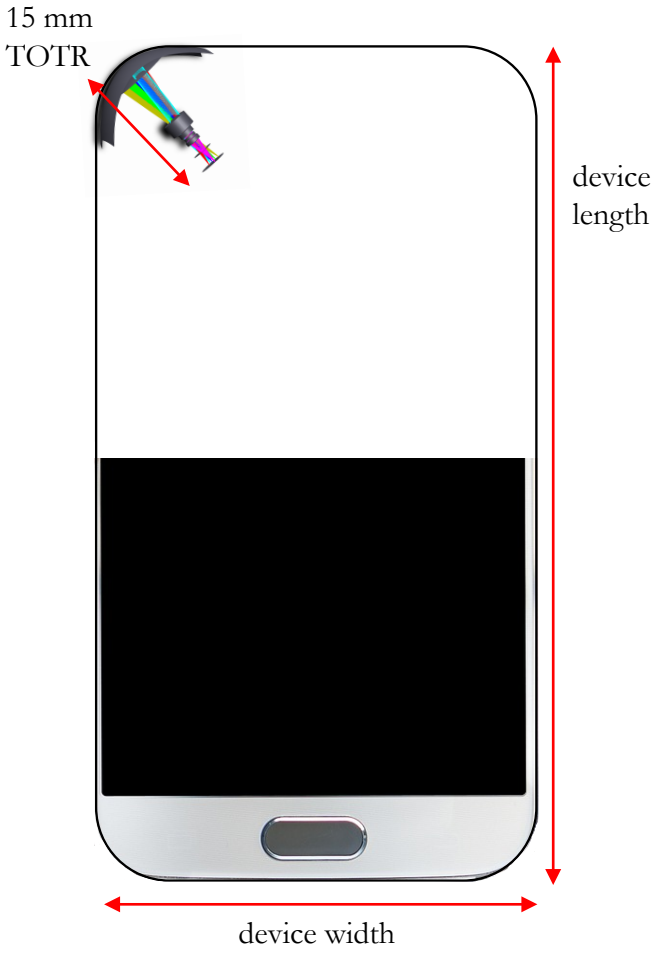

Figure 5.1: Proposed new position of camera lens within the phone or device. Half of the device is blank to illustrate the new camera location.

dependent aberrations, discussed in Chapter 2.

The modified lens orientation is not completely free from housing restrictions. A limitation on element diameters exists for all components, this is the device thickness. The rectangular front lens must fit within the device such that the lens height is defined by the device. However, the front lens width does not have any physical constraints. The optical limitation on the front lens geometry is the usable field angle. Stop position can also be used to control the diameter of the internal elements, so that the elements fit upright within the device housing. The scene is imaged with polychromatic light across a $90° \times 40°$ field of view. Typical

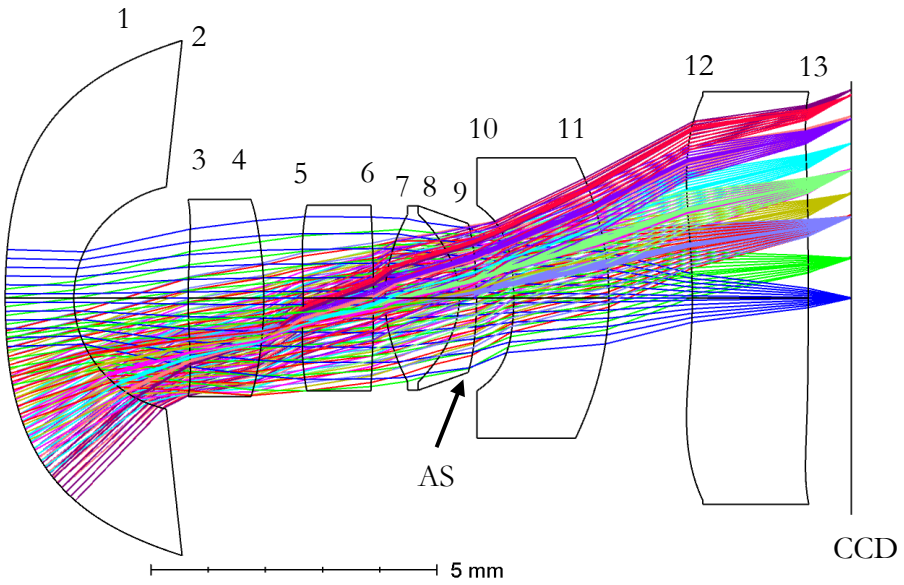

Figure 5.2: Widefield lens with total track length of 14.79 mm. All lenses adhere to the criteria of edge thickness being larger than 1/10 of the central element thickness.

wavelengths used in photographic imaging are 486 nm, 587 nm and 656 nm, therefore consideration must be given to the choice of lens material to minimise chromatic effects. The first element in the lens is a glass element labelled as surface 1 and 2 in Fig 5.2. Glass is chosen for optimal chromatic correction as the range of available plastics is limited. In addition, the most external lens is recommended to be made from tough glass to withstand scratching. In the case of a strong first element, a curved coverglass around the corner enclosing the camera can be considered.

The entrance pupil has a diameter of 1.72 mm, which is comparable to the semi-diameter for many of the components in the lens. The large pupil diameter is not common in wide field imaging due to the strong field dependent aberrations. Although the lens presented here claims a semi-classical solution, multiple aspherical surfaces are required for a large pupil diameter. It is worth noting that the polynomial orders here are reduced compared to current mobile phone lenses, only using up to 8^{th} order and all conicoids of revolution have a value in the range between $-1 \leq \kappa \leq 1.1$.

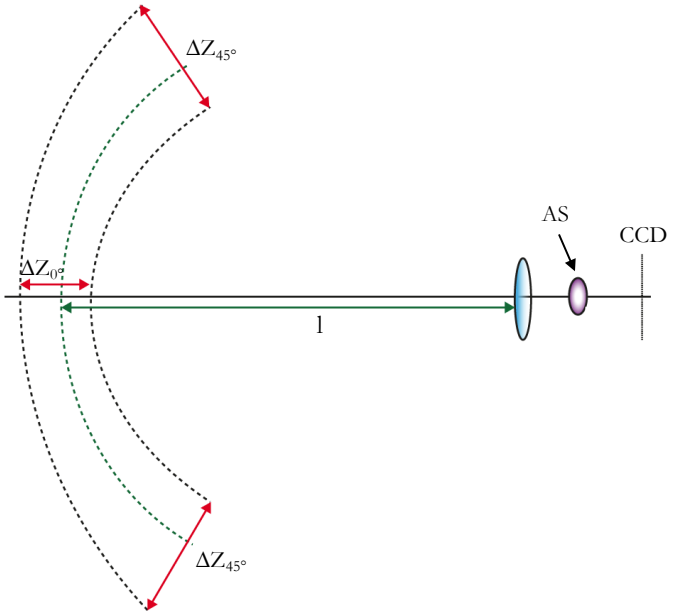

Figure 5.3: Dual-$F\#$ lens vignetted by an elliptical AS with yielding a variation in DOF across the field.

Function	Target Value
Working F-number	2
Ray Height in x	4 mm
Incident Ray Angle	20 deg
Relative Illumination	$\geq$ 50 %
% Distortion	$\leq$ 20 %
Total Track Length	15 mm
Min Edge Thickness in Glass	0.1 mm
Min Edge Thickness in Air	0.1 mm

Table 5.1: Input parameters for optimisation of the panoramic lens.

The lens data is presented in Table 5.2. A large front lens is responsible for collecting all field angles. Powerful front lenses can reduce the dimensions of the following elements. This is important as the elements must fit within the device housing inclusive with their mounting. The largest internal element diameter is

Surf	Rad (mm)	Thick (mm)	Glass	Conic	A (mm^{-3})	B (mm^{-5})	C(mm^{-7})
1	11.3404	1.2000	N-BK7	-1.101	4.9208×10^{-3}	-1.708×10^{-4}	9.547×10^{-6}
2	1.9	2.0000	Air	-0.0900	0	0	0
3	c 10.5058	1.3242	OKP4	-1.0036	-0.0172	1.5769×10^{-3}	-4.215×10^{-4}
4	-6.4948	0.6862	Air	-1.001	4.7254×10^{-3}	-1.147×10^{-4}	-5.103×10^{-4}
5	-10.7127	1.2300	OKP4	-0.9981	0.0437	-7.543×10^{-3}	4.4907×10^{-4}
6	-26.9613	0.2008	Air	-1.0139	0	0	0
7	2.5000	1.3000	440R	-0.999	-0.0155	4.5419×10^{-3}	-2.383×10^{-4}
8	-1.5000	0.3000	OKP4	-0.9951	0	0	0
STO	-8.1039	0.6518	Air	-1.000	-0.131	-1.917×10^{-4}	-1.349×10^{-4}
10	-5.0432	1.6518	Air	-0.9987	0	0	0
11	-5.1418	1.4587	OKP4	-0.9998	0	0	0
12	-10.3911	2.0251	BASF55	-1.0032	6.2042×10^{-3}	-1.202×10^{-4}	2.0473×10^{-6}
13	Infinity	0.7520	Air	0	-1.513×10^{-3}	6.7269×10^{-5}	4.2611×10^{-6}

Table 5.2: Lens data for widefield lens, where A, B and C are even aspheric coefficients of 4th, 6th and 8th order.

the last element with a semi-diameter of x =3.5 mm. The vertical component radius can be limited to y = 2 mm which comfortable fits within the device housing. This type of lens geometry is possible due to plastic moulding.

The lens has an F-number of $F\# = 2.32$ for a full unobscured aperture with entrance pupil diameter of 1.7 mm and a focal length of $f = 3.96$ mm. F-numbers of mobile phone modules are currently pixel limited. The maximum entrance pupil diameter is therefore determined by adequate pixel sampling of the Airy disk.

Dual channel lenses typically have a central ray path and a secondary path which is created by a beam-splitting component. This requires a generous design space, especially when considered within a mobile phone. In this design, strategically vignetting the incident ray bundles close to the AS can offer a dual $F\#$ lens using only the primary ray path. It is proposed that the central field retain the original $F\#$ while vignetting the larger field stops down the beam effectively increasing the $F\#$ of the lens, shown in Fig. 5.4. This approach creates a variation in depth of field across the scene, where $2(\Delta Z_{0^\circ}) \approx \Delta Z_{45^\circ}$.

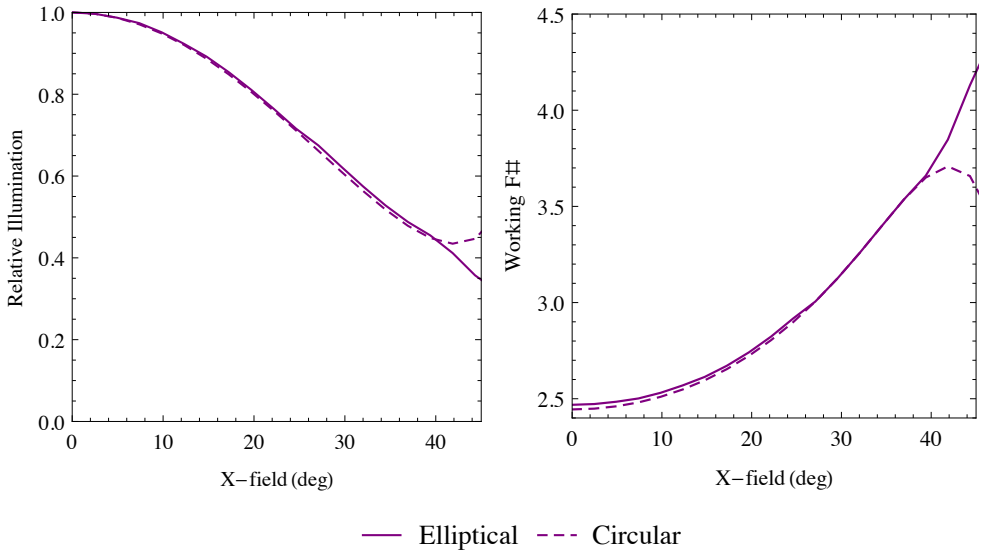

Figure 5.4: Left: Relative illumination for a full clear aperture and for the elliptical stop. Right: working $F\#$ for full aperture and for elliptical aperture.

Vignetting a widefield lens is not a trivial task as the largest fields are compressed and geometrically skewed, as seen in Fig. 5.6. These reduced beam cross

sections lead to illumination reduction for large field angles with a full clear aperture that follows the $\cos^4\theta$ illumination drop-off [13]. The field angle $(45°, 20°)$ is the most extreme point in the field of view. For this point the transmitted illumination is shown by a dashed purple line in Fig. 5.4. The edge illumination is approximately 50% for a full clear aperture. Introducing an ellipticity to the stop and vignetting half of the beam reduces the illumination by a further half. This effect is highlighted by the continuous purple line in Fig. 5.4. This reduction only exists toward the edge as the central fields are unobstructed.

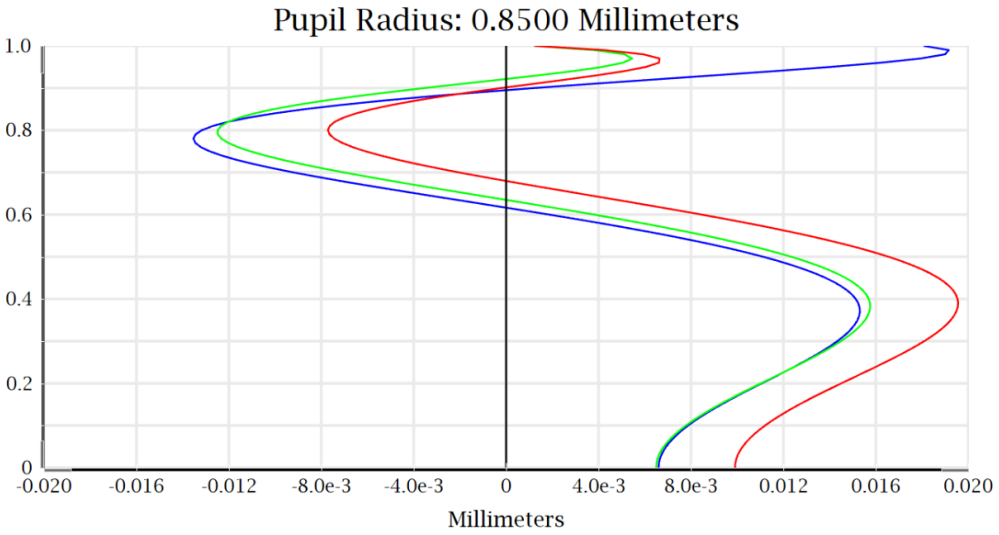

Figure 5.5: Longitudinal chromatic aberration about the image plane where the origin represents the CCD plane.

To simulate this effect without a detrimental loss of light to the system, the incoming ray pencils are modelled in Zemax whereby each field is compressed in dimensions as appropriate in the presence of the AS. The proposed design approaches a more classical lens with basic spherical surfaces. Plastic is chosen for the internal lens material as the elements are lightweight and inexpensive to manufacture. The range of polymers for imaging is restricted in range of RIs, and the residual LCA for the lens is plotted in Fig. 5.5.

A schematic for the lens vignetting including the modified aperture stop (AS) is shown Fig. 5.6. The physical dimensions of the AS are designed to adhere to

the field compression modelled in Zemax. For a conjugate object distance of 1m the $F\#$ for the central field is 2.32. Vignetting is not experienced equally across the field. Therefore, the $F\#$ increases with increasing field angle. That is, the $F\#$ increases as the section of the incoming ray bundle is truncated, where the largest obstruction happens at 45°, reducing the beam by half yielding an $F\#$ of 4.25. The total DOF for the unobscured fields is calculated from Eq.(1.26) as 744 mm at a mean wavelength of 550 nm, that is ± 371 mm when calculated directly from the equation. It can be extrapolated that scene has a total DOF of 1.49 m at the edge of the field.

Spot diagrams for the vignetted ray bundles are shown in Fig. 5.7. It is apparent that the lens performance diminishes with increasing field angle. A pixel size of $0.83\mu m$ is required to sample at Nyquist frequency. Recent advances in diminishing pixel size allow for 0.8 μm pixels. The spatial frequency response of the widefield lens is shown in Fig. 5.8. A sufficient sampling of image points across the field of view shows that the lens produces good image quality that is not compromised by aberrations with the exception for the very limiting edge of the field. This loss in contrast relates to the loss in illumination that was observed for the same field point in Fig 5.4.

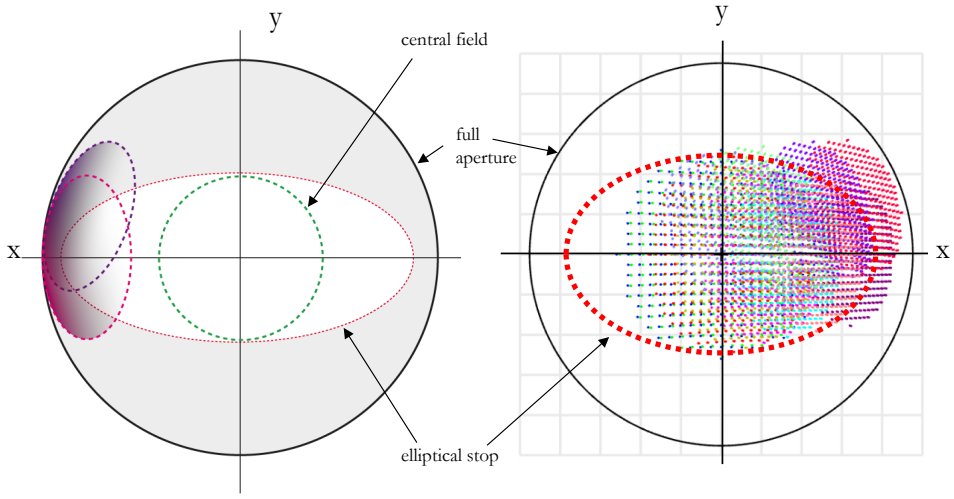

Figure 5.6: Light transmitted through the lens full aperture stop (black) and elliptical aperture stop (dashed red perimeter) showing the vignetting within the lens to achieve a central field of F/2.32 while the larger field angles are imaged at F/4.25.

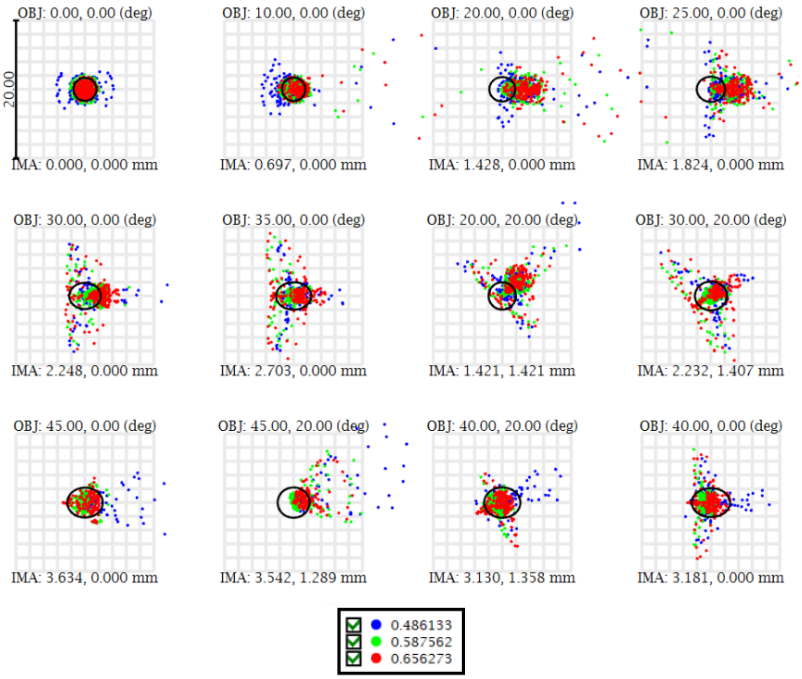

Figure 5.7: Spot diagrams for the vignetted beams of Airy disk radius 1.67μm.

Distortion control can be challenging in fast lenses. In this lens the design follows a more conventional approach for widefield lens design where the aperture stop is located at the center of the lens. This allows for a balance of elements at both sides of the stop. Residual distortion at the edge of the field is -14.8% distortion, which can be easily corrected computationally as no image blur is introduced. Table 5.2 lists multiple strong radii present in this design. A long TTL allows for optimal balancing of optical power within the lens to effectively reduce the field curvature on the CCD plane, shown on the right in Fig. 5.9.

Once vignetted, the effect of field dependent aberrations is reduced. The rms wavefront error across the largest half field is shown in Fig. 5.10, where the performance across all channels are close to the diffraction limit.

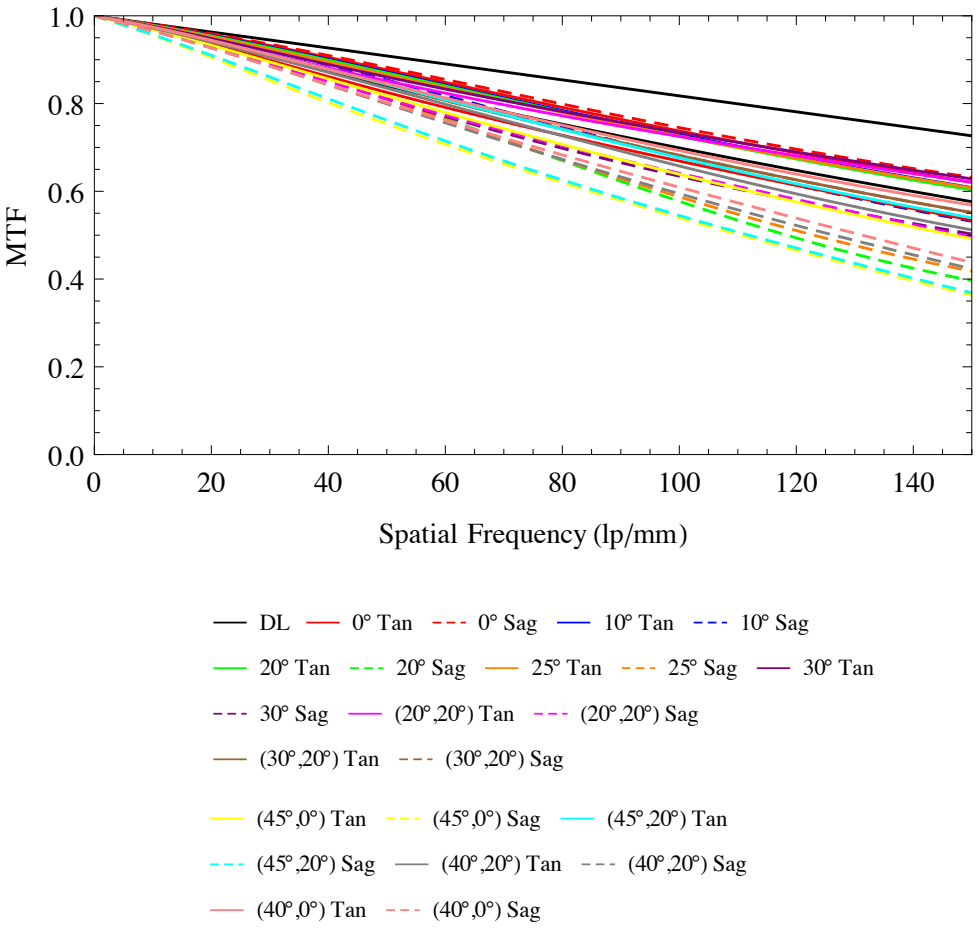

Figure 5.8: MTF for compressed pencils simulating the presence of the elliptical stop.

Pixel Binning

On-chip binning is the process of summing the charge from groups of adjacent pixels at the output node capacitor of the CCD [100]. In doing so, the group of pixels can be considered as one large pixel. Binning is applied to this application to counteract the loss of intensity experienced by large field angle due to vignetting. The CCD is divided into sub-sections where the vignetted fields are binned as 4×4, while the central field is not binned. This approach can adequately sample across the FOV, avoiding under and oversampling of image points. The CCD sectioning for binning purposes is shown in Fig. 5.11. Implementing this effect in Zemax, field angles are vignetted by weighting functions, that is where a smaller

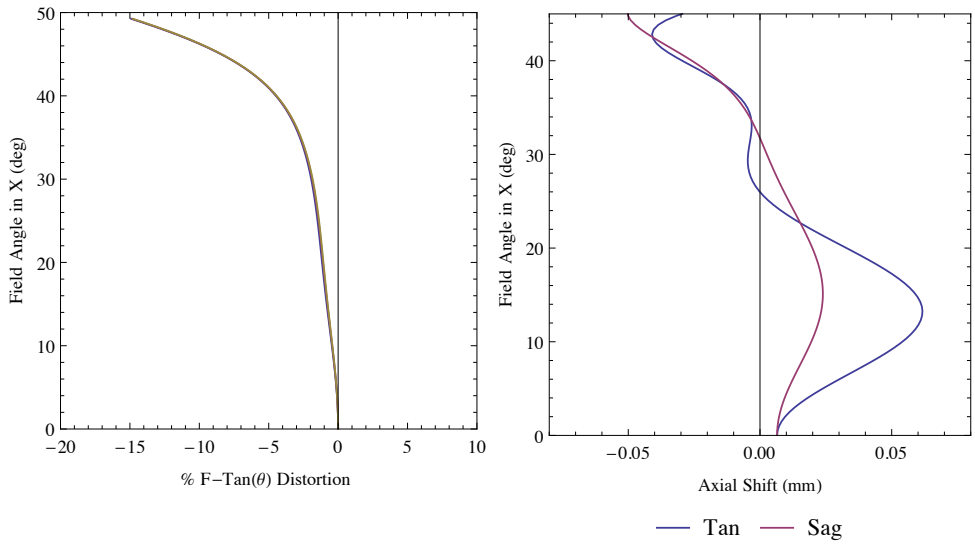

Figure 5.9: Left: percentage distortion across the field.Right: field curvature at the mean wavelength of $\lambda = 550nm$, sagittal deviation from the CCD plane is shown in pink and tangential deviations in purple.

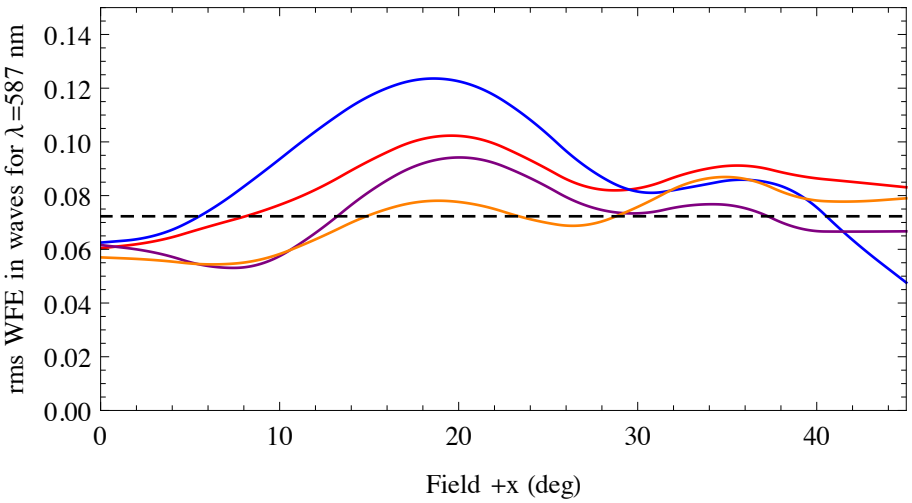

Figure 5.10: rms wavefront error across the field of view for the elliptically vignetted aperture.

cross-section beam propagates through the lens while retaining the intensity of a full beam. This effectively simulates the output signal from the 4x4 sampled pixels for large angles.

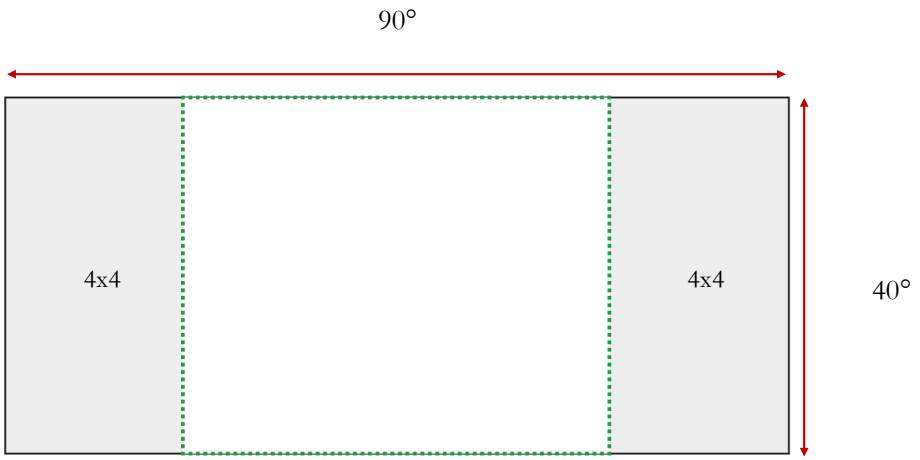

Figure 5.11: Binning of pixels in the F/4.25 and F/2.32 regions.

Zemax simulations cannot faithfully represent the required binning areas, only for central and edge effects where the fraction of beam truncation is in whole or half. For a pixel size of 0.8 μm and proposed sensor dimensions of 7.8×4mm requires an active pixel area of 9750×5000. Detectors of these dimensions can be manufactured although it is worth noting that the active pixel area is approximately equal to the two adjacent standard CCD sensors together. A two-sensor approach could be employed if the discontinuity in the centre of the field is digitally corrected.

Mechanical Refocus

Asymmetry associated with the in-focus regions around the object position is not a concern in this application if the lens has a VCM. The lens is conjugate to an object at 1 meter from the front vertex of the lens. Refocusing can be incorporated by changing the conjugate object position and then shifting the last element axially by a distance that refocuses the lens maintaining a constant TTL. A range of object distances from $l = 500$ mm to $l = 5000$ mm were chosen to test the maximum displacement in which the final lens compound must shift to focus. The largest distances from the original conjugate object point are listed in Table 5.3. The element is displaced sufficiently to refocus the lens while retaining

a constant TTL. The last compound lens element is chosen for refocusing as the angle of refraction is minimal over the three surfaces, labelled as surfaces 12 to 14 in Fig 5.2, and therefore more tolerable to displacement.

Surf	Thickness (mm)	Thickness Variation 1(mm)	Thickness Variation 2(mm)
0	1000	500	5000
11	1.4587	1.4540	1.467
13	0.7520	0.7558	0.75

Table 5.3: Multi-conjugate object distances and refocusing distances.

Distances closer than 500 mm from the lens generates undesirable effects in the lens such as a reduction in contrast and increase in distortion. Smaller distances would not be beneficial for video conferencing due to the FOV. Refocusing the lens allows for a conjugate range of object positions between 500 mm and 5m without experiencing image deterioration. The maximum translation of the last component to allow for the full range of defocus is $12\mu m$.

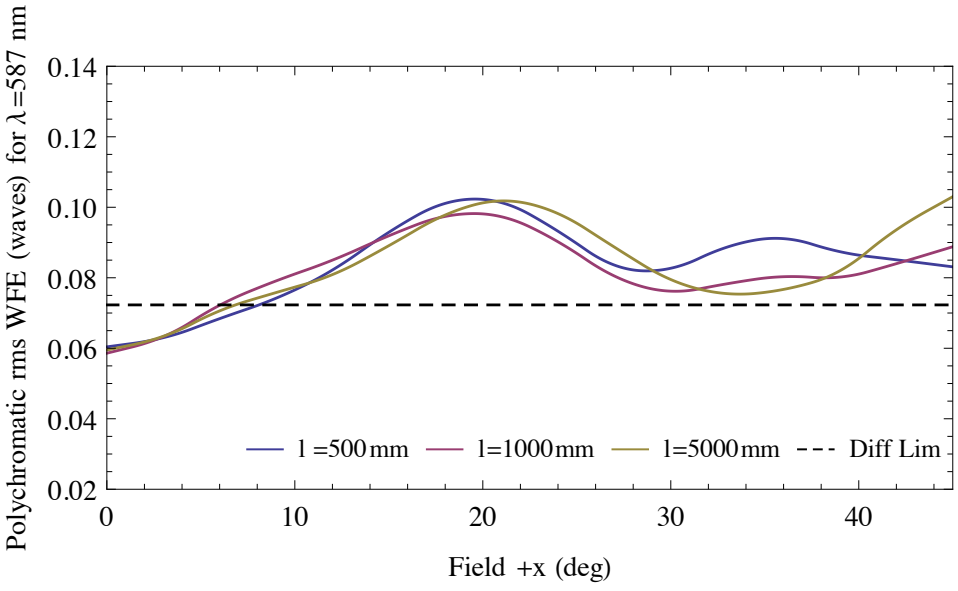

Figure 5.12: rms across the field with mechanical refocusing

5.3 Conclusion

A new wide field smartphone camera lens is presented with a novel orientation, whereby the front lens is positioned at the corner of the phone or device. The rectangular field of view would be sufficient for a video conferencing application. The centre field has a high resolution shallow depth of field while the peripheral regions of the field have a larger depth of field of lower image quality. Partial-detector binning allows for the compensation of any intensity losses from the modified stop. In addition to this, the lens can be mechanically refocused without image quality degradation allowing the extended depth of field to be increased by a factor of 10. Future designs may introduce a folding element where the CCD can be positioned on the flat surface of the device.

Chapter 6

Conclusions & Future Work

An optically-generated extended depth of field is a desirable feature in imaging systems as it can reduce the dependency on mechanical refocussing and computational post-processing. Three novel approaches for extending depth of field in fast miniaturised lenses are proposed in this thesis.

Study 1: Chromatic EDOF

Intrinsic chromatic aberration of a singlet was used to generate object space LCA. Many previous applications have utilised LCA for EDOF using computational image reconstruction. The methodology proposed in this chapter introduces a wavelength dependent approach for extending DOF, which can be systematically carried out through the analytical proofs. Illumination is provided by two commercially available NIR LEDs with central wavelengths of $\lambda_1 = 780$ nm and $\lambda_2 = 870$ nm, respectively. The use of NIR illumination comes from the requirement to resolve the fine details of the iris of the eye, which are lost in the visible spectrum. As a full analytical methodology is presented, illumination wavelengths are another design parameter.

The study includes the feasibility of both low and high dispersion materials and their effect in achieving an extended depth of field. The performance of this method also includes a model of the cornea and the possibility of induced aberrations by refracting from the cornea. This analysis shows that -9% distortion is introduced and does not deteriorate the MTF. The field of view is limited to 6°. This is acceptable for a singlet lens, as the field is also sufficient to image a single iris.

Study 2: Two eye EDOF

Spatially dependent solution to imaging two irises over an extended depth of field.

Two design configurations for imaging both irises over an extended depth of field are presented. Each design configuration involves multiple solutions. The iris dimensions are chosen for the case of maximum separated irises, an IPD of 35 ± 6 mm. A smaller IPD can be chosen for a specific user. This design is based upon simple geometry. Decreasing the IPD will decrease the principle ray angle and thus reduce the required image displacement. This statement only holds for a lens of the same parameters. Considering fundamental aberration theory, smaller interpupillary distances have smaller field angle and so do not induce large amplitudes of field dependent aberrations. It is important to note that the degree of variation of the sag across the plate surface is fundamentally dependent on the lens preceding the plate. The sole purpose of the plate element should be for image point displacement.

Two viable solutions for the high yield consumer market would be a Zernike radially varying plate and a cylindrical lens with vertically-varying thickness. Both plates are capable of extending the depth of field of their associated lenses by 3.1 and 2.9 times respectively. Both solutions show an acceptable tolerance range, where the Zernike plate provides a critical decrease in MTF at large principle ray angles as the irises are displaced vertically. One aspect to note in design is that the radially varying thickness plates should be produced specifically for a user-specific IPD due the demanding sag variation required. This is not the case for the vertically thickness varying plates as the statistical variation in IPD is corrected for in the fundamental field dependent aberration correction with aspheres on surfaces 1 to 6. It is for this reason that the vertically thickness varying plates would be the best solution for a high yield market such as the consumer imaging market. In turn, as the lens-plate combination can be used by all IPDs, then the specificity for biometric imaging would be dependent on the calibration and software.

Study 3: Widefield EDOF

A new lens orientation is presented where the use of vignetting and pixel binning allows the user to exploit a dual-f-number feature across the field of view. The proposed novel positioning of the lens, at the corner of the device allows for a more classical approach to the lens design. Although the necessity for a large entrance pupil requires high order aspherical surfaces to be employed to minimise the effect of field dependent aberrations. Residual chromatic effects exist due to a limitation in available refractive indices for optical polymers. This limitation still remains a design drawback for commercial applications. Larger sensors are required with non-standard aspect ratios.

Future Work

The importance of imaging and depth sensing in current smart devices is being increasingly recognised. This realisation gives rise to an increase in allocated design space for imaging modules. This increased design space is currently being used for multiple miniaturised cameras, all of similar dimensions to the five plastic element designs commonly used today. Multiple cameras can be used for stereo imaging, and also for the simulation of depth of optical features such as zoom and DOF. This increase in design space is a tremendous advantage to the optical designer whereby the designs can be more creative. The optics found within commercial camera modules may have the option to depart from polynomial dependent surfaces and converge toward more traditional designs possible allowing for a considerable optical zoom. A shift in fixed camera parameters for both device manufacturers and commercial miniature lens designers promises that the field of fast commercial lenses has the prospect of delivering high quality imaging.

Bibliography

[1] C.-S. Chen, T.-H. Tsai, and M.-T. Chou, "Optical image lens system," Nov. 8 2016. US Patent 9,488,803. (Cited on pages xiii and 2.)

[2] V. N. Mahajan, *Optical Imaging and Aberrations: Ray Geometrical Optics*, vol. I. SPIE Press, 1998. (Cited on pages xiv, 38 and 46.)

[3] D. A. Atchison and G. Smith, *Optics of the human eye*. Butterworth-Heinemann Oxford, 2000. (Cited on pages xv, 73 and 74.)

[4] S. AG, "Optical glass catalogue." https://www.schott.com, Germany. (Cited on pages xv and 78.)

[5] Z. Corporation, "Cyclo olefin polymer (cop) - zeonex datasheet," Japan. (Cited on pages xv and 78.)

[6] V. N. Mahajan, *Optical Imaging and Aberrations, Part II: Wave Diffraction Optics*. SPIE Press, 2011. (Cited on pages 4 and 18.)

[7] W. J. Smith, *Modern Optical Engineering*. McGraw-Hill Education, 1966. (Cited on pages 4 and 70.)

[8] H. Hopkins, "The application of frequency response techniques in optics," *Proceedings of the Physical Society*, vol. 79, no. 5, p. 889, 1962. (Cited on page 6.)

[9] J. Goodman, *Introduction to Fourier Optics*. W.H. Freedman Co. Ltd, 2008. (Cited on pages 6 and 8.)

[10] T. Williams, *The Optical Transfer Function of Imaging Systems*. CRC Press, 1998. (Cited on page 6.)

[11] M. Freeman and C. Hull, *Optics*. Butterworth-Heinemann, 11th ed., 2003. (Cited on pages 11, 12, 34 and 50.)

[12] M. Laikin, *Lens Design*. CRC Press, 2006. (Cited on pages 12, 70 and 72.)

[13] H. Gross, F. Blechinger, and B. Achtner, *Handbook of Optical Systems Volume 4 : Survey of Optical Instruments*. Wiley-VLC, 2008. (Cited on pages 12 and 136.)

[14] W. T. Welford, "Use of annular apertures to increase focal depth," *JOSA*, vol. 50, no. 8, pp. 749–753, 1960. (Cited on page 13.)

[15] E. R. Dowski and W. T. Cathey, "Extended depth of field through wavefront coding," *Applied Optics*, vol. 34, no. 11, pp. 1859–1866, 1995. (Cited on page 14.)

[16] E. Ben-Eliezer, N. Konforti, B. Milgrom, and E. Marom, "An optimal binary amplitude-phase mask for hybrid imaging systems that exhibit high resolution and extended depth of field," *Optics Express*, vol. 16, no. 25, pp. 20540–20561, 2008. (Cited on page 14.)

[17] S. Elmalem, N. Konforti, and E. Marom, "Polychromatic imaging with extended depth of field using phase masks exhibiting constant phase over broad wavelength band," *Applied Optics*, vol. 52, no. 36, pp. 8634–8643, 2013. (Cited on page 15.)

[18] B. Milgrom, N. Konforti, M. A. Golub, and E. Marom, "Novel approach for extending the depth of field of barcode decoders by using rgb channels of information," *Optics Express*, vol. 18, no. 16, pp. 17027–17039, 2010. (Cited on page 15.)

[19] H. Haim, A. Bronstein, and E. Marom, "Computational multi-focus imaging combining sparse model with color dependent phase mask," *Optics Express*, vol. 23, no. 19, pp. 24547–24556, 2015. (Cited on page 15.)

[20] B. Milgrom, N. Konforti, M. A. Golub, and E. Marom, "Pupil coding masks for imaging polychromatic scenes with high resolution and extended depth of field," *Optics Express*, vol. 18, no. 15, pp. 15569–15584, 2010. (Cited on page 15.)

[21] E. Ben-Eliezer, E. Marom, N. Konforti, and Z. Zalevsky, "Experimental

realization of an imaging system with an extended depth of field," *Applied Optics*, vol. 44, pp. 2792–2798, May 2005. (Cited on pages 15 and 24.)

[22] N. Caron and Y. Sheng, "Polynomial phase masks for extending the depth of field of a microscope," *Applied Optics*, vol. 47, no. 22, pp. E39–E43, 2008. (Cited on page 16.)

[23] D.-m. Zhou, H.-B. Cheng, H.-Y. Tam, Y. Wen, and X. Ye, "Extending the depth of field of integral imaging system by employing cubic phase plate," *Optik-International Journal for Light and Electron Optics*, vol. 124, no. 24, pp. 7065–7069, 2013. (Cited on page 16.)

[24] M. Larivière-Bastien and S. Thibault, "Limits of imaging-system simplification using cubic mask wavefront coding," *Optics letters*, vol. 38, no. 19, pp. 3830–3833, 2013. (Cited on page 16.)

[25] L. Ledesma-Carrillo, R. Guzmán-Cabrera, C. M. Gómez-Sarabia, M. Torres-Cisneros, and J. Ojeda-Castañeda, "Tunable field depth: hyperbolic optical masks," *Applied Optics*, vol. 56, no. 1, pp. A104–A114, 2017. (Cited on page 16.)

[26] M.-A. Burcklen, F. Diaz, F. Leprêtre, J. Rollin, A. Delboulbé, M.-S. Lee, B. Loiseaux, A. Koudoli, S. Denel, P. Millet, *et al.*, "Experimental demonstration of extended depth-of-field f/1.2 visible high definition camera with jointly optimized phase mask and real-time digital processing," *Journal of the European Optical Society*, vol. 10, 2015. (Cited on page 17.)

[27] M. Olvera-Angeles, A. Padilla-Vivanco, K. Ortega, J. Sasian, J. Schwiegerling, J. Arines, and E. Acosta, "Optimizing trefoil phase plates design for color wavefront coding," in *Current Developments in Lens Design and Optical Engineering XIX*, vol. 10745, p. 1074515, International Society for Optics and Photonics, 2018. (Cited on page 17.)

[28] O. Palillero-Sandoval, J. F. Aguilar, and L. Berriel-Valdos, "Phase mask coded with the superposition of four zernike polynomials for extending the depth of field in an imaging system," *Applied optics*, vol. 53, no. 18, pp. 4033–4038, 2014. (Cited on page 18.)

[29] M. Bergkoetter and J. Bentley, "Extended depth of field in an intrinsically wavefront-encoded biometric iris camera," in *International Optical Design Conference*, pp. IW3A–2, Optical Society of America, 2014. (Cited on page 18.)

[30] W. Charman and H. Whitefoot, "Pupil diameter and the depth-of-field of the human eye as measured by laser speckle," *Optica Acta: International Journal of Optics*, vol. 24, no. 12, pp. 1211–1216, 1977. (Cited on page 18.)

[31] S. Mezouari and A. R. Harvey, "Phase pupil functions for reduction of defocus and spherical aberrations," *Optics letters*, vol. 28, no. 10, pp. 771–773, 2003. (Cited on page 18.)

[32] P. Mouroulis, "Depth of field extension with spherical optics," *Optics Express*, vol. 16, no. 17, pp. 12995–13004, 2008. (Cited on page 18.)

[33] T. Nakamura, R. Horisaki, and J. Tanida, "Computational superposition compound eye imaging for extended depth-of-field and field-of-view," *Optics express*, vol. 20, no. 25, pp. 27482–27495, 2012. (Cited on page 18.)

[34] H. Tang and K. N. Kutulakos, "Utilizing optical aberrations for extended-depth-of-field panoramas," in *Asian Conference on Computer Vision*, pp. 365–378, Springer, 2012. (Cited on page 19.)

[35] X. Guo, L. Kong, Y. Wu, Y. Zhao, L. Dong, and M. Liu, "Design and implementation of a large depth-of-field and large aperture optical system," in *Novel Optical Systems Design and Optimization XX*, vol. 10376, p. 103760E, International Society for Optics and Photonics, 2017. (Cited on page 19.)

[36] K. Chu, N. George, and W. Chi, "Extending the depth of field through unbalanced optical path difference," *Applied optics*, vol. 47, no. 36, pp. 6895–6903, 2008. (Cited on page 19.)

[37] W. Chi, K. Chu, and N. George, "Polarization coded aperture," *Optics express*, vol. 14, no. 15, pp. 6634–6642, 2006. (Cited on page 19.)

[38] C. Olsovsky, R. Shelton, O. Carrasco-Zevallos, B. E. Applegate, and K. C. Maitland, "Chromatic confocal microscopy for multi-depth imaging of epithelial tissue," *Biomedical optics express*, vol. 4, no. 5, pp. 732–740, 2013. (Cited on page 20.)

[39] O. Cossairt, C. Zhou, and S. Nayar, "Diffusion coded photography for extended depth of field," in *ACM Transactions on Graphics (TOG)*, vol. 29, p. 31, ACM, 2010. (Cited on page 20.)

[40] S. Sanyal, P. Bandyopadhyay, and A. Ghosh, "Vector wave imagery using a birefringent lens," *Optical Engineering*, vol. 37, no. 2, pp. 592–600, 1998. (Cited on page 20.)

[41] S. Mandal, S. Sanyal, and A. Ghosh, "Imaging characteristics of a birefringent lens under broadband illumination," *Optik-International Journal for Light and Electron Optics*, vol. 118, no. 7, pp. 335–339, 2007. (Cited on page 20.)

[42] S. Sanyal and A. Ghosh, "High focal depth with a quasi-bifocus birefringent lens," *Applied optics*, vol. 39, no. 14, pp. 2321–2325, 2000. (Cited on page 20.)

[43] W. Singer, M. Totzeck, and H. Gross, *Handbook of optical systems, volume 2: Physical image formation*. John Wiley & Sons, 2006. (Cited on page 20.)

[44] L. Wang, T. Hayakawa, and M. Ishikawa, "Depth of field extended imaging method based on intensification of time and spatial expansion," in *Nanosensors, Biosensors, Info-Tech Sensors and 3D Systems 2017*, vol. 10167, p. 101670C, International Society for Optics and Photonics, 2017. (Cited on page 21.)

[45] H.-S. Chen and Y.-H. Lin, "An endoscopic system adopting a liquid crystal lens with an electrically tunable depth-of-field," *Optics express*, vol. 21, no. 15, pp. 18079–18088, 2013. (Cited on page 21.)

[46] T. Galstian, O. Sova, K. Asatryan, V. Presniakov, A. Zohrabyan, and

M. Evensen, "Optical camera with liquid crystal autofocus lens," *Optics express*, vol. 25, no. 24, pp. 29945–29964, 2017. (Cited on page 22.)

[47] Q. Tong, M. Chen, Z. Xin, D. Wei, X. Zhang, J. Liao, H. Wang, and C. Xie, "Depth of field extension and objective space depth measurement based on wavefront imaging," *Optics Express*, vol. 26, no. 14, pp. 18368–18385, 2018. (Cited on page 22.)

[48] C. J. Sheil, "Tunable thermally induced gradient index for extended depth of field," *Applied Optics*, vol. 57, no. 22, pp. E71–E79, 2018. (Cited on page 22.)

[49] Z. Zhai, S. Ding, Q. Lv, X. Wang, and Y. Zhong, "Extended depth of field through an axicon," *Journal of modern Optics*, vol. 56, no. 11, pp. 1304–1308, 2009. (Cited on page 23.)

[50] P. Favaro, "A split-sensor light field camera for extended depth of field and superresolution," in *Proc. SPIE*, vol. 8436, p. 843602, 2012. (Cited on page 23.)

[51] S. Barbero and J. Rubinstein, "Adjustable-focus lenses based on the alvarez principle," *Journal of Optics*, vol. 13, no. 12, p. 125705, 2011. (Cited on page 24.)

[52] J. Ojeda-Castañeda, E. Yepez-Vidal, and C. M. Gómez-Sarabia, "Multiple-frame photography for extended depth of field," *Applied optics*, vol. 52, no. 10, pp. D84–D91, 2013. (Cited on page 24.)

[53] S. Barbero, "The alvarez and lohmann refractive lenses revisited," *Optics express*, vol. 17, no. 11, pp. 9376–9390, 2009. (Cited on page 24.)

[54] M. Bawart, A. Jesacher, P. Zelger, S. Bernet, and M. Ritsch-Marte, "Modified alvarez lens for high-speed focusing," *Optics express*, vol. 25, no. 24, pp. 29847–29855, 2017. (Cited on page 24.)

[55] L. Zhou, Q. Shan, Z. Liu, and W. She, "Extending the depth-of-field and ranging the scene with a shifted phase mask," in *Fifth Conference*

on Frontiers in Optical Imaging Technology and Applications, vol. 10832, p. 108320B, International Society for Optics and Photonics, 2018. (Cited on page 25.)

[56] H. Nagahara, S. Kuthirummal, C. Zhou, and S. K. Nayar, "Flexible depth of field photography," in *European Conference on Computer Vision*, pp. 60–73, Springer, 2008. (Cited on page 25.)

[57] R. Yokoya and S. K. Nayar, "Extended depth of field catadioptric imaging using focal sweep," in *Proceedings of the IEEE International Conference on Computer Vision*, pp. 3505–3513, 2015. (Cited on page 25.)

[58] O. Cossairt and S. Nayar, "Spectral focal sweep: Extended depth of field from chromatic aberrations," in *Computational Photography (ICCP), 2010 IEEE International Conference on*, pp. 1–8, IEEE, 2010. (Cited on page 26.)

[59] F. Guichard, H.-P. Nguyen, R. Tessières, M. Pyanet, I. Tarchouna, and F. Cao, "Extended depth-of-field using sharpness transport across color channels," in *Proc. SPIE*, vol. 7250, pp. 72500N–72500N–12, 2009. (Cited on page 26.)

[60] Q. Qian and B. K. Gunturk, "Extending depth of field and dynamic range from differently focused and exposed images," *Multidimensional Systems and Signal Processing*, vol. 27, no. 2, pp. 493–509, 2016. (Cited on page 27.)

[61] Q. Wang, Z. Yu, C. Rasmussen, and J. Yu, "Stereo vision–based depth of field rendering on a mobile device," *Journal of Electronic Imaging*, vol. 23, no. 2, pp. 023009–023009, 2014. (Cited on page 27.)

[62] P. Zammit, A. R. Harvey, and G. Carles, "Extended depth-of-field imaging and ranging in a snapshot," *Optica*, vol. 1, no. 4, pp. 209–216, 2014. (Cited on page 27.)

[63] S. Bagheri and B. Javidi, "Extension of depth of field using amplitude and phase modulation of the pupil function," *Optics letters*, vol. 33, no. 7, pp. 757–759, 2008. (Cited on page 27.)

[64] C. Zhang, J. Bastian, C. Shen, A. van den Hengel, and T. Shen, "Extended depth-of-field via focus stacking and graph cuts," in *Image Processing (ICIP), 2013 20th IEEE International Conference on*, pp. 1272–1276, IEEE, 2013. (Cited on page 28.)

[65] S. Elmalem, R. Giryes, and E. Marom, "Learned phase coded aperture for the benefit of depth of field extension," *Optics Express*, vol. 26, no. 12, pp. 15316–15331, 2018. (Cited on page 28.)

[66] M. Lopez-Ramirez, L. Ledesma-Carrillo, E. Cabal-Yepez, G. Botella, C. Rodriguez-Donate, and S. Ledesma, "Fpga-based methodology for depth-of-field extension in a single image," *Digital Signal Processing*, vol. 70, pp. 14–23, 2017. (Cited on page 29.)

[67] Y. Piao, M. Zhang, X. Wang, and P. Li, "Extended depth of field integral imaging using multi-focus fusion," *Optics Communications*, vol. 411, pp. 8–14, 2018. (Cited on page 29.)

[68] M. Born and E. Wolf, *Principles of optics: electromagnetic theory of propagation, interference and diffraction of light*. Elsevier, 1980. (Cited on pages 33, 35, 41, 49 and 58.)

[69] J. Braat and P. Török, *Imaging optics*. Cambridge University Press, 2019. (Cited on pages 33 and 84.)

[70] H. Gross, *Handbook of Optical Systems*, vol. 1. Wiley-VLC, 2005. (Cited on page 34.)

[71] H. Gross, H. Zügge, M. Peschka, and F. Blechinger, *Handbook of Optical Systems, Volume 3: Aberration Theory and Correction of Optical Systems*. Wiley-VCH, 2007. (Cited on pages 37, 38, 40, 42, 44, 48, 50, 55, 61 and 64.)

[72] W. R. Hamilton, "Theory of systems of rays," *Transactions of the Royal Irish Academy*, vol. 15, no. 1828, pp. 69–174, 1828. (Cited on page 38.)

[73] W. R. Hamilton, "Supplement to an essay on the theory of systems of rays," *The Transactions of the Royal Irish Academy*, pp. 3–62, 1830. (Cited on page 38.)

[74] J. Sasián, *Introduction to Aberrations in Optical Imaging Systems.* Cambridge University Press, 2013. (Cited on page 38.)

[75] K. P. Thompson, *Aberration fields in tilted and decentered optical systems.* PhD thesis, University of Arizona, 1980. (Cited on pages 38 and 39.)

[76] W. T. Welford, *Aberrations of Optical Systems.* CRC Press, 1986. (Cited on pages 40, 42, 46, 50, 58, 61, 74 and 75.)

[77] R. N. Wilson, *Reflecting Telescope Optics I.* Springer Science, 1996. (Cited on page 43.)

[78] R. Kingslake, *Optical System Design.* Academic Press, 2012. (Cited on page 44.)

[79] J. C. Wyant and K. Creath, "Basic wavefront aberration theory for optical metrology," *Applied optics and optical engineering*, vol. 11, no. s 29, p. 2, 1992. (Cited on page 49.)

[80] C. Zhao and J. H. Burge, "Criteria for correction of quadratic field-dependent aberrations," *JOSA A*, vol. 19, no. 11, pp. 2313–2321, 2002. (Cited on page 52.)

[81] C. Zhao and J. H. Burge, "Application of the pupil astigmatism criteria in optical design," *Applied optics*, vol. 41, no. 34, pp. 7288–7293, 2002. (Cited on page 52.)

[82] R. E. Fischer, B. Tadic-Galeb, P. R. Yoder, and R. Galeb, *Optical system design.* Citeseer, 2000. (Cited on pages 54 and 62.)

[83] J. M. Geary, *Introduction to lens design: with practical ZEMAX examples.* Willmann-Bell Richmond, 2002. (Cited on pages 55 and 57.)

[84] P. Mouroulis and J. Macdonald, *Geometrical optics and optical design.* Oxford University Press, USA, 1997. (Cited on page 58.)

[85] A. E. Conrady, *Applied Optics and Optical Design, Part One.* Courier Corporation, 2013. (Cited on page 60.)

[86] M. J. Kidger, *Fundamental Optical Design.* SPIE Press, 2001. (Cited on pages 60 and 61.)

[87] R. Zemax, *Zemax User's Manual*, 2011. (Cited on page 66.)

[88] J. Ye, L. Chen, X. Li, Q. Yuan, and Z. Gao, "Review of optical freeform surface representation technique and its application," *Optical Engineering*, vol. 56, no. 11, p. 110901, 2017. (Cited on page 66.)

[89] N. M. Fitzgerald, C. Dainty, and A. V. Goncharov, "Extending the depth of field with chromatic aberration for dual-wavelength iris imaging," *Optics Express*, vol. 25, pp. 31696–31707, Dec 2017. (Cited on pages 69 and 92.)

[90] N. Fitzgerald, A. V. Goncharov, and C. Dainty, "Extending the depth of field in a fixed focus lens using axial colour," in *Proc. SPIE*, vol. 10590, p. 105902A, SPIE, 2017. (Cited on page 69.)

[91] C. J. Sheil and A. V. Goncharov, "Crystalline lens paradoxes revisited: significance of age-related restructuring of the grin," *Biomed. Opt. Express*, vol. 8, pp. 4172–4180, Sep 2017. (Cited on page 83.)

[92] H. Navarro, G. Saavedra, M. Martínez-Corral, M. Sjostrom, and R. Olsson, "Depth-of-field enhancement in integral imaging by selective depth-deconvolution," *Journal of Display Technology*, vol. 10, no. 3, pp. 182–188, 2014. (Cited on page 83.)

[93] W. G. 3, "Iso/iec 19794-6 information technology - biometric data interchnage formats - part 6: Iris image," *International Standard Edition*, vol. 44, 2011. (Cited on page 84.)

[94] N. M. Fitzgerald, C. Dainty, and A. V. Goncharov, "Two iris imaging over an extended depth of field with a mobile phone camera," in *Optical Design and Engineering VII*, vol. 10690, p. 106900X, International Society for Optics and Photonics, 2018. (Cited on page 92.)

[95] K. Fuerschbach, J. P. Rolland, and K. P. Thompson, "A new family of optical systems employing φ-polynomial surfaces," *Optics express*, vol. 19, no. 22, pp. 21919–21928, 2011. (Cited on page 105.)

[96] A. Broemel, U. Lippmann, and H. Gross, "Freeform surface descriptions. part i: Mathematical representations," *Advanced Optical Technologies*, vol. 6, no. 5, pp. 327–336, 2017. (Cited on page 105.)

[97] A. Brückner, J. Duparré, R. Leitel, P. Dannberg, A. Bräuer, and A. Tünnermann, "Thin wafer-level camera lenses inspired by insect compound eyes," *Optics Express*, vol. 18, no. 24, pp. 24379–24394, 2010. (Cited on page 129.)

[98] Y. Yan and J. Sasian, "Miniature camera lens design with a freeform surface," in *International Optical Design Conference 2017*, vol. 10590, p. 1059012, International Society for Optics and Photonics, 2017. (Cited on page 130.)

[99] B. Ma, K. Sharma, K. P. Thompson, and J. P. Rolland, "Mobile device camera design with q-type polynomials to achieve higher production yield," *Optics express*, vol. 21, no. 15, pp. 17454–17463, 2013. (Cited on page 130.)

[100] I. S. McLean, *Electronic Imaging in Astronomy: Detectors and Instrumentation*. Springer Science & Business Media, 2008. (Cited on page 139.)